GROUND PENETRATING RADAR

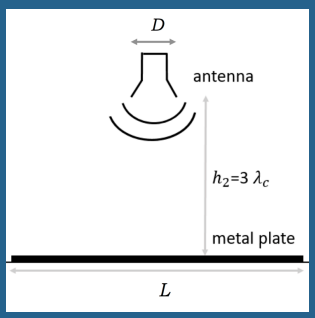

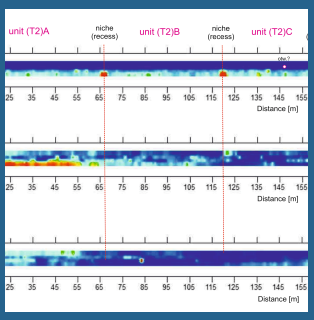

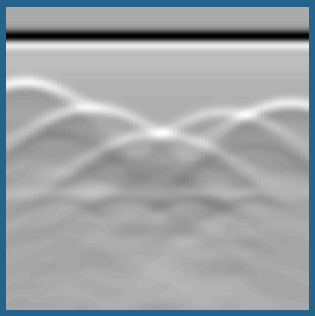

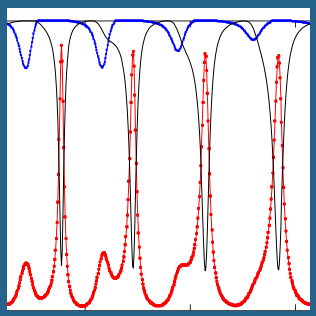

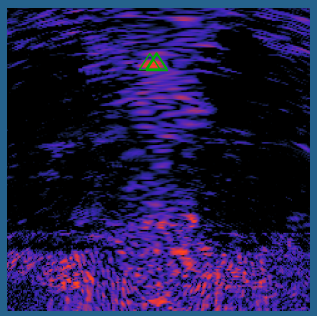

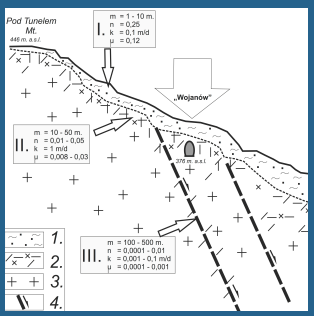

Issue 2, Volume 1

July 2018

www.GPRadar.eu/journal

Ground Penetrating Radar is an open access peer-reviewed journal published quarterly by TU1208 GPR Association. TU1208 GPR Association was founded in September 2017 as a follow up of the COST Action TU1208 "Civil engineering applications of Ground Penetrating Radar," to further support cooperation between Universities, research centres, private companies and public agencies active in the Ground Penetrating Radar field. Responsibility for the contents of the manuscripts published on *Ground Penetrating Radar* rests upon the Authors and not upon TU1208 GPR Association or its Members.

All Manuscripts should be submitted at:
http://gpradar.eu/journal/submission.html

All correspondence and communication should be directed to:
Ground Penetrating Radar c/o TU1208 GPR Association
Via Flaminio Ponzio 14, 00153 Rome, Italy
journal@GPRadar.eu

This is **Issue 2**, **Volume 1**, published in **July 2018**. All papers are available in open access at http://gpradar.eu/journal
This issue includes: Editorial, Preface, six papers, Table of Contents, News & Announcements.

ISSN 2533-3100

EDITORIAL

Welcome to Issue 2, Volume 1 of *Ground Penetrating Radar*, the international, peer-refereed, open-access, academic journal designed to advance scientific knowledge and foster innovative engineering solutions in the field of Ground Penetrating Radar (GPR).

I wish to start this Editorial with many thanks to all colleagues who sent me warm messages and congratulations after the publication of the inaugural journal issue, in January of this year; also, I wish to express my deep gratitude to the Members of the Editorial Board and to all contributing Authors who believe in this newborn journal and have chosen *Ground Penetrating Radar* for the publication of their research works.

This issue comes later than expected, but with six interesting papers (see the Preface for an introduction to the papers) and a series of good news.

The first news item is that a journal section entitled 'News & Announcements' is inaugurated with this issue, dedicated to hosting the following content:

- Announcements regarding upcoming GPR-related academic activities, such as conferences and conference sessions, workshops, training schools, scientific contests and awards;
- Reviews of recent GPR-related books, submitted by their Authors and/or Publishers;
- Selected advertisements.

If you are interested in contributing to this section of the journal, please contact the editorial office at journal@gpradar.eu.

The second piece of news is that a Special Issue is being launched: the last issue of Volume 1 (to be published in December 2018) will be a collection of extended papers resuming contributions presented during the three days workshop 'Applications of Ground Penetrating Radar and related Science Management aspects' held in Split (Croatia), on 27-29 June 2018, in the framework of the 3rd International Conference on Smart and Sustainable Technologies (SpliTech 2018). This Special Issue is being edited by Prof. Dragan Poljak (University of Split, Croatia) and myself; submissions are open to scientists and experts who participated in the workshop and their co-Authors, only.

The third news is a scientific contest, open to Members of TU1208 GPR Association, only. Among all papers submitted to *Ground Penetrating Radar* from 1 September 2018 to 20 April 2019, whose Corresponding Author is a Member of TU1208 GPR Association at the time when the paper is submitted, the Editorial Board of the journal will select: (i) the Best Paper having an early-career investigator as

Corresponding Author, (ii) the Best Paper having a female scientist as Corresponding Author, (iii) the Best Paper having a scientist from an Inclusiveness Target Country as Corresponding Author. An early-career investigator is a scientist who received his PhD degree since no more than eight years at the time when the paper is submitted. Inclusiveness Target Countries currently are: Albania, Bosnia-Herzegovina, Bulgaria, Cyprus, Czech Republic, Estonia, Croatia, Hungary, Lithuania, Latvia, Luxembourg, Malta, Montenegro, Poland, Portugal, Romania, Slovenia, Slovakia, the former Yugoslav Republic of Macedonia, Republic of Serbia and Turkey. The Corresponding Authors of the awarded papers will receive award certificates and TU1208 GPR Association will support their participation in the 10th International Workshop on Advanced Ground Penetrating Radar (IWAGPR 2019, Rome, Italy, 3-5 July 2019) by reimbursing their conference registration fee. This contest is based on an idea proposed by Dr Pier Matteo Barone (American University of Rome, Italy).

All *Ground Penetrating Radar* papers are processed and published in true open access, free to both Authors and Readers, thanks to the generous support of TU1208 GPR Association and to the voluntary efforts of the journal Editorial Board. This issue is also supported by Adapis Georadar Teknik Ab (georadar.eu) and IDS Georadar s.r.l. (idsgeoradar.com): I would like to thank both companies personally, as well as on behalf of the journal Editorial Board, Authors and Readers.

Do you have suggestions to improve this journal? Would you like to leave a comment or ask a question? We are looking forward to hearing from our Readers! Send us a message at gpradar.eu/journal/contact.html or journal@gpradar.eu. Would you like to guest edit a Special Issue for *Ground Penetrating Radar*? Send us a proposal! If you wish to participate in the Editorial Board, please send us your motivation letter and curriculum vitae.

We hope to receive several interesting papers in the upcoming weeks!

The Editor-in-Chief
Lara Pajewski

PREFACE

I am delighted and honoured to introduce the second issue of the first volume of *Ground Penetrating Radar*, which includes six papers authored by scientists from 13 institutes in 11 countries (Belgium, Croatia, Czech Republic, France, Italy, Poland, Portugal, Serbia, Spain, Turkey, and United States of America).

The issue is opened with a paper entitled "**GPR system performance compliance according to COST Action TU1208 guidelines**," authored by myself, Milan Vrtunski, Željko Bugarinović, Aleksandar Ristić, Miro Govedarica, Audrey van der Wielen, Colette Grégoire, Carl Van Geem, Xavier Dérobert, Vladislav Borecky, Salih Serkan Artagan, Simona Fontul, Vânia Marecos, and Sébastien Lambot. Four tests are proposed, which can be carried out to evaluate the signal-to-noise ratio, short-term stability, linearity in the time axis, and long-term stability of the Ground Penetrating Radar (GPR) signal. The paper includes a thorough introduction to the topic, a full description of the tests, as well as results obtained by executing the tests on five pulsed control units and nine antennas with central frequencies from 400 MHz to 1.8 GHz. The performed measurements are not representative enough to establish absolute thresholds for the tests; nonetheless, they provide useful indications about values that one may obtain when testing GPR equipment, if the equipment is working reasonably well. Also, by periodically repeating the tests on the same equipment, it is possible to detect any significant shift from previously obtained values, which may imply that the GPR unit or antenna under test is not working in a normal or satisfactory manner. The Authors welcome any comments and suggestions to improve the tests. Moreover, we hope that the tests will be executed by other research teams, manufacturers and private end-users in the near future, on a wider variety of control units and antennas, on both brand new and older equipment; by sharing information about the obtained results, the GPR community can jointly establish reasonable thresholds for the tests, which can help to distinguish between equipment working properly and flawed equipment.

The second paper is entitled "**Frequency domain deterministic-stochastic analysis of the transient current induced along a ground penetrating radar dipole antenna over a lossy half-space**" and is authored by Anna Šušnjara, Dragan Poljak, Vicko Dorić, Sébastien Lalléchère, Khalil El Khamlichi Drissi, Pierre Bonnet, and Françoise Paladian. This paper presents a stochastic analysis of the transient current induced along a dipole antenna over a lossy half-space. The electromagnetic formulation of the problem is based on the Pocklington's integro-differential equation in the frequency domain, which is solved by means of the Galerkin-Bubnov indirect boundary element method; the transient solution is obtained by using the inverse fast

Fourier transform. By exploiting the Stochastic Collocation technique, the Authors investigate the variability of the current as a function of the soil permittivity, soil conductivity, and dipole distance from the half-space. Beyond the specific simulation case considered by the Authors, this paper represents a successful and valuable example of application of the Stochastic Collocation method in the GPR field, which may inspire other researchers to employ a similar approach in their simulations. Indeed, in GPR electromagnetic modelling problems there often is uncertainty on the input parameters, because some geometrical and/or physical properties of the scenario may be partly or entirely unknown. In such cases, the simple but robust Stochastic Collocation method can be effectively used to determine relevant statistics about the GPR responses and to assess confidence intervals in the numerical results.

Still concerning GPR antennas and full-wave methods for the solution of electromagnetic radiation and forward-scattering problems, the third paper is entitled "**Electromagnetic modelling and simulation of a high-frequency Ground Penetrating Radar antenna over a concrete cell with steel rods**;" it is authored by Alessio Ventura and myself. In this work, a high-frequency GPR antenna placed over a reinforced concrete cell is simulated by using the commercial software CST Microwave Studio, which implements the Finite-Integration technique. This study was mostly carried out during the Master thesis in Electronic Engineering of the first Author, under my supervision. Geometrical and physical information about the antenna was taken from the PhD thesis of Dr Craig Warren, where the same device was experimentally characterized and numerically modelled by using the Finite-Difference Time-Domain software GprMax3D; the reinforced concrete cell, instead, is one of the reference simulation scenarios of COST (European Cooperation in Science and Technology) Action TU1208 "Civil engineering applications of Ground Penetrating Radar." The paper comprises an explanation of how the CST model was built, followed by results calculated with the antenna above the concrete structure; comparisons with a simplified model, where the physical structure of the antenna is not taken into account, are also presented. The significant differences between the results of the realistic model and those of the simplified model confirm the importance of including accurate models of the actual antennas in GPR simulations. The results presented in the paper are available for download as 'Supplementary materials;' this gives me the opportunity to remind Readers that *Ground Penetrating Radar* encourages scientists to publish methods and results in as much detail as possible, as well as to enclose supplementary materials to their papers (e.g., data, software, videos, presentations, and any other useful electronic files).

The three papers introduced above stem from COST Action TU1208 "Civil engineering applications of Ground Penetrating Radar." COST is the longest-running European framework supporting trans-national cooperation among

researchers, engineers and scholars. COST Actions are bottom-up science and technology networks where scientists, professionals and stakeholders can jointly develop their own ideas; they are active through a range of networking tools, such as workshops, conferences, training schools, short-term scientific missions, and dissemination activities. COST Action TU1208 was running from 4 April 2013 to 3 October 2017; its main objective was to exchange and increase scientific-technical knowledge and experience of GPR techniques in civil engineering, whilst promoting a wider and more effective use of this safe and non-destructive method in the monitoring of structures.

The journal issue continues with the paper entitled "**GPR research in Wojanów railway tunnel, Sudetes mts., Poland**," authored by Adam Szynkiewicz. This is an interesting and detailled case study, where a commercial GPR equipped with three different antennas was used in the context of a geotechnical research carried out for the purposes of designing the renovation of Wojanów railway tunnel, in Poland. GPR measurements were performed above and inside the tunnel, namely along the ceiling of the tunnel, along the tunnel walls, and all along the tunnel floor (on the railway tracks, as well as close to the tunnel walls). The central frequencies of the three antennas were 100 MHz, 250 MHz, and 800 MHz. Most data were analysed in a two-dimensional system; a preliminary analysis in a three-dimensional system was attempted, too. The Author describes how the survey was carried out, how data were processed and interpreted, and how the various antennas were able to provide different kinds of information; the paper provides practical advice and useful recommendations. We are very pleased to host this contribution on *Ground Penetrating Radar*, because case studies dealing with the use of GPR in tunnels are not common in the scientific literature (this is realistically due to the fact that GPR tunnel inspections present considerable practical difficulties) and because of the longstanding experience of the Author in the GPR field, which reflects in the paper.

The journal issue is concluded with two papers coming from an excellent research team, where innovative solutions for suppressing clutter and reducing the corresponding false alarms in Forward-Looking GPR (FLGPR) are presented and validated on experimental data. The main focus is on the use of vehicle mounted FLGPR, equipped with dual band array antennas, for the detection of buried explosive threats, such as mines and improvised explosive devices.

The first paper of this pair is entitled "**Model-based clutter reduction method for forward looking Ground Penetrating Radar imaging**" and is authored by Yukinori Fuse, Borja Gonzalez-Valdes, Jose A. Martinez-Lorenzo, and Carey M. Rappaport. A model-based clutter suppression image processing method, which uses a mask to reduce clutter from the rough ground surface and from objects above the ground, is described and tested. The proposed approach is able to clean the L-Band Synthetic

Aperture Radar (SAR) image obtained by the FLGPR by employing a mixed binary mask, which is produced from L-Band and X-band data; this mask covers only the surface scatterer signals and excludes the signals generated by buried targets within the masked covering area. A new simulated SAR image is created, by exploiting the masked L-Band SAR image; the simulated image, due to the primary clutter objects, is subtracted from the original image, thus providing a clutter-suppressed SAR image without affecting the buried target signals. The performed tests show that the application of the proposed method significantly reduces the false alarm rate.

The subsequent paper, which is the last contribution included in this journal issue, is entitled "**False alarm reduction by target tracking for Forward Looking Ground Penetrating Radar**" and is authored by Yukinori Fuse, Masoud Rostami, Borja Gonzalez-Valdes, and Carey M. Rappaport. In this contribution, a target tracking process is proposed, which can be applied to multiple clutter suppressed SAR images to further reduce the false alarm rate. It is observed that underground objects tend to scatter similarly for most stand-off distances and yield a consistent image, independent of the platform position. Such image consistency from the buried targets is a feature that is exploited to distinguish them from clutter objects. If the position of the FLGPR antennas is accurately measured by Global Positioning System units, while the radar system is moving, the position of the signals on the SAR image can be compared in a selection of frames and the signals that remain at a given position, which are indicative of stationary targets, can be identified, while the clutter signals can be eliminated. Tests performed by the Authors show that false alarms are further reduced by this approach and the detection performance of the radar is improved.

I wish to warmly thank all Authors of these six papers for choosing *Ground Penetrating Radar*. I hope that their scientific efforts and their trust in this journal will be returned back with an effective spreading of their researches. Many thanks also to all researchers and experts involved into the revision process of the papers, for their voluntary efforts.

I am grateful to TU1208 GPR Association (gpradar.eu/tu1208), Adapis Georadar Teknik Ab (georadar.eu), and IDS Georadar s.r.l. (idsgeoradar.com), for supporting the publication of this issue, and to COST (cost.eu) for having funded and supported the Action TU1208 (gpradar.eu).

The Editor-in-Chief
Lara Pajewski

SCIENTIFIC PAPERS

Ground Penetrating Radar
The first peer-reviewed scientific journal dedicated to GPR

GPR System Performance Compliance according to COST Action TU1208 guidelines

Lara Pajewski[1] (corresponding author), Milan Vrtunski[2], Željko Bugarinović[2], Aleksandar Ristić[2], Miro Govedarica[2], Audrey van der Wielen[3], Colette Grégoire[3], Carl Van Geem[3], Xavier Dérobert[4], Vladislav Borecky[5], Salih Serkan Artagan[6], Simona Fontul[7], Vânia Marecos[7] & Sébastien Lambot[8]

[1] Department of Information Engineering, Electronics and Telecommunications, Sapienza University of Rome, Rome, Italy - lara.pajewski@uniroma1.it

[2] Faculty of Technical Sciences, University of Novi Sad, Novi Sad, Serbia - milanv@uns.ac.rs, zeljko91bug@gmail.com, aristic@uns.ac.rs, miro@uns.ac.rs

[3] Belgian Road Research Centre (BRRC), Brussels, Belgium - a.vanderwielen@brrc.be, c.gregoire@brrc.be, c.vangeem@brrc.be

[4] Institut français des sciences et technologies des transports, de l'aménagement et des réseaux (IFSTTAR), Nantes, France - xavier.derobert@ifsttar.fr

[5] University of Pardubice, Pardubice, Czech Republic - vladislav.borecky@upce.cz

[6] Anadolu University, Turkey - ssartagan@anadolu.edu.tr

[7] National Laboratory of Civil Engineering (LNEC), Lisbon, Portugal - simona@lnec.pt, vmarecos@gmail.com

[8] Earth and Life Institute, Université catholique de Louvain, Louvain-La-Neuve, Belgium - sebastien.lambot@uclouvain.be

Abstract

Ground Penetrating Radar (GPR) systems shall be periodically calibrated and their performance verified, in accordance with the recommendations and specifications of the manufacturer. Nevertheless, most GPR owners in Europe employ their instrumentation for years without ever having it checked by the manufacturer, unless major flaws or problems become evident, according to the results of a survey carried out in the context of COST (European Cooperation in Science and Technology) Action TU1208 "Civil engineering applications of Ground Penetrating Radar." The D6087–08 standard, emitted by the American Society for Testing Materials (ASTM International), describes four procedures for the calibration of GPR systems equipped with air-coupled antennas. After a critical analysis of those procedures, four improved tests were proposed by a team of Members of the COST Action TU1208, which can be carried out to evaluate the signal-to-noise ratio, short-term stability, linearity in the time axis, and long-term stability of the GPR signal. This paper includes a full description of the proposed tests and presents the results obtained by scientists from Belgium, Czech Republic, Portugal, and Serbia, who executed the tests on their GPR

https://doi.org/10.26376/GPR2018007

systems. Overall, five pulsed control units and nine antennas were tested (five horn and four ground-coupled antennas, with central frequencies from 400 MHz to 1.8 GHz). While the performed measurements are not representative enough to establish absolute thresholds for the tests, they provide a valuable indication about values that one could obtain when testing GPR equipment, if the equipment is working reasonably well. Moreover, by periodically repeating the tests on the same equipment, it is possible to detect any significant shift from previously obtained values, which may imply that the GPR unit or antenna under test is not working in a normal or satisfactory manner. We also believe that executing the tests described in this paper is a useful exercise to gain awareness about the behaviour of a GPR system, its accuracy and limits, and how to best utilize it.

KEYWORDS: Ground Penetrating Radar (GPR); Antennas; Calibration; System performance compliance; Signal-to-noise ratio; Signal stability; Signal linearity in the time axis.

1. INTRODUCTION

Early Ground Penetrating Radar (GPR) technology was relatively primitive, data presentation was complex and interpretation of results was a difficult task [1]. Over time, the GPR technology has improved in terms of sensitivity, functional form, ease of use and information presentation. Systems have become lighter, more portable and self-contained; efficient data processing algorithms have been developed, the interaction of electromagnetic waves with soil and targets is better understood, and there is a stronger awareness of GPR limitations [2]-[5]. As a consequence, the GPR technique is nowadays increasingly used in a wide range of applications and is considered as a safe and versatile method, which is capable to provide accurate and reliable information in a fast and efficient way [6]-[11]. GPR surveys are successfully conducted in various environments, under conditions that may sometimes change on a daily basis in the context of long surveys. Thanks to the continuing technology and methodology improvements, it is expected that GPR will further advance in the coming years.

High precision and reliability in GPR measurements obviously require systems with very high linearity and stability, generating very low levels of disturbancies.

As is well known, the measurement accuracy is the closeness of agreement between the measured quantity value and the true quantity value of a measurand (e.g., the amplitude of the electric field as a

https://doi.org/10.26376/GPR2018007

function of time, in the GPR case); the sensitivity is a relation between the indication of an instrument and the corresponding change in a quantity being measured. Ideally, the accuracy and sensitivity of a GPR should be constant over its full operating range; in practice, most measurements involve some changes in accuracy and sensitivity and this type of imperfection is referred as non-linearity of the equipment (which is often emphasized at the extremes of the expected operating range). Being aware of the linearity properties of a GPR and understanding their impact on the measured values significantly aids data interpretation and contributes to the effectiveness of a survey; if the equipment demonstrates non-linearity, it may be not properly calibrated in some portions of the operating range, or else some components may be worn, or the signal-to-noise ratio (SNR) may be too low.

Stability is the key to predictability: if the measuring process is changing over time, the ability to use the gathered data for the evaluation of electromagnetic and geometrical properties of media and targets is diminished, and so is the capacity to use GPR results in making decisions. Selectivity is defined as the instrument's insensitivity to changes in factors other than the actual measurand, for instance to environmental factors (humidity, pressure, temperature); an instrument with better selectivity guarantees a higher stability. There are many further factors that may introduce instability in a GPR system, such as internal and external electromagnetic noise, alterations of feeding voltage, antenna shielding problems, mechanical vibrations, variations of antenna matching due to permittivity and conductivity changes in the surveyed media, and more; additionally, as in all electronic devices, the GPR stability can worsen over time due to deterioration or ageing of system components.

Noise is the unwanted electromagnetic energy that interferes with the ability of the receiver to detect the useful signal. Noise is always present in the environment and is also generated within the GPR system. If the level of disturbancies generated by the radar is low, the detection probability of small signals is enhanced [12]. The use of appropriate signal processing procedures can improve the SNR in GPR investigations [13]-[15].

To verify the performance compliance of GPR equipment, suitable stability, linearity and SNR tests should be carried out on a regular

https://doi.org/10.26376/GPR2018007

basis and in a controlled environment, by following procedures that should be standardized. However, few recognized international standards exist in the area of GPR [16] and, to the best of our knowledge, the calibration topic is covered only within one of them, namely in the ASTM D6087 - 08(2015)e1 "Standard Test Method for Evaluating Asphalt-Covered Concrete Bridge Decks Using Ground Penetrating Radar" emitted by the American Society for Testing Materials (ASTM International) [17]; therein, four procedures for testing GPR systems equipped with air-coupled antennas are described. Moreover, reliable GPR manufacturers shall suggest calibration and verification procedures for the equipment they produce.

Besides the poor availability of standards in the field, the importance of periodically testing and calibrating GPR instrumentation is often underestimated in Europe, according to a survey conducted during the Third General Meeting of COST Action TU1208 "Civil engineering applications of Ground Penetrating Radar." This event was held in London, United Kingdom, on 4-6 March 2015, and was attended by 90 participants from 29 countries, from academia and industry: in addition to the only GPR manufacturer participating in the meeting, just a researcher from France, a team of researchers from Belgium, and another researcher from Belgium claimed to have experience on testing the stability, linearity and SNR levels of GPR systems. In particular, the researcher from France stated that in the scientific network of the French Ministry of ecological and solidary transition (MTES), composed by the Institut Français des Sciences et Technologies des Transports, de l'Aménagement et des Réseaux (IFSTTAR, Nantes, France) and the Centre d'études et d'expertise pour les risques, la mobilité, l'environnement et l'aménagement (CEREMA, France), procedures similar to those described in [17] had been executed various times throughout the years, to test the equipment owned by the institute. The research team from Université catholique de Louvain (UCL, Louvain-la-Neuve, Belgium) reported about their studies on the topic, which were published in [18], [19] and are resumed in the following paragraphs. The researcher from the Belgian Road Research Centre (BRRC, Brussels, Belgium) communicated that she executed the procedures of [17] during her PhD thesis (see Appendix 5 of [20]); in particular, she tested a commercial 2.3 GHz ground-coupled antenna, which did not fulfill the thresholds set by the ASTM standard for the long term

https://doi.org/10.26376/GPR2018007

stability and signal to noise ratio, namely because of the short-term noise in the acquired signal. Additionally, a Member from Spain reported about research activities performed in the University of Vigo by her colleagues [21], which are resumed in the following of this section, too.

In [18], the stability over time and repeatability of a frequency-domain and a time-domain GPR system were investigated. The frequency-domain GPR was a combination of a vector network analyser and an 800–5200 MHz horn antenna. The time-domain GPR was a commercial control unit with a 900 MHz bow-tie antenna. Both GPR systems were calibrated several times by performing measurements with the antennas at different heights over a perfect electric conductor (PEC) in the laboratory, as well as over a water layer. Further measurements were performed over a thin water layer and a relatively thick sandy soil layer, as validating media. The frequency-domain GPR turned out to be relatively stable, while the time-domain GPR presented a significant drift, which according to the authors can be accounted for using corrections based on the air direct-coupling waves. Inversions for the thin water layer and the sandy soil layer provided reliable results and showed a high degree of repeatability for both radar systems. Results presented in [18] also show that water- and PEC-based calibrations provide very similar results for the GPR calibration functions, with useful practical implications in case the calibration of a low-frequency antenna is necessary and when a sufficiently large metal plane is not available. Furthermore, the error on the calibration due to inaccurate antenna heights over PEC (or water) yields significant uncertainties on the inversion results for the horn antenna and smaller uncertainties for the bow-tie antenna.

In [19], the time drift of a time-domain GPR with a 900 MHz antenna was quantified over a certain time period (28 hours, non consecutive but in identical situation) and the maximum observed time drift was 0.0978 ns. As a second step of the study, the maximum time and amplitude drift were characterized in the frequency domain, via the calculation of a frequency-dependent ratio, to be multiplied by the original spectrum of the signal in order to illustrate the effects of the drift. Third step of the study was the quantification of the sensitivity of soil characterization (by full-wave inversion) in response to a drift: the overestimation of the dielectric permittivity reached 50% for low

https://doi.org/10.26376/GPR2018007

dielectric permittivity values, whereas the maximum underestimation was 25% for high permittivity values, following a gradient. The error on the estimation of the electric conductivity turned out to be much higher, reaching an extreme of 105.4% for the lowest original values, with an average of 102.5%. These results show that the inaccuracy of recorded GPR data caused by drift phenomena, or more in general by the system instability, can be disastrous for an inverse problem solution.

In [21], several tests were carried out in order to evaluate the short-term and long-term amplitude and arrival-time stability of a time-domain commercial GPR working with three different ground-coupled antennas having central frequencies of 500, 800, and 1000 MHz. The tests were taken and further developed from [22], where procedures for the calibration of GPR equipment were presented; such procedures were in turn taken from a Texas Department of Transportation report [23]. Actually, in [23] eight procedures to test the performance of GPR systems were proposed. Four of them are based on the evaluation of the GPR reflection from a large metal plate and allow measuring the noise-to-signal ratio, the short-term signal stability, the amplitude of the so-called 'end reflection' directly preceding the metal plate reflection (caused by impedance mismatch at the end of the antenna, according to [23]), and the variations in the time-calibration factor; another procedure makes use of a non-reinforced concrete slab placed on top of a metal plate and aims at measuring the signal penetration in concrete; one more procedure, with the antenna pointed directly up into the air, is to measure an "end reflection waveform" (superimposed on every waveform collected by the system, according to [23]). Finally, two procedures allow compensating the bouncing effects of air-coupled antennas mounted on vehicles and evaluating the influence of vehicle speed on GPR amplitudes.

Coming back to [21], inspiration concerning the warm-up time before executing the tests was taken from [24] and the obtained data were used to determine some parameters proposed in [25], as well. The results of [21] show that, after a warm-up time of about 10 minutes, the GPR system under test had high arrival time stability, ensuring correct positioning of the recorded reflections in time. On the other hand, the amplitude stability was not satisfactory; for practical purposes, amplitude instability may cause significant errors in the estimation of the electromagnetic properties of media (for example, when applying the

https://doi.org/10.26376/GPR2018007

procedures customarily used in road pavement investigations for the estimation of the electromagnetic properties of road layers, where the amplitude of the signal reflected by a particular layer is compared with the amplitude of the signal reflected by a metal plate). As suggested in [21], when accurate amplitude values are needed, it is safer to repeat static measurements several times and take an average of the received signals, in order to minimize the amplitude instability effects. All stability tests of [21] were carried out in air and repeated in distilled water; in the latter medium the amplitude stability was significantly improved, which suggests that the examined antennas work better when placed in contact with an absorbent medium having an impedance different than the air (as is expected for ground-coupled antennas).

Following the Third General Meeting, two Members of COST Action TU1208 from Italy and United Kingdom analysed the ASTM SNR test proposed in [17]. They considered a reduced Taylor's expansion up to the second order of the expressions of SNR bias and variance; and, they derived a formula for tuning the SNR threshold according to a fixed target value of the GPR signal stability [26]. Moreover, they executed the SNR test of [17] on a time-domain commercial GPR equipped with three different horn antennas produced by the same manufacturer, having central frequencies of 1 GHz, 2 GHz, and again 2 GHz, to investigate the effects of the antenna frequency on the SNR [26]. While the authors of the present paper appreciate the valuable efforts done in [26], it is the opinion of the authors that the SNR test of [17] is inherently not correct, for reasons explained in Sub-section 2.1 of the present paper.

Before introducing and describing the content of the present paper, a few more studies available in the GPR literature are worth being mentioned.

Various scientific-technical reports from the United States can be found on the web, where the tests proposed in [17], [21] and [23] are suggested; the report [27] is especially interesting and includes, in Appendix B, the description of almost all tests of [21] and [23], plus a procedure for evaluating the metal plate reflection symmetry. In [28] it was recommended to calibrate GPR systems at least once per year, based on the results of the tests described in [27].

In [29], the authors assessed the accuracy of GPR evaluations of propagation velocity and two-way travel time. By using time picks from

https://doi.org/10.26376/GPR2018007

a common midpoint radargram recorded by a GPR equipped with a 200 MHz antenna, confidence limits of the order of 0.01 m/ns were found for velocity estimates; the confidence limits for two-way travel time estimates were of the order of 1 ns. In [30], the velocity inaccuracy level found in [29] was translated to an uncertainty of 12% in the estimated moisture content of a typical soil.

In the recently published paper [31], a new method for the stability evaluation of GPR systems was proposed, based on statistics. Four sets of experiments were carried out in an anechoic chamber and on a sandbox, to compare the stability performances of a commercial impulse GPR system with a 900 MHz ground-coupled antenna and a stepped-frequency GPR system covering the 50 MHz – 4 GHz range, based on a vector network analyser equipped with a pair of homemade bow-tie antennas. The influence of the warm-up time, environmental noise and antenna vibration on the GPR signal instability was investigated. In agreement with [18], it was found that the GPR signal recorded by the stepped-frequency GPR system was more stable than the impulse GPR system (at a cost of a longer sweep time, hence a slower survey speed). A warm-up time of several minutes turned out to be enough for the impulse system, whereas the stepped-frequency system needed no warm-up time (but only because it was warmed up before the measurement, to perform a standard calibration of the vector network analyser and coaxial cable). Environmental noise was found to have a negligible influence on the stability performance of the impulse system, probably because – in normal conditions – the environmental noise is much weaker than the instantaneous electromagnetic power radiated by a GPR. Mechanical vibrations, instead, were found to have a severe impact on the GPR stability (in agreement with [27]): the instability index was increased by more than one order of magnitude in a vibrating condition, compared to a static condition; it is therefore very important to undertake shock-proof measures when using a GPR mounted on a vehicle. Finally, the instability index evaluated by considering the direct wave, only, turned out to be similar to the instability index evaluated by considering the reflection from a metal plate; therefore, by using the index proposed in [31], a simple measurement of the direct signal seems to be enough for the evaluation of the instability of a GPR system (no need of using a metal plate). However, it is the opinion of the authors of the present paper that the

https://doi.org/10.26376/GPR2018007

implementation of the test proposed in [31] may be too difficult for an average GPR user lacking of a scientific background; to make that text executable by everyone, the calculation of the instability index should be incorporated in the GPR system software, which should also assist the user in performing the test.

In this context, the international group of TU1208 Members authoring this paper focused on the standardised procedures described in [17] and critically analysed them. After a series of exploratory experiments carried out at the BRRC, with the aim of better understanding the merits and limits of the ASTM tests, in-depth discussions took place and four improved tests were defined as an output of the 2017 Working Group Meeting "Guidelines for the use of GPR in civil engineering" of COST Action TU1208, held at the COST Association premises in Brussels, Belgium, on 9-13 January 2017. In this paper, the four improved tests are presented (Section 2). They can be used to test GPR systems equipped with both air-coupled and ground-coupled antennas; and, they allow the quantitative experimental evaluation of the SNR (Sub-Section 2.1), signal stability over time (Sub-Section 2.2), signal linearity in the time axis (Sub-Section 2.3), and signal long-term stability (Sub-Section 2.4). During 2017, the four improved test were executed by research teams from Belgium (BRRC), Czech Republic (University of Pardubice, Pardubice), Portugal (National Laboratory of Civil Engineering, LNEC, Lisbon), and Serbia (Faculty of Technical Sciences of the University of Novi Sad, Novi Sad), to verify the performances of five commercial impulse GPR control units and nine commercial antennas with central frequencies ranging from 400 MHz to 1.8 GHz (five horn and four ground-coupled antennas); all the obtained results are reported and commented herein. The tests and experimental results were presented at the Final Conference of COST Action TU1208, held in Warsaw, Poland, on 25-27 September 2017 [32]; the results of measurements carried out in Serbia were also presented at the 2018 European Geosciences Union General Assembly (EGU GA), held in Vienna, Austria, on 8-13 April 2018, in the framework of the session "COST Actions in Geosciences: breakthrough ideas, research activities and results" [33].

The improved tests are being integrated in the guidelines for the use of GPR in civil engineering proposed by the COST Action TU1208. Given the afore-mentioned scarce availability of standards in the area of

https://doi.org/10.26376/GPR2018007

GPR and having observed the existence of inhomogeneous recommendations and use practices in different countries, COST Action TU1208 worked hard on leveraging the gaps and yielded three guidelines for the use of GPR in some civil engineering tasks, plus a volume of recommendations for a safe geophysical prospecting [34]. The main focus of the three guidelines is on GPR road inspection, detection and localization of utilities in urban areas, and assessment of concrete structures (concrete bridges, tunnels and floors). As in all civil engineering applications of GPR it is very important to be aware of the stability, linearity and repeatability of the employed equipment, it was decided to include the four improved GPR performance compliance tests in the guidelines. Such guidelines are currently being refined and finalized, before being published in open access on the website of the Action (www.gpradar.eu).

We hope that the GPR performance compliance tests described in this paper will be executed by other research teams, private end-users and manufacturers, in the near future, on a wide variety of control units and antennas, on both brand new and older equipment; by sharing information about the obtained results, the GPR community can establish reasonable thresholds for the tests, which will help to distinguish between equipment working properly and flawed equipment (so that, in case of flawed equipment, the manufacturer can be contacted to check and possibly repair or calibrate the equipment). Our plans for future work also include investigating how the results of the proposed performance compliance tests translate into accuracy levels of measured physical and geometrical quantities, in various applications of the GPR technique.

2. TESTS

Four tests are proposed, which can be used to test GPR systems equipped with both air-coupled and ground-coupled antennas. They allow experimentally quantifying the SNR (Sub-Section 2.1), signal stability over time (Sub-Section 2.2), signal linearity in the time axis (Sub-Section 2.3), and signal long-term stability (Sub-Section 2.4). These tests can be carried out to assess the performance of a GPR system, in order to gain awareness about its accuracy and precision. They provide a baseline for evaluating the performance of new GPR equipment currently under development. It is also advised to

https://doi.org/10.26376/GPR2018007

periodically repeat the tests on the same equipment, to monitor its performance over time and detect any significant shift from previously obtained values, which may imply that the GPR control unit or antenna under test is not working correctly. The tests proposed herein do not have the ambition to become compulsory; if the user guide of a GPR system includes tests proposed by the manufacturer, they take preference over the procedures described herein.

In all the proposed tests the antenna is placed at a certain height above a square metal plate, to enhance the amplitude of the reflected signal and guarantee repeatability of the test; in this configuration, a number of traces are recorded (see Figure 1, showing photos of the experimental setup used in Serbia and Portugal).

Common parameters for all tests are:

- Warm-up time:

Non negligible variations of results can occur during operation, if the GPR electronic components are not given the possibility to initially reach a temperature that provides the overall system with suitable stability and performance; based on experiments carried out by the authors, the warm-up time should be at least 30 minutes, or according to recommendations by the manufacturer.

- Metal plate size:

Depends on the central frequency of the antenna and is given by:

$$L = D + 2\sqrt{5}\lambda_c \quad (1)$$

where L is the minimum side length of the metal plate, D is the maximum aperture dimension (for aperture antennas, such as horns) or the maximum antenna dimension (for bow-tie and dipole antennas), $\lambda_c = c/f_c$ is the wavelength at the central frequency of the spectrum emitted by the antenna, and c is the light velocity in the air. If the antenna size is not known, then a pejorative assumption of D can be made based on the size of the antenna box and any other useful available information about antenna geometry and position inside the box. A smaller metal plate may be used for tests presented in Sub-sections 2.2-2.4, although not recommended; Eq. (1) has to be strictly respected for the test presented in Sub-section 2.1 (unless information

https://doi.org/10.26376/GPR2018007

about the antenna beam width is available, which can make it possible to use a smaller plate).

(a) **(b)**

FIG. 1 – **(a)** Experimental setup for a 400 MHz ground-coupled antenna in a laboratory of the Faculty of Technical Sciences, in the University of Novi Sad, in Serbia. **(b)** Experimental setup for 1 GHz and 1.8 GHz air-coupled antennas in a laboratory of the National Laboratory for Civil Engineering of Lisbon, in Portugal.

2.1 Signal-to-Noise Ratio (Test 1)

In this test two series of measurements are carried out, at two different distances between the metal plate and the antenna.

For the first series of measurements (see Figures 2(a) and Fig. 3):

- The distance between the metal plate and the antenna is $h_1 = 2\lambda_c$;
- The time window (TW) is at least twice the two-way travel time from the antenna to the metal plate ($TW > 8\lambda_c / c$).
- 100 waveforms are recorded.
- The average reflection amplitude $\langle A_{mp} \rangle$, that is the average peak-to-peak amplitude of the first echo coming from the metal plate, is evaluated.

In Figure 2(a), the sketch of the antenna is meant to represent the set of receiving and transmitting antennas (nowadays, they almost always are two distinct devices, which may be included in a common box or in two separate boxes). The distance h_1 guarantees that the first reflection coming from the metal plate is well separated from the so-called direct wave (as illustrated in Figure 3), which is the pulse

https://doi.org/10.26376/GPR2018007

travelling straight from the transmitting to receiving antenna (or, in horn antennas, the pulse reflected at the bottom of the antenna); this claim is

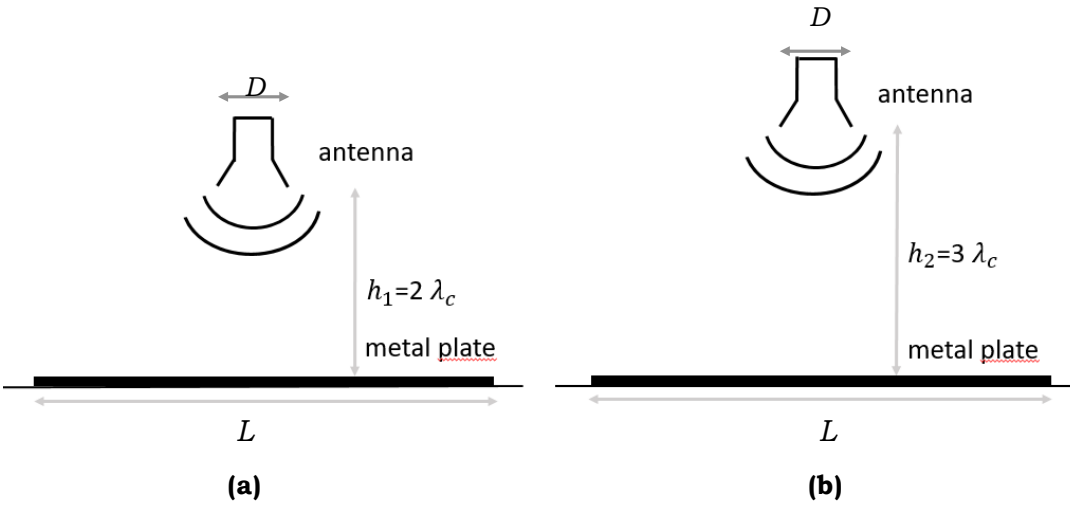

FIG. 2 – Sketches of the experimental setup for Test 1: **(a)** Measurement series 1; **(b)** Measurement series 2.

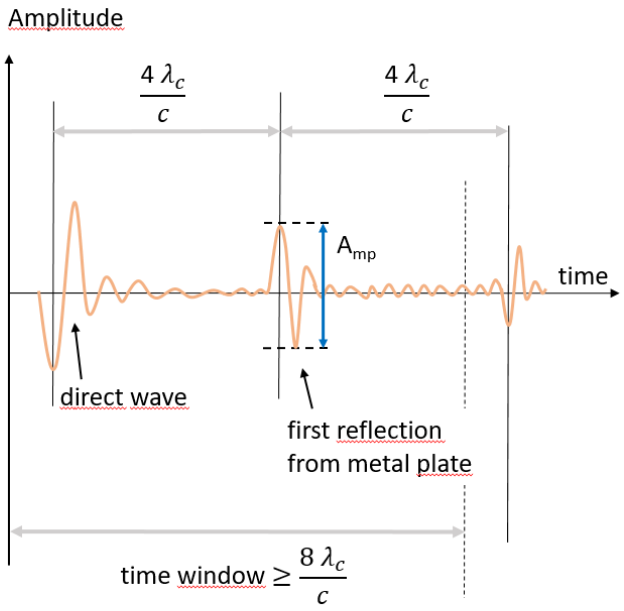

FIG. 3 – Sketch of a GPR trace, to illustrate the choice of geometrical parameters, settings, and quantities to be evaluated, for measurement series 1 of Test 1.

based on the assumption that the pulse emitted by radar is $2\lambda_c/c$ long (or shorter), as is customarily true for ultra wideband pulses popularly used in GPR.

https://doi.org/10.26376/GPR2018007

For the second series of measurements (see Figures 2(b) and 4), the same GPR settings as in the first series are used and, again, 100 waveforms are recorded. The antenna height and the evaluated quantity are different:

- The distance between the metal plate and the antenna is $h_2 = 3\lambda_c$;
- The suggested 'relevant time window' starts $2\lambda_c/c$ after the absolute maximum amplitude of the signal, and is $2\lambda_c/c$ long.
- The average amplitude $\langle A_n \rangle$, that is the average peak-to-peak noise amplitude over the 'relevant time window', is evaluated. Of course noise has an irregular time shape and does not appear as a series of pulses with peak-to-peak amplitudes, it is therefore proposed to evaluate A_n as the difference between the maximum and minimum amplitudes of noise over the considered 'relevant time window'.

An indicator of the signal-to-noise ratio can finally be calculated, by using the following formula:

$$I_{SNR} = \frac{\langle A_{mp} \rangle}{\langle A_n \rangle} \tag{2}$$

The higher this quantity, the better the quality of the signal is. In Section 3, examples of I_{SNR} values obtained by the authors are reported and commented on.

The suggested minimum L value, given by Eq. (1), is to make sure that any unwanted reflection coming from outside the metal plate is received after the metal plate echo when the antenna height is h_1 and after the 'relevant time window' when the antenna height is h_2. Under the simplified assumption of geometrical optics (i.e., by describing the propagation of electromagnetic fields in terms of rays) and with reference to the scheme in Figure 5(a): if $L = D + 2\sqrt{5}\lambda_c$, the two-way travel time from A to B is $6\lambda_c/c$, which is equal to the two-way travel time from B to C plus the pulse time duration, $4\lambda_c/c + 2\lambda_c/c$; this guarantees that reflections coming from outside the metal plate do not affect the results of measurement series 1. In Figure 5(b), the two-way travel time from A to B is $2\sqrt{14}\lambda_c/c \approx 7{,}48\,\lambda_c/c$, which is longer than $6\lambda_c/c$; this guarantees that reflections coming from outside the metal plate do not affect the results of measurement series 2.

https://doi.org/10.26376/GPR2018007

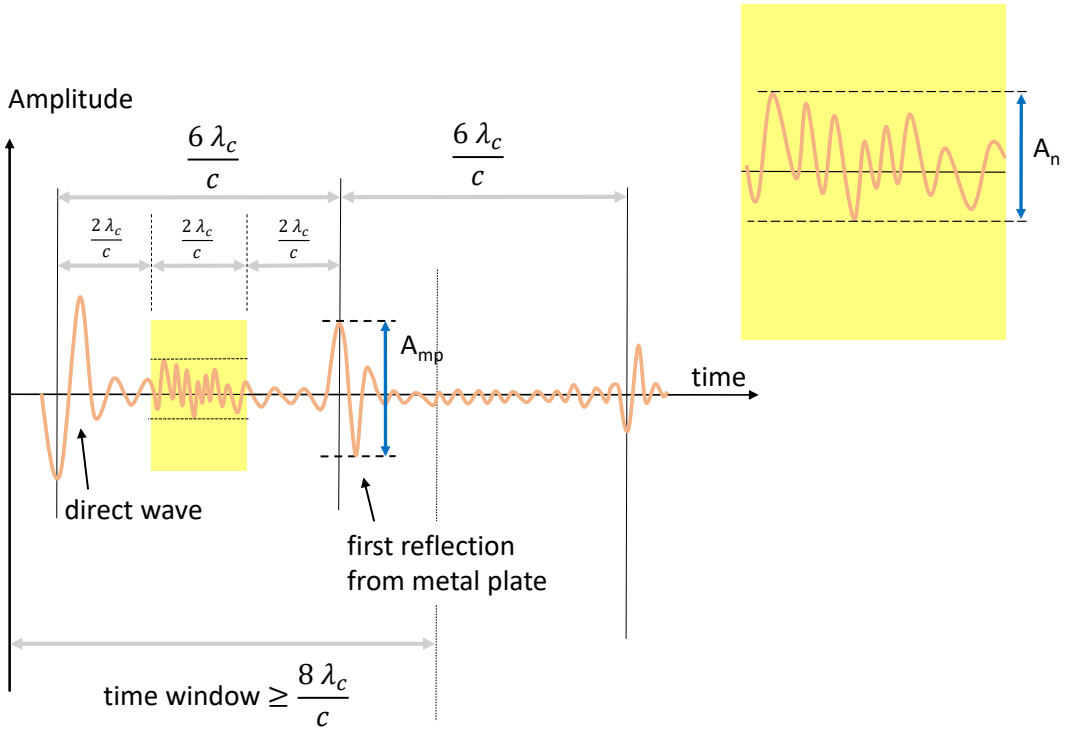

FIG. 4 – Sketch of a GPR trace, to illustrate the choice of geometrical parameters, settings, and quantities to be evaluated, for measurement series 2 of Test 1.

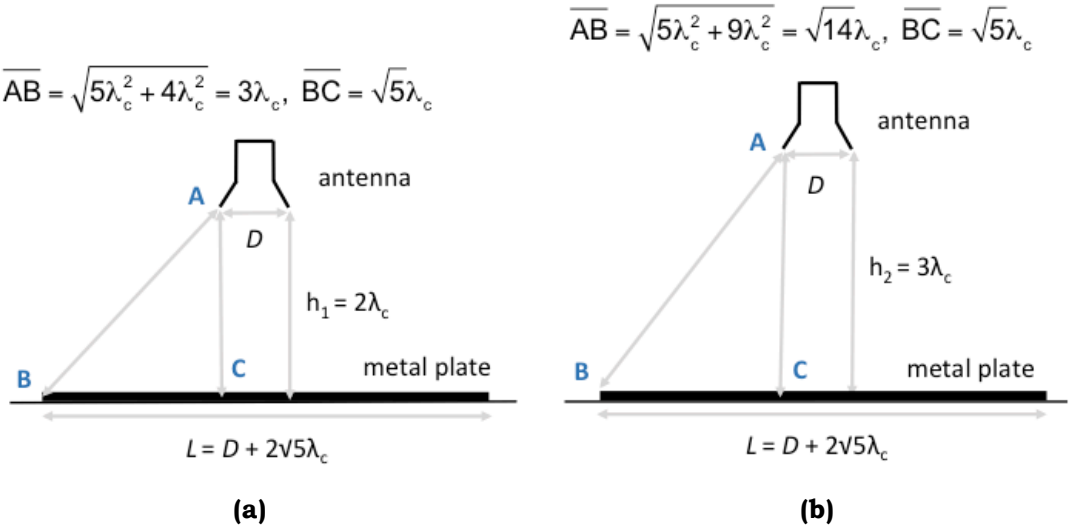

FIG. 5 – Geometrical sketches to explain the choice of the metal plate size.

https://doi.org/10.26376/GPR2018007

By using a larger metal plate, with $L' = D + 2\sqrt{7}\lambda_c$, both measurement series 1 and 2 could be performed with the antenna at h_2 from the metal plate (the values of I_{SNR} would be obviously lower, because the peak-to-peak amplitude of the metal plate echo would be smaller, due to the longer propagation path). As an enlargement of the metal plate of $L' - L \approx 0.82\lambda_c$ may be an issue at low frequencies, it was decided to propose a 'more complicated' test, with two separate series of measurements, in order to keep the metal plate as small as possible. Note also that, if information about the antenna beam width is available, it may be possible to reduce the metal plate size accordingly.

The main differences between Test 1 and the SNR test for air-launched antennas of [17] (paragraphs 6.2.1.1-6.2.1.3), as well as the authors' doubts about the validity of the test of [17], are now discussed.

In [17], it is recommended to position the antenna at a far field distance above a square metal plate, where the far field distance is defined as 'approximately equal to the maximum dimension of the antenna aperture (D)'; the recommended minimum side length of the metal plate is $4D$. The warm-up period is 20-min, or the time recommended by the manufacturer. After warming up the GPR, 100 waveforms are recorded. For each waveform, the signal-to-noise ratio is calculated as the ratio between the signal and noise levels; the signal level is defined as the amplitude of the echo from the metal plate, whereas the noise level is defined as the maximum amplitude occurring after the metal plate reflection and up to the 50% of the time window normally used with the antenna. Finally, the average signal-to-noise value of the 100 waveforms is calculated and taken as the signal-to-noise of the system. In [17], it is stated that this value should be greater than or equal to 20 (+26.0 dB).

A first doubt is concerned with the far field distance definition used in [17]. As is widely stated in the antenna literature, such definition is adequate for measuring the properties of antennas with $D \leq \lambda_c$, only, whereas for larger antennas the far field distance is generally taken as $2D^2/\lambda_c$. For pyramidal horns, which are popular air-launched solutions for GPR applications, a much longer distance than $2D^2/\lambda_c$ may be necessary to measure the far field antenna properties, due to the large phase deviations across their apertures [35]. While the far field distance is not correctly defined in [17], the opinion of the authors is that the SNR is a quantity that can be measured in the near field, too,

https://doi.org/10.26376/GPR2018007

therefore the inaccurate definition taken for the far field distance does not compromise the feasibility of the test. Nevertheless, at the suggested distance between the metal plate and the antenna, the first metal plate echo may arrive immediately after the direct wave if the pulse length is $2\lambda_c/c$; in other words, unless the pulse emitted by the GPR is significantly shorter than $2\lambda_c/c$, the measured trace will consist of the direct wave immediately followed by a sequence of multiple metal plate reflections, with no possibility to measure noise levels in between the echoes. It is the opinion of the authors that this is one of the main faults of the SNR test of [17], which makes it inapplicable in most cases.

Another major problem of the SNR test of [17] is the indicated time interval for the measurement of the noise level. As already mentioned, the noise level is defined in [17] as the maximum amplitude after the first metal plate reflection, up to 50% of the time window normally used with the antenna. Provided that a 'normally used time window' is a questionable concept, because the time window depends on the survey objectives and on the electromagnetic properties of the investigated materials, it is highly probable that this procedure leads to mistake the maximum amplitude of the second reflection coming from the metal plate as the level of noise. For example, in [26] the SNR test of [17] was applied to a 1-GHz horn (λ_c= 30 cm) and two 2-GHz horns (λ_c= 15 cm). Each antenna was tested at three different distances from the metal plate: h_A = 30 cm, h_B = 40 cm and h_C = 50 cm. Therefore, the two-way travel time from the antenna to the metal plate and back to the antenna was t_A= 2 ns, $t_B \approx$ 2.7 ns and $t_C \approx$ 3.3 ns in the three cases, respectively. The time window was set to 25 ns for the 1-GHz horn and to 15 ns for the 2-GHz horns. The observation window for the evaluation of the noise level started after the first metal plate echo and ended at 12.5 ns for the 1-GHz horn, at 7.5 ns for the 2-GHz horns. Accordingly, the second reflection coming from the metal plate was always included in the noise level observation window.

It is not clear whether [17] suggests to measure the maximum absolute amplitude or the maximum peak-to-peak amplitude of signal and noise. It is also noticed that the warm up period suggested in [17] is shorter than the one proposed in this paper. Based on the results of the tests carried out by the authors, 20 min does not seem enough for many GPR systems to reach stability (see Sub-section 2.4); this is in agreement with the ASTM D4748 - 10(2015) "Standard Test Method for

https://doi.org/10.26376/GPR2018007

Determining the Thickness of Bound Pavement Layers Using Short-Pulse Radar" [36], where it is advised to warm up the GPR system prior to a survey for a period recommended by the manufacturer, typically between 30 minutes and 1 hour (paragraph 8.2). Finally, although the SNR test of [17] is recommended for air-launched antennas, only, the (faulty) procedure seems applicable to ground-coupled antennas, too, once the practical problem of how to lift them is solved.

2.2 Signal Stability (Test 2)

To test the signal stability, the same test configuration as in Test 1 is used, with h_1. The time window is at least twice the two-way travel time from the antenna to the metal plate ($TW > 8\lambda_c/c$) and 100 traces at the maximum data acquisition rate are recorded. An indicator of the signal stability can be calculated by using the following formula:

$$I_{Stability} = (A_{\mathrm{MAX}} - A_{\mathrm{min}})/A_{\mathrm{avg}} \quad (3)$$

where A_{MAX} is the maximum and A_{min} is the minimum peak-to-peak amplitude of the metal plate reflection, selected among all 100 recorded traces, and A_{avg} is the average peak-to-peak amplitude of the metal plate reflection. The smaller the quantity $I_{Stability}$, the better is the stability of the system. In Section 3, examples of $I_{Stability}$ values obtained by the authors are reported and commented on.

The ASTM stability test is described in paragraphs 6.2.2.1-6.2.2.2 of [17]. The same test configuration as in the SNR ratio test is used; 100 traces are recorded at the maximum data acquisition rate and the signal stability is calculated by using an equation similar to Eq. (2), where A_{avg} is the average trace amplitude of all traces instead of the average peak-to-peak amplitude of the metal plate reflection.

As far as the experimental set-up and GPR settings are concerned, differences between the signal stability test proposed herein and the ASTM stability test were already discussed in Section 2.1. For this test, those differences are of minor importance because noise levels are not measured. In the ASTM stability test it is not clear whether absolute amplitudes or peak-to-peak amplitudes should be measured.

2.3 Linearity in the time axis (Test 3)

In Test 3, the same test configurations as in Test 1 are used. Additionally, measurements in a third configuration are carried out, with

https://doi.org/10.26376/GPR2018007

$h_3 = 2.5\,\lambda_c$ (see Figure 6). The time window is at least twice the two-way travel time from the antenna to the metal plate at the longest distance h_2 ($TW > 12\lambda_c/c$). A single waveform is recorded per configuration. For each configuration i (i = 1, 2, 3), corresponding to h_i, the time delay Δt_i is determined: this is defined as the difference between the absolute maximum amplitude of the direct wave and the absolute maximum amplitude of the echo coming from the metal plate. The following absolute differences are then calculated: $T_{21}=|\Delta t_2 - \Delta t_1|$; $T_{31}=|\Delta t_3 - \Delta t_1|$. The corresponding speed factors C_{21} and C_{31} are calculated as:

$$C_{21} = (h_2 - h_1)/T_{21} \tag{4}$$

$$C_{31} = (h_3 - h_1)/T_{31} \tag{5}$$

The relative variation in the measured speed can be finally evaluated, as follows:

$$Sv_{rel} = \frac{2|C_{21} - C_{31}|}{C_{21} + C_{31}} \tag{6}$$

The smaller the quantity Sv_{rel} the better is the linearity of the system in the time axis. In Section 3, examples of Sv_{rel} values obtained by the authors are reported and commented on.

While executing this test, a special attention must be paid to the accuracy of height measurements and the horizontality of the antennas: any error induces notable bias in the evaluation of Sv_{rel} (see the relevant discussion in Section 3).

The original ASTM linearity test is described in paragraphs 6.2.3.1-6.2.3.2 of [17]. The same test configuration as in the SNR ratio test is used, except that any reflecting object can replace the metal plate. Measurements are performed at three different distances between the antenna and reflector, which are defined as distances corresponding to 15%, 30% and 50% of the time window normally used with the system. The variation in time calibration factor is calculated with a formula similar to Eq. (6), without the modulus. Substantially, our test is the same as in [17], but the metal plate is used as reflector, and the three considered distances between the antenna and the reflector are different than in [17].

https://doi.org/10.26376/GPR2018007

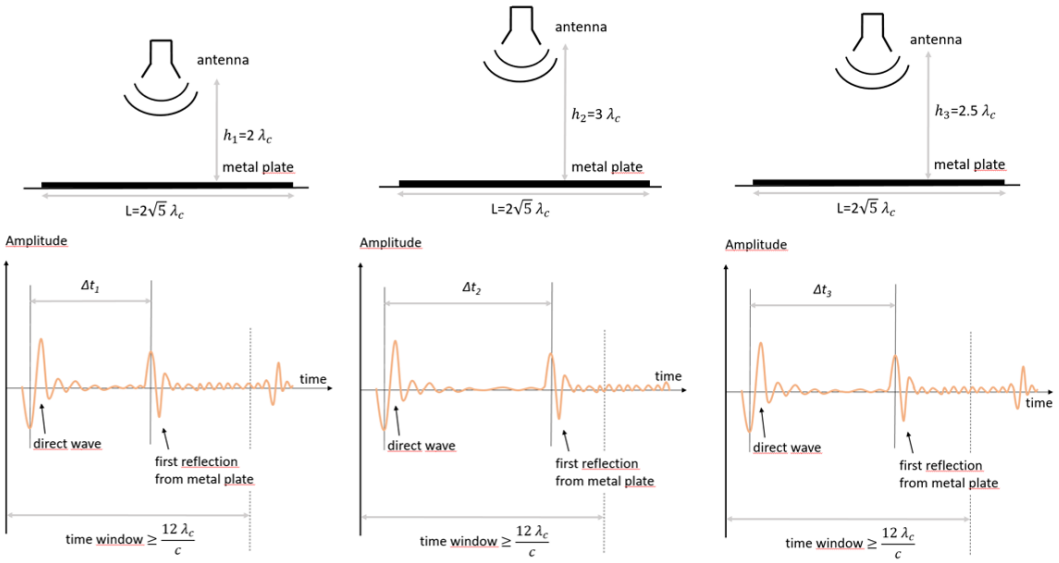

FIG. 6 – Sketches of the experimental setup for Test 3, and GPR traces: **(a)** Measurement series 1; **(b)** Measurement series 2; **(c)** Measurement series 3.

2.4 Long–term stability (Test 4)

In Test 4, the same test configuration as in Test 1 is used, with h_1. The time window is at least twice the two-way travel time from the antenna to the metal plate ($TW > 8\lambda_c/c$). Every minute, for at least 120 minutes, 10 waveforms are recorded. Hence, at least 1200 traces are recorded in total, and it is even better if traces are recorded for a longer time (e.g., a time similar to the length of the longest surveys carried out with the equipment under test). For each waveform w (w = 1, … , T, being T the total number of traces) the peak-to-peak amplitude A_w of the metal plate first echo is determined. The sliding-average amplitudes M_q (q = 1, …, T – (N – 1)) are then calculated, by using the following formula where the suggested value for N is 10:

$$M_q = \frac{1}{N}\sum_{j=0}^{N-1} A_{q+j} \tag{7}$$

The sliding-average amplitudes M_q are then plotted against time (or as a function of q). Realizing such a graph helps to gain awareness about the behaviour over time of the GPR system at hand and allows discovering how long is the warm-up time needed by the system. An

https://doi.org/10.26376/GPR2018007

example is presented in Figure 7 (data are from the BRRC): in this case, waveforms were recorded for 180 minutes; it can be observed that about 30 min of warming up are necessary, moreover a drift occurring after using the antenna for about 100 min can be noticed; Based on preliminary tests carried out by the BRRC, the long-term stability of GPR systems seems to be significantly affected by atmospheric conditions; however, more tests are necessary to confirm this remark.

The long-term stability factor $I_{LTStability}$ is defined as the maximum between the following two quantities:

$$Q_1 = \frac{M_{\mathrm{MAX}} - A_{1w}}{A_{1w}} \tag{8}$$

and

$$Q_2 = \frac{|M_{\mathrm{min}} - A_{1w}|}{A_{1w}} \tag{9}$$

where M_{MAX} and M_{min} are the maximum and minimum values of the sliding-average amplitudes after the warm up and A_{1w} is the first (reference) trace after the warm up (note that A_{1w} might be replaced by M_1 in Equations (8) and (9), i.e., it makes sense as well to consider the first sliding-average amplitude after the warm up as a reference, instead of A_{1w}). The smaller the long-term stability factor, the better is the long-term stability of the system. In Section 3, examples of results obtained by the authors are reported and commented on.

The original ASTM long-term stability test is slightly different and is described in paragraph 6.2.4.1 of [17]. The same test configuration as in the SNR test is used. The GPR is allowed to operate for 120 minutes and a waveform every minute is recorded. The long-term stability factor is calculated as the difference between the largest amplitude of metal plate reflection measured between 20 and 120 minutes, and the amplitude measured after 20 minutes, normalized to the amplitude measured after 20 minutes. In the test proposed herein, the 20 minutes time is replaced by the warm-up time (which can change significantly among different systems), moreover a higher number of traces are recorded and the concept of sliding-average amplitudes is used, because usually amplitudes show large oscillations over a short time. The amplitude of those short-term variations can be estimated from the

https://doi.org/10.26376/GPR2018007

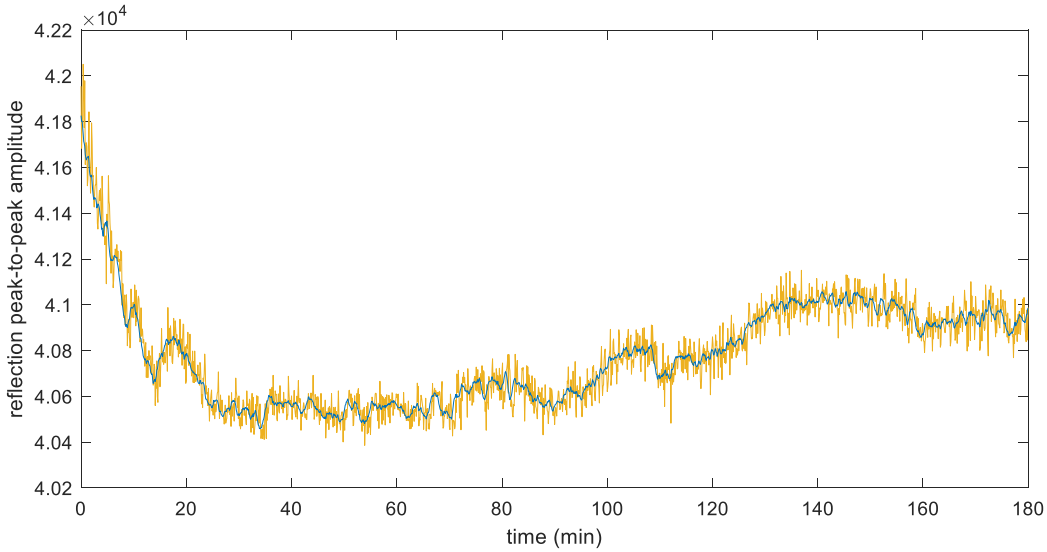

FIG. 7 – Example of graph showing the values of sliding averages (M_q) against time (dark blue line) and all the peak-to-peak amplitudes A_w (yellow line).

results of Test 2 and can rise up to 20% [20]; the BRRC reported them to be up to 3%, with the antennas they tested in the framework of the present research work.

3. RESULTS AND DISCUSSION

During 2017, the tests presented in Section 2 were executed in Belgium (BRRC), Czech Republic (University of Pardubice, UP), Portugal (National Laboratory of Civil Engineering, LNEC), and Serbia (Faculty of Technical Sciences of the University of Novi Sad, FTS).

As is resumed in Table I, five commercial impulse control units and nine commercial antennas were tested (five horn antennas and four ground-coupled antennas). One of the FTS antennas was dual-frequency and was tested as two individual antennas, with central frequencies of 400 MHz and 900 MHz. The BRRC and LNEC tested control units are the same model (GSSI SIR 20) and both laboratories tested them with a 1 GHz horn manufactured by GSSI; it is therefore especially interesting to compare the results obtained by BRRC and LNEC on the raw data gathered with the 1 GHz antenna (note that 512 samples per trace were recorded at BRRC, whereas 256 and 1024 samples per trace were recorded at LNEC, with this antenna). All of the tested antennas are

https://doi.org/10.26376/GPR2018007

regularly used in fieldwork and none of them had showed signs of malfunctioning before tests were performed.

Note that at LNEC only Tests 1 and 2 were carried out. Note also that the UP team used a smaller metal plate than what is suggested in the tests (see Eq. (1)). Moreover, the UP team carried out Test 3 at different distances between antenna and metal plate than those suggested in the tests (in particular, the UP values were h_1=34 cm, h_2=68 cm and h_3=113 cm); nonetheless, it was decided to include the UP results in this paper.

All obtained results are summarized in Table II.

While performing the tests, it was observed that the maximum amplitude of the direct wave is not always the absolute maximum amplitude of the recorded trace: in most cases, the amplitude of the metal plate reflection is indeed stronger (this is likely due to a reduction of the direct wave implemented by the manufacturers in the tested GPR systems). Furthermore, it was observed that the first collected sample has always a random value, which can be larger than any reflection and shall be discarded.

In Figure 8, results of Tests 1 and 2 obtained on raw and filtered data are compared through histograms; only BRRC and LNEC results are considered in this figure, because FTS and UP always worked with raw data. In most cases, results obtained on filtered data are better than those obtained on raw data. Results obtained for the 1 GHz BRRC antenna are worse than results obtained for all other antennas, including the identical 1 GHz antenna from LNEC, in both Tests 1 and 2, which is an alarm bell on the conditions of the antenna.

In Figure 9, results of Tests 1 and 2 obtained on raw data are compared. Only three antennas show a SNR better than 20. For all antennas, the indicator of the short-term signal stability is higher than 2.8%. Results obtained for the 0.9 GHz UP antenna are significantly worse than results obtained for all other antennas, in both Tests 1 and 2; it is likely that this antenna is not working very well, however it has to be kept in mind that the UP metal plate was too small and this reduces the reliability of the UP results which could be affected by reflections coming from the surrounding environment. The 2 GHz UP antenna shows the highest SNR and not very good value of stability.

https://doi.org/10.26376/GPR2018007

TABLE I – TESTED ANTENNAS, SUMMARY.

Institution	Tested GPR control units and antennas	Performed tests	Settings and Remarks
Faculty of Technical Sciences, Novi Sad, Serbia (FTS)	Control unit: GSSI SIR 3000 Ground coupled antennas: GSSI 0.4 GHz GSSI 0.9 GHz The antennas were purchased in 2003 (0.4 GHz) and 2009 (0.9 GHz). A rough estimate for the number of working hours is 1000 h for the 0.4 GHz antenna and 600 h for the 0.9 GHz antenna.	All tests	- Side length of the metal reflector: 3.5 m (0.4 GHz antenna) and 1.7 m (0.9 GHz antenna). - Samples per trace: 512. - All tests were performed on raw data.
Belgium Road Research Centre, Brussels, Belgium (BRRC)	Control unit: GSSI SIR 20 Horn antennas: GSSI 1 GHz GSSI 2 GHz All equipment was purchased in 2010. A rough estimate for the working hours of the tested antennas is: 150 h for the 1 GHz antenna, 500 h for the 2 GHz antenna.	All tests	- Side length of the metal reflector: 1.5 m for both antennas. - Samples per trace: 512. - Tests were performed on both raw and filtered data. The applied filters are: - FIR BP 0.25-3 GHz; - FIR BP 0.25-5 GHz; - GSSI NoiseFilter.
University of Pardubice, Pardubice, Czech Republic (UP)	Control units: IDS RIS HiPave, IDS DAD MCH FastWave Ground coupled antennas: IDS 0.4 GHz IDS 0.9 GHz Horn antennas: IDS 2 GHz All equipment was purchased in 2013. A rough estimate for the total working hours of the tested equipment is 200 h.	All tests	- Side length of the metal reflector: 1 m. - Samples per trace: 512. - All tests performed on raw data.
National Laboratory for Civil Engineering, Lisbon, Portugal (LNEC)	Control unit: GSSI SIR 20 Horn antennas: GSSI 1 GHz GSSI 1.8 GHz Date of purchase and estimation of working hours not available.	Tests 1, 2	- Rectangular metal reflector, 1 m × 2 m. - Tests performed at 256 and 1024 samples per trace with 1 GHz horn, 512 and 1024 samples per trace with 1.8 GHz horn. - Tests performed on raw and filtered data. The applied filters are: - IIR 0.1-1 GHz; - FIR 0.5-3 GHz; - IIR 0.1-2 GHz; - FIR 0.5-5 GHz.

https://doi.org/10.26376/GPR2018007

TABLE II – TEST RESULTS, SUMMARY.

	Antenna	Filter	SNR	Signal Stability	Linearity in time axis	Long Term Stability
1	FTS 0.4 GHz	Raw	10.58	7.91	5.18	2.44
2	FTS 0.9 GHz	Raw	12.48	2.88	2.99	1.57
3	BRRC 1 GHz	Raw	7.24	10.61	4.26	0.92
4	BRRC 1 GHz	FIR	9.70	10.96	3.17	-
5	LNEC 1 GHz	Raw	17.64	5.26	-	-
6	LNEC 1 GHz	FIR-IIR	20.35	2.81	-	-
7	LNEC 1.8 GHz	Raw	15.81	3.89	-	-
8	LNEC 1.8 GHz	FIR-IIR	28.07	1.59	-	-
9	BRRC 2 GHz	Raw	16.21	4.51	6.29	0.69
10	BRRC 2 GHz	FIR	17.45	3.10	3.91	-
11	BRRC 2 GHz	GSSI NF	22.00	2.54	4.56	0.65
12	UP 0.4 GHz	Raw	9.75	4.08	4.88	0.14
13	UP 0.9 GHz	Raw	1.19	15.89	3.39	0.63
14	UP 2 GHz	Raw	23.74	12.18	2.99	1.22

In Figure 10, results of Tests 3 and 4 obtained on raw data are compared. Concerning the linearity in the time axis, the relative variation in the measured speed is always higher than 2.9%. The long-term stability factor is always lower than 3%; the results obtained for the 0.9 GHz UP antenna are worse than those obtained for the other antennas, which may be due to the fact that the antenna is not working well, or to the use of a small metal plate, or else to a scarce accuracy in measuring the distances between metal plate and antenna. Actually, it has been observed by the BRRC research team that results of Test 3 are highly variable and strongly dependent on the laboratory precision; in particular, an error of 1 mm in the measurement of the antenna position can yield an error larger than 2% in the test results. Additionally, it may be appropriate to modify the procedure of Test 3 and use mean values calculated out of, e.g., 100 traces, instead of basing the evaluation of the short-term stability on single waveforms, because of the significant variation of the results that can be observed if measurements are

https://doi.org/10.26376/GPR2018007

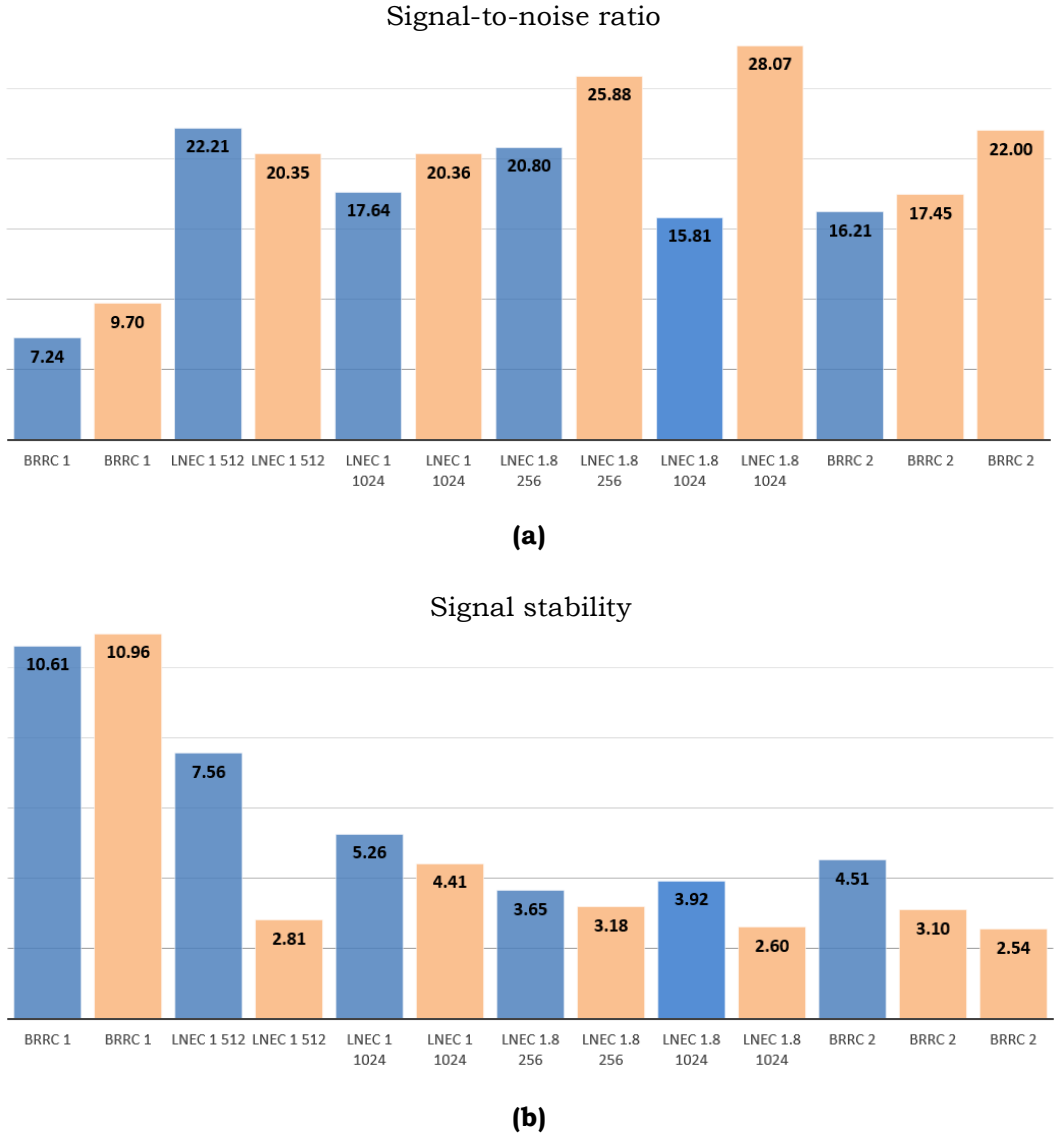

FIG. 8 - Results of Tests 1 **(a)** and 2 **(b)**, raw and filtered data, BRRC and LNEC only.

repeatedly carried out as suggested in Sub-section 2.3. In particular, the BRRC research team reported that, for a given configuration, the relative variation in the measured speed changed from 0.9% to 17.6%, by repeating the evaluation many times. And so, the BRRC results of Test 3 presented in this paper make already use of mean values calculated out of 100 traces, instead of making use of values calculated out of single traces.

https://doi.org/10.26376/GPR2018007

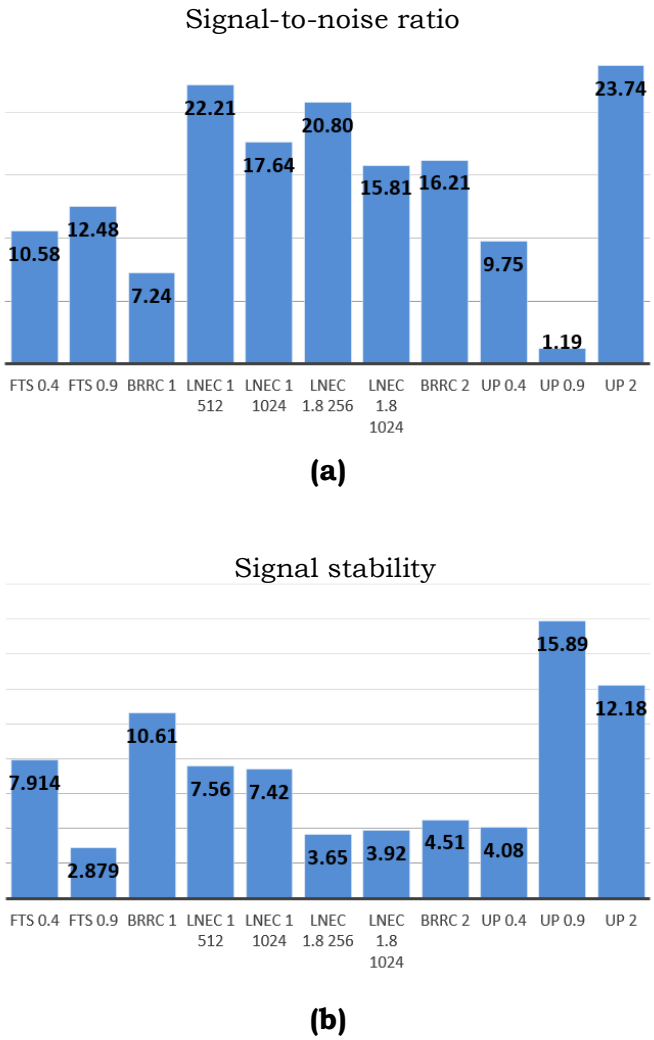

FIG. 9 - Results of Tests 1 **(a)** and 2 **(b)**, raw data only.

Finally, with reference to Test 4, in Figure 11 the sliding averages (M_q) are plotted as a function of time for the 2 GHz antenna owned by the BRRC; results in Figure 11(a) were obtained with cold weather and results in (b) were obtained with warm weather. It therefore seems that the results of the tests (and the behaviour of GPR equipment) are strongly affected by the atmospheric conditions; however, more experiments are necessary to confirm this remark and be sure that the weather is the origin of the observed differences.

https://doi.org/10.26376/GPR2018007

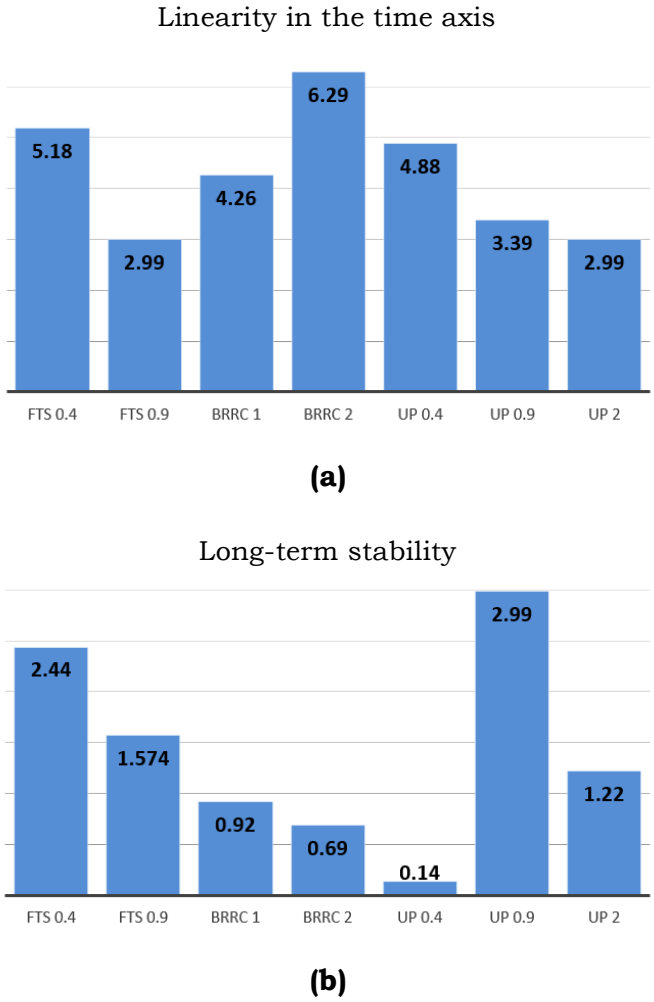

FIG. 10 - Results of Tests 3 **(a)** and 4 **(b)**, raw data only.

4. CONCLUSIONS

This paper deals with the design and execution of new experimental tests for assessing the performances of Ground Penetrating Radar (GPR) equipment. After a literature review and a critical analysis of the D6087–08 standard emitted by the American Society for Testing Materials (ASTM International), where typical procedures for the calibration of GPR systems with air-coupled antennas are described, four improved tests were proposed by a team of Members of COST (European Cooperation in Science and Technology) Action TU1208 "Civil engineering applications of Ground Penetrating Radar." These four tests

https://doi.org/10.26376/GPR2018007

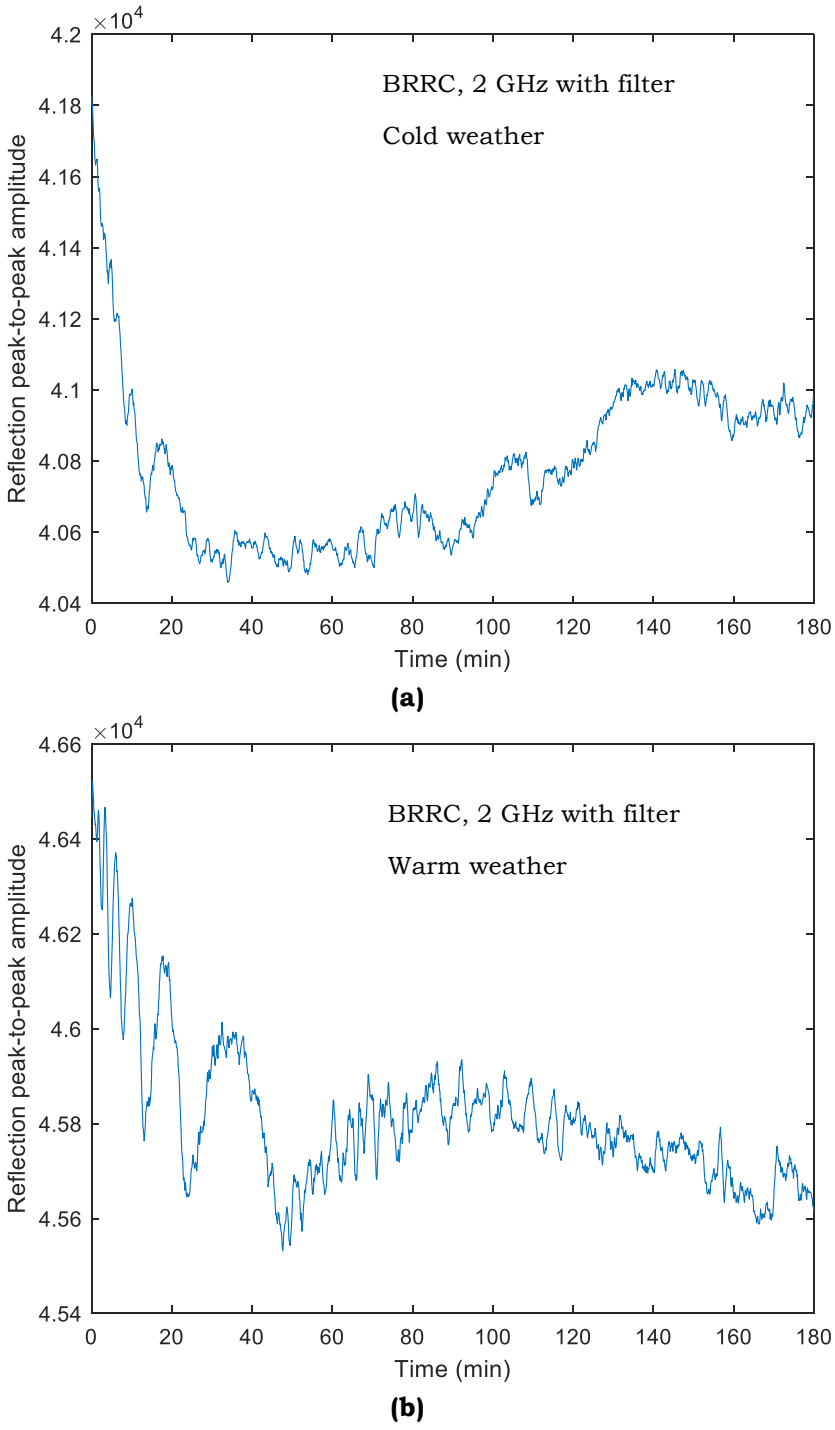

FIG. 11 – Test 4, sliding averages of the metal plate reflection peak-to-peak amplitudes (M_q) against time. **(a)** Results obtained in cold weather; **(b)** Results obtained in warm weather.

https://doi.org/10.26376/GPR2018007

can be carried out to evaluate the signal-to-noise ratio (SNR, Test 1), short-term stability (Test 2), linearity in the time axis (Test 3), and long-term stability of the GPR signal (Test 4); all tests make use of a metal plate and the GPR antenna has to be lifted over it.

Our intention was to keep the procedures simple: we are aware that more accurate tests could be conceived and proposed, however our twofold goal was to propose reliable tests and to foster greater awareness in GPR users of the importance of regularly testing control unit and antennas. Simple procedures ensure that users without a strong scientific background can correctly perform the tests, whereas sophisticated procedures would probably discourage them or be improperly applied.

The paper includes a full description of the four proposed procedures followed by results obtained by research teams from Belgium, Czech Republic, Portugal and Serbia, who performed the tests on commercial GPR systems they own and regularly use in fieldworks. Overall, five pulsed control units and nine antennas were tested (five horn and four ground-coupled antennas, with central frequencies ranging from 400 MHz to 1.8 GHz).

Only three antennas turned out to have a signal-to-noise ratio better than 20. For all antennas, the indicator of the short-term signal stability was higher than 2.8%. Regarding the linearity in the time axis, the relative variation in the measured speed was always higher than 2.9%; in this test, it is crucial to accurately measure the distance between antenna and metal plate and to position the antenna aperture or plane parallel to the ground. The long-term stability factor was always lower than 3%.

The obtained results seem to be fairly consistent: antennas performing well in one test, usually yield good results also in the other tests. The results suggest a malfunctioning of one of the antennas, which performed worse than the other antennas in three tests over four; the low performances of this antennas might be also due to a poor laboratory accuracy in performing the tests and to the metal plate used, which was smaller than suggested.

Based on our tests, a warm-up time of at least 30 min is advised before starting a survey. Our results also suggest that the behaviour of GPR systems may be strongly dependent on atmospheric conditions

https://doi.org/10.26376/GPR2018007

(different results were obtained in cold and warm weather), however more experiments are necessary to confirm this observation and better understand the relation between weather and GPR long-term stability.

While the results presented herein are not representative enough to establish absolute thresholds for the tests, they provide a valuable indication about values that one can obtain when testing GPR equipment. At present, we may say that a SNR indicator of at least 10 (20 dB) should be probably obtained when performing Test 1, if the antenna is working well. Reasonably good values of the signal stability indicator (Test 2) should not be larger than 8%. Concerning the linearity in the time axis, the indicator of Test 3 should not be larger than 6.5%. Finally, the long-term signal stability indicator of Test 4 should not be larger than 2.5%. Though reliable thresholds are not yet established, by periodically repeating the tests on the same equipment it is possible to detect shifts from previously obtained values, which may imply that the GPR under test is not working in normal or satisfactory manner. Moreover, the execution of the tests gives stronger awareness about the behaviour and limits of the owned GPR systems.

We hope that other research teams, GPR experts and manufacturers will execute the tests in the near future, on a wider variety of control units and antennas, on both brand new and older equipment, and share the results with the GPR community. In this way, reliable thresholds for the tests can be jointly established and maybe the procedures can be refined and upgraded. It will also be very interesting to investigate how the results of the proposed tests translate into accuracy levels of measured physical and geometrical quantities, in the various applications of the GPR technique. This will allow determining application-specific thresholds, instead of absolute thresholds, as well as thresholds associated with desired accuracy levels of the results.

ACKNOWLEDGEMENTS

This work was carried out as a contribution to COST (European Cooperation in Science and Technology) Action TU1208 “Civil Engineering Application of Ground Penetrating Radar” (www.cost.eu, www.gpradar.eu). The authors thank COST for funding and supporting COST Action TU1208.

https://doi.org/10.26376/GPR2018007

REFERENCES

[1] P. Annan, “GPR—History, Trends, and Future Developments,” Subsurface Sensing Technologies and Applications, vol. 3, no. 4, pp. 253–270, October 2002, doi: 10.1023/A:1020657129590.

[2] S. S. Artagan and V. Borecky, “History of using GPR for diagnostics of transport structures,” Proceedings of the 6th International Scientific Conference, Pardubice, Czech Republic, 3–4 September 2015, 7 pp.

[3] W. Wai-Lok Lai, X. Dérobert, and P. Annan, “A review of Ground Penetrating Radar application in civil engineering: A 30-year journey from Locating and Testing to Imaging and Diagnosis,” NDT & E International, vol. 96, pp. 58–78, June 2018, doi: 10.1016/j.ndteint.2017.04.002.

[4] D. J. Daniels and E. C. Utsi, “GPR case histories and known physical principles,” Proceedings of the 7th International Workshop on Advanced Ground Penetrating Radar (IWAGPR 2013), Nantes, France, 2–5 July 2013, pp. 1–9, doi: 10.1109/IWAGPR.2013.6601507.

[5] E. C. Utsi, “Ground Penetrating Radar: Theory and Practice.” Publishing House: Butterworth-Heinemann; Oxford, United Kingdom, April 2017; ISBN: 978008102216; 224 pp.

[6] A. Benedetto and L. Pajewski, Eds. “Civil Engineering Applications of Ground Penetrating Radar,” Publishing House: Springer International; Book Series "Springer Transactions in Civil and Environmental Engineering;" April 2015; e-book ISBN: 9783319048130; hardcover ISBN: 9783319048123; doi: 10.1007/9783319048130; 371 pp.

[7] X. Núñez-Nieto, M. Solla, P. Gómez-Pérez, and H. Lorenzo “GPR signal characterization for automated landmine and UXO detection based on machine learning techniques,” Remote Sensing, vol. 6, no. 10, pp. 9729–9748, October 2014, doi:10.3390/rs6109729.

[8] V. Ferrara, “Technical survey about available technologies for detecting buried people under rubble or avalanches,” WIT Transaction on The Built Environment, vol. 150, pp. 91-101, May 2015, doi: 10.2495/DMAN150091.

[9] M. Zajc, B. Celarc, and A. Gosar, “Structural–geological and karst feature investigations of the limestone–flysch thrust-fault contact using low-frequency ground penetrating radar (Adria–Dinarides thrust zone, SW Slovenia),” Environmental Earth Sciences, vol. 73, no. 12, pp. 8237-8249, June 2015, doi: 10.1007/s12665-014-3987-x.

[10] J. Jezova, L. Mertens, and S. Lambot, “Ground-penetrating radar for observing tree trunks and other cylindrical objects,” Construction and

https://doi.org/10.26376/GPR2018007

Building Materials, vol. 123, pp. 214-225, October 2016, doi: 10.1016/j.conbuildmat.2016.07.005.

[11] L. Pajewski, M. Solla, and M. Kuc̦uk̈demirci, “Ground-Penetrating Radar for Archaeology and Cultural Heritage Diagnostics: Activities Carried Out in COST Action TU1208,” in: Nondestructive Techniques for the Assessment of Historic Structures, L. M. da Silva Goncalves, H. Rodrigues, F. Gaspar, Eds., CRC Press – Taylor & Francis Group, Boca Raton, FL, USA, October 2017, ISBN 9781138710474, pp. 215-225.

[12] J. D. Taylor, Ed., “Advanced Ultrawideband Radar: Signals, Targets, and Applications,” Publishing House: CRC Press – Taylor & Francis Group; Boca Raton, FL, December 2016; ISBN 9781466586574, 494 pp.

[13] A. Zhao, Y. Jiang, and W. Wang, “Signal-to-noise ratio enhancement in multichannel GPR data via the Karhunen-Loève transform,” Proceedings of the Progress in Electromagnetic Research Symposium, Hangzhou, China, 22–26 August 2005, vol. 1, no. 6, pp. 754–757, 2005, doi: 10.2529/PIERS041210090705.

[14] X. L. Travassos, D. A. G. Vieira, V. Palade, and A. Nicolas, “Noise reduction in a non-homogenous ground penetrating radar problem by multiobjective neural networks,” IEEE Transactions on Magnetics, vol. 45, no. 3, pp. 1454–1457, February 2009, doi: 10.1109/TMAG.2009.2012677.

[15] J. Li, C. Le Bastard, Y. Wang, G. Wei, B. Ma, and M. Sun, “Enhanced GPR signal for layered media time-delay estimation in low-SNR scenario,” IEEE Geoscience Remote Sensing Letters, vol. 13, no. 3, pp. 299–303, January 2016, doi: 10.1109/LGRS.2015.2502662.

[16] L. Pajewski and M. Marciniak, “Comparative study of GPR international standards and guidelines,” Short-Term Scientific Missions - Year 2, L. Pajewski & M. Marciniak, Eds.; Publishing House: Aracne; Rome, Italy, May 2015; ISBN 978-88-548-8488-5. Available in open access on the website of COST Action TU1208: www.gpradar.eu/resources/books.html

[17] ASTM D6087-08(2015)e1 “Standard Test Method for Evaluating Asphalt-Covered Concrete Bridge Decks Using Ground Penetrating Radar,” ASTM International, West Conshohocken, PA, 2015.

[18] M. R. Mahmoudzadeh Ardekani and S. Lambot, “Full-Wave Calibration of Time- and Frequency-Domain Ground-Penetrating Radar in Far-Field Conditions,” IEEE Transactions on Geoscience and Remote Sensing, vol. 52, no. 1, pp. 664–678, January 2014, doi: 10.1109/TGRS.2013.2243458.

[19] L. Mertens, A. P. Tran, and S. Lambot, “Determination of the stability of a pulse GPR system and quantification of the drift effect on soil material characterization by full-wave inversion,” Proceedings of the 15th International

https://doi.org/10.26376/GPR2018007

Conference on Ground Penetrating Radar (GPR 2014), 30 June – 4 July 2014, Brussels, Belgium, pp. 480–483, doi: 10.1109/ICGPR.2014.6970471.

[20] A. Van der Wielen, "Characterization of thin layers into concrete with Ground Penetrating Radar," PhD Thesis; Université de Liège, Liège, Belgium, 28 March 2014; 228 pp. (available for free download at http://hdl.handle.net/2268/163976, last checked 10 July 2018).

[21] F. I. Rial, H. Lorenzo, A. Novo, and M. Pereira, "Checking the signal stability in GPR systems and antennas," IEEE Journal of Selected Topics in Applied Earth Observations and Remote Sensing, vol. 4(4), pp. 785–790, December 2011, doi: 10.1109/JSTARS.2011.2159779.

[22] T. Scullion, C. L. Lau, and T. Saarenketo, "Performance specifications of ground penetrating radar," Proceedings of the 6th International Conference on Ground Penetrating Radar (GPR 1996), 30 September–3 October 1996, Sendai, Japan, pp. 341–346.

[23] T. Scullion, C. L. Lau, and Y. Chen, "Implementation of the Texas Ground Penetrating Radar system," Interim Report No. FHWA/TX-92/1233-1, Texas Department of Transportation, November 1992 (revised April 1994), 102 pp.

[24] R. W. Jacob, J. F. Hernance, "Precision GPR measurements: Assessing and compensating for instrument drift," in Proceedings of the 10th International Conference on Ground Penetrating Radar (GPR 2004), 21–24 June 2004, Delft, The Netherlands, pp. 159–162.

[25] G. Manacorda and M. Miniati, "An easy way of checking impulsive georadar equipment performances," Proceedings of the 8th International Conference on Ground Penetrating Radar (GPR 2000), 23-26 May 2000, Gold Coast, Australia, 2000, pp. 44–49.

[26] F. Benedetto and F. Tosti, "A signal processing methodology for assessing the performance of ASTM standard test methods for GPR systems," Signal Processing, vol. 132, pp. 327–337, 2017, doi: 10.1016/j.sigpro. 2016.06.030.

[27] S. Sebesta, T. Scullion, and T. Saarenketo, "Using Infrared and High-Speed Ground-Penetrating Radar for Uniformity Measurements on New HMA Layers," Report No. S2-R06C-RR-1 of the Second Strategic Highway Research Program, Transportation Research Board of the National Academies, 2013, 81 pp.

[28] D. Goulias and M. Scott, "Effective Implementation of Ground Penetrating Radar (GPR) for Condition Assessment & Monitoring of Critical Infrastructure Components of Bridges and Highways," Final Report No. MD-

https://doi.org/10.26376/GPR2018007

15-SHA-UM-3-11, State Highway Administration of Maryland Department of Transportation, January 2015, 173 pp.

[29] R. W. Jacob and J. F. Hermance, "Assessing the precision of GPR velocity and vertical two-way travel time estimates," Journal of Environmental Engineering and Geophysics, vol. 9, no. 3, pp. 143–153, September 2004, doi: 10.4133/JEEG9.3.143.

[30] R. W. Jacob and J. F. Hermance, "Random and non-random uncertainties in precision GPR measurements: Identifying and compensating for instrument drift," Subsurface Sensing Technologies and Applications, vol. 6, no. 1, pp. 59–71, January 2005, doi: 10.1007/s11220-005-4226-z.

[31] H. Liu, B. Xing, J. Zhu, B. Zhou, F. Wang, X. Xie, and Q. H. Liu, Fellow, "Quantitative Stability Analysis of Ground Penetrating Radar Systems," IEEE Geoscience and Remote Sensing Letters, vol. 15, no. 4, April 2018, pp. 522–526, doi: 10.1109/LGRS.2018.2801827.

[32] Webpage of the Final Conference of COST Action TU1208 "Civil engineering applications of Ground Penetrating Radar" (Warsaw, Poland, 25–27 September 2017): www.gpradar.eu/events-dissemination/conferences/finalconference.html

[33] M. Vrtunski, L. Pajewski, X. Derobert, Ž. Bugarinović, A. Ristić, M. Govedarica, "GPR antenna testing based on COST Action TU1208 guidelines," Geophysical Research Abstracts, European Geosciences Union (EGU) General Assembly 2017, 8–13 April 2018, Vienna, Austria, article ID EGU2018-2353, p. 1.

[34] R. Persico, A. Provenzano, C. Trela, M. Sato, K. Takahashi, S. Arcone, S. Koppenjan, L. G. Stolarczyk, E. C. Utsi, S. Ebihara, K. Wada, E. Pettinelli, L. Pajewski, "Recommendations for the Safety of People and Instruments in Ground-Penetrating Radar and Near-surface Geophysical Prospecting." Publishing House: EAGE Publications bv; Houten, The Netherlands, June 2015, ISBN 9789462821620, 68 pp.

[35] A. Balanis, "Antenna Theory: Analysis and Design," IV edition. Publishing House: John Wiley & sons Inc; Hoboken, NJ, January 2016, ISBN: 9781118642061, 1072 pp.

[36] ASTM D4748–10(2015) "Standard Test Method for Determining the Thickness of Bound Pavement Layers Using Short-Pulse Radar," ASTM International, West Conshohocken, PA, 2015.

https://doi.org/10.26376/GPR2018007

Ground Penetrating Radar
The first peer-reviewed scientific journal dedicated to GPR

FREQUENCY DOMAIN DETERMINISTIC-STOCHASTIC ANALYSIS OF THE TRANSIENT CURRENT INDUCED ALONG A GROUND PENETRATING RADAR DIPOLE ANTENNA OVER A LOSSY HALF-SPACE

ANNA ŠUŠNJARA[1] (CORRESPONDING AUTHOR), DRAGAN POLJAK[1], VICKO DORIĆ[1], SÉBASTIEN LALLÉCHÈRE[2], KHALIL EL KHAMLICHI DRISSI[2], PIERRE BONNET[2] & FRANÇOISE PALADIAN[2]

[1] DEPARTMENT OF ELECTRONICS AND COMPUTER SCIENCE, FACULTY OF ELECTRICAL ENGINEERING, MECHANICAL ENGINEERING AND NAVAL ARCHITECTURE (FESB), UNIVERSITY OF SPLIT, SPLIT, CROATIA
ANSUSNJA@FESB.HR, DPOLJAK@FESB.HR, VDORIC@FESB.HR

[2] UNIVERSITÉ CLERMONT AUVERGNE, CENTRE NATIONAL DE LA RECHERCHE SCIENTIFIQUE (CNRS), SIGMA CLERMONT, INSTITUT PASCAL, CLERMONT-FERRAND, FRANCE
SEBASTIEN.LALLECHERE@UCA.FR, KHALIL.DRISSI@UCA.FR, PIERRE.BONNET@ UCA.FR, FRANCOISE.PALADIAN@UCA.FR

ABSTRACT

This paper deals with the stochastic analysis of transient current induced along a ground penetrating radar (GPR) antenna. The antenna is modelled as a horizontal dipole and is placed over a lossy half-space. The electromagnetic formulation of the problem is based on the Pocklington's integro-differential equation in the frequency domain, which is solved by means of the Galerkin-Bubnov indirect boundary element method. The transient solution is obtained by using the inverse fast Fourier transform. The paper aims to investigate the variability of the current due to key uncertain parameters, such as the soil permittivity and conductivity, and the wire distance from the half-space. Stochastic assumptions are incorporated in the model by means of the stochastic collocation technique. Computational examples present the mean value of current distributed along the wire with the confidence margins. Sensitivity analysis is obtained, i.e., the uncertainty in the output is apportioned to different sources of uncertainty in the model input thus giving a better insight into model reliability.

KEYWORDS: Ground Penetrating Radar (GPR); Electromagnetic modelling; Galerkin-Bubnov indirect boundary element method; Stochastic collocation technique; Antennas; Lossy half-space.

1. INTRODUCTION

Ground penetrating radar (GPR) is used in civil engineering, archaeology, and many other areas. GPR antennas are moved over the

https://doi.org/10.26376/GPR2018008

surface of the inspected soil or structure, while emitting and receiving electromagnetic (EM) waves. In order to extract accurate and useful information from the received EM field, it is important to have as much a priori information as possible [1]. Such information includes a good understanding of the electromagnetic properties of the involved media and used antennas [2]. However, the knowledge about these properties is inevitably stochastic in its nature.

Many researchers have studied the EM behaviour of GPR antennas, by using different techniques that can be classified in two main categories: frequency domain (FD) [3] and time domain (TD) [4]-[10] techniques. A stochastic analysis of the transient response of a GPR antenna has been presented in [11]-[13]. In [11] the unknown current along the wire above the lossy-half space is governed by the space-time Hallen integral equation. The deterministic solution is featured by GB-IBEM method. The stochastic response is obtained with respect to uncertain antenna position (height) and uncertain ground conductivity. The work done in [12] and [13] present the stochastic current response for the wire buried in the lossy ground which may be found useful not only in GPR purposes but in other areas, for example in the design of lighting protection for electrical settlements.

As a counterpoise to time domain analysis, the stochastic analysis of frequency domain response is presented in the present paper. Stochastic Collocation (SC) method is combined with a direct EM solver to assess the variability of the current induced on a GPR dipole antenna, due to the uncertain nature of the soil and antenna height. The dipole is assumed to be thin and is placed above a lossy half-space, with its axis parallel to the air-soil interface: such simple geometry is especially convenient for testing new computational approaches and methods. The formulation of the problem, implemented in our deterministic EM solver, is based on a FD solution of Pocklington's integro-differential equation, by means of Galerkin-Bubnov Indirect Boundary Element Method (GB-IBEM) [3]; the transient response is then obtained via inverse Fast Fourier's transform [14].

The paper is organized as follows. Section 2 outlines the employed FD integral equation approach and related numerical solution (Sub-section 2.1); the theoretical basis of the Stochastic Collocation method are also presented (Sub-section 2.2). Section 3 brings computational examples, while in Section 4 general conclusions are given.

https://doi.org/10.26376/GPR2018008

2. ELECTROMAGNETIC MODELLING METHOD

2.1 Deterministic frequency-domain analysis

The geometry of interest is a straight, thin and horizontal dipole placed at height h above a lossy half-space (see Figure 1). The wire is considered as a perfect conductor, with a voltage source applied to the gap in the centre of the antenna. The source has a Gaussian shaped waveform.

The current induced along the wire is governed by the Pocklington's integro-differential equation in the frequency domain [3]. Such equation is derived by enforcing the interface conditions for the tangential components of the electric field at the wire surface:

$$\vec{e}_x \cdot \left(\vec{E}^{exc} + \vec{E}^{sct}\right) = 0 \tag{1}$$

where $\vec{e}_x$ is the unit vector, the excitation field $\vec{E}^{exc}$ is composed by the incident field $\vec{E}^{inc}$ and the field reflected from the ground $\vec{E}^{ref}$:

$$\vec{E}^{exc} = \vec{E}^{inc} + \vec{E}^{ref} \tag{2}$$

The scattered electric field is given as:

$$\vec{E}^{sct} = -j\omega\vec{A} - \nabla\varphi \tag{3}$$

where $\vec{A}$ represents the magnetic vector potential, φ is the electric scalar potential and ω is angular frequency, $\omega=2\pi f$. According to the thin wire approximation, only the axial component of the magnetic vector potential exists, therefore Equation (3) becomes [3]:

$$E_x^{sct} = -j\omega A_x - \frac{\partial\varphi}{\partial x} \tag{4}$$

The axial component of the magnetic vector potential and the electric scalar potential are given by:

$$A_x = \frac{\mu}{4\pi}\int_{-L/2}^{L/2} I(x')g(x,x')dx' \tag{5}$$

and

$$\varphi(x) = -\frac{1}{j4\pi\omega\varepsilon_0}\int_{-L/2}^{L/2} \frac{\partial I(x')}{\partial x'}g(x,x')dx' \tag{6}$$

https://doi.org/10.26376/GPR2018008

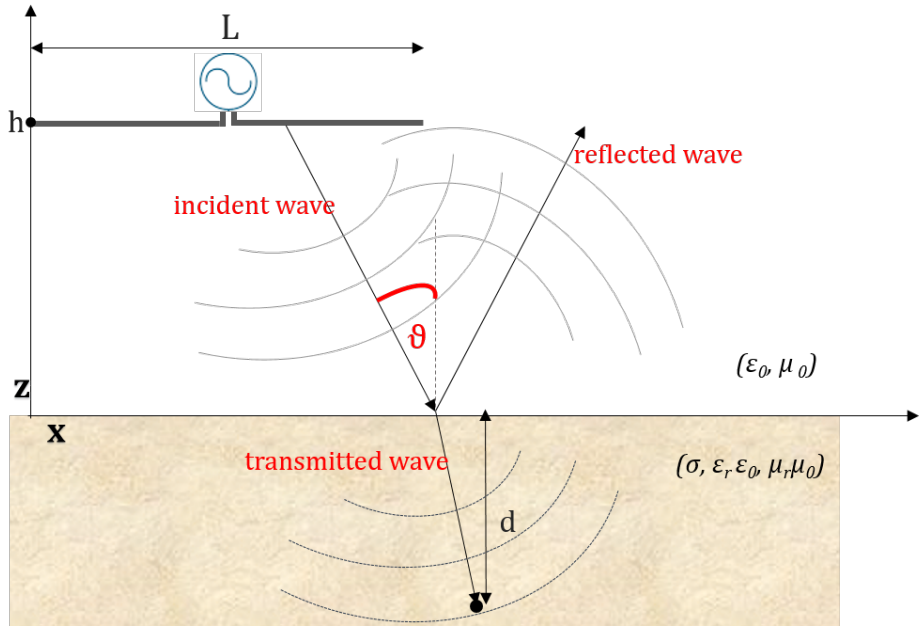

FIG. 1 – A GPR dipole antenna horizontally placed above a lossy half-space.

respectively. The induced current along the wire is represented by $I(x')$, while $g(x,x')$ denotes the total Green function [3]:

$$g(x,x') = g_0(x,x') - R_{TM} g_i(x,x') \tag{7}$$

where $g_0(x,x')$ is the free space Green function:

$$g_0(x,x') = \frac{e^{-jk_0R_0}}{R_0} \tag{8}$$

and $g_i(x,x')$ arises from the image theory:

$$g_i(x,x') = \frac{e^{-jk_0R_i}}{R_i} \tag{9}$$

The distance from the source point on the wire, or its image in the ground, to the observation point is denoted by R_0 and R_i, respectively. The influence of the lossy half-space is taken into account by means of the reflection coefficient R_{TM}, which for a transverse magnetic polarisation is given by:

$$R_{TM} = \frac{n\ \cos\vartheta - \sqrt{n - (\sin\vartheta)^2}}{n\ \cos\vartheta + \sqrt{n - (\sin\vartheta)^2}} \tag{10}$$

https://doi.org/10.26376/GPR2018008

where n stands for the refraction index and θ is the incident angle:

$$n = \sqrt{\varepsilon_r - j\sigma/(\omega\varepsilon_0)} \qquad \theta = \arctan\left[|x - x'|/(2h)\right] \tag{11}$$

Inserting Equations (4)-(7) in (2) leads to Pocklington's integro-differential equation for the unknown current induced along the wire axis [3]:

$$E_x^{exc} = \frac{j\omega\mu}{4\pi}\int_{-L/2}^{L/2} I(x')g(x,x')dx' + -\frac{1}{j4\pi\omega\varepsilon_0}\frac{\partial}{\partial x}\int_{-L/2}^{L/2}\frac{\partial I(x')}{\partial x'}g(x,x')dx' \tag{12}$$

The unknown current is calculated via GB-IBEM. More details can be found elsewhere, e.g. in [3]. In order to obtain the transient response, the solution is then transformed to the TD. First, the current is calculated for the specified frequency range, thus obtaining the transfer function of a system $H(f)$ in the FD. Then, $H(f)$ is multiplied by the spectrum of the Gaussian pulse given by [11]:

$$V(f) = V_0\sqrt{\pi}\,t_w\,e^{-(\pi f t_w)^2}\,e^{-j2\pi f t_0} \tag{13}$$

where V_0 is the amplitude, t_0 is the time delay of the Gaussian pulse and t_w is the half-width of the Gaussian pulse in the TD. Finally, the frequency response is transformed to the TD by using the inverse fast Fourier transform. For this purpose, the Matlab function *"ifft"* is used [14], [15].

2.2 Stochastic collocation technique

Stochastic studies, in general, are carried out in two steps [16]. The first step implies the definition of random input data of the given model; input random variables (RV) are statistically described by assigning the corresponding statistical distributions. The second step is to solve a stochastic numerical or analytical model to obtain the statistical description of the output value of interest.

The SC method has been widely used in recent stochastic EM computations: the main advantages are its non-intrusive nature and simplicity. A theoretical background of this approach can be found in [17], for the sake of completeness some basics are given in this section.

The fundamental principle of the SC method is the polynomial approximation of the considered output Y for N uncertain input

https://doi.org/10.26376/GPR2018008

parameters (N is defined as random dimension of the problem). The random input parameter Z is given as [17]:

$$Z = Z^0 + \hat{u} \tag{14}$$

where Z^0 is the initial value and $\hat{u}$ is a random variable with a statistical distribution. The output of interest Y is expanded over a stochastic space by using the Lagrangian basis functions:

$$Y(Z^0; t) = \sum_{\mathrm{i}=1}^{N_{SC}} Y_{\mathrm{i}}(Z^0) L_{\mathrm{i}}(t) \tag{15}$$

where $L_i(t)$ is the Lagrangian basis function given by:

$$L_{\mathrm{i}}(t) = \prod_{\mathrm{j}=1,\mathrm{j}\neq\mathrm{i}}^{N_{SC}} \frac{(t - t_{\mathrm{j}})}{(t_{\mathrm{j}} - t_{\mathrm{i}})} \tag{16}$$

and t_i is i-th collocation point, also called sigma point. The reasons for choosing the Lagrange polynomials as basis function come from its property $L_i(t_j) = \delta_{ij}$ leading to: $Y_i(Z^0) = Y(Z^0; t_i)$ [17]. Following the definition for the statistical moments, the expected value of the output Y of interest can be calculated as:

$$\langle Y(Z^0; t) \rangle = \sum_{\mathrm{i}=1}^{N_{SC}} Y_{\mathrm{i}}(Z^0)\, \mathrm{w}_{\mathrm{i}} \tag{17}$$

and the variance is:

$$\mathrm{Var}[Y(Z^0; t)] = \sigma_{\mathrm{E}}^2 = \sum_{\mathrm{i}=0}^{N_{SC}} \mathrm{w}_{\mathrm{i}} Y_{\mathrm{i}}^2 - \langle Y \rangle^2 \tag{18}$$

where w_i denotes the weight given by:

$$\mathrm{w}_{\mathrm{i}} = \int_{\mathrm{D}} L_{\mathrm{i}}(t)\, \mathrm{pdf}(t) \mathrm{d}t \tag{19}$$

for the input RV with the probability density function pdf(t). The order of the approximation depends on number of sigma points, N_{SC}. A higher N_{SC} implies a better approximation, but at the cost of computational effort. The dimensionality of the problem can be increased to the desired extent. In this paper higher dimensions are included via the tensor product rule. Therefore the number of required deterministic

https://doi.org/10.26376/GPR2018008

simulations is given as $(N_{SC})^N$. However, the SC technique suffers from the "curse of dimensionality;" hence, the computation for a very high number of input RVs by using the tensor product is not practical.

The SC method provides means for performing a Sensitivity Analysis (SA) of a given model. In this paper, the variance based sensitivity analysis is used [17]. This approach is part of a more general Global Sensitivity Analysis (GSA) method [18], which provides the means for estimating the influence of a collection of random inputs on the output of interest. In this paper, for a random dimension $N = 3$, the impact factor of each random input variable is obtained as:

$$\mathrm{I_i} = \mathrm{Var}(E;\ \mathrm{RV_i})/\mathrm{Var}(E) \tag{20}$$

where i = 1, 2, 3. This expression corresponds to the first order Sobol like indices [18]. The impact of the collection of input RVs is given as:

$$\mathrm{I'_{jk}} = \mathrm{Var}\big(E;\ \mathrm{RV_j}, \mathrm{RV_k}\big)/\mathrm{Var}(E) \tag{21}$$

where j =1, 2, 3 and k = 1, 2, 3, j≠k. The measure of mutual interaction of each combination of random input variables is defined through higher order indices. For example, second order indices are obtained by combining Equations (21) and (22). More details are found in [18].

3. COMPUTATIONAL EXAMPLES

A horizontal dipole antenna, with length $L = 1$ m and radius $a = 6.74$ mm, is placed above a lossy half-space. Both L and a are considered as deterministic parameters. Three parameters are modelled as random input variables, with uniform distributions: the antenna height (i.e., its distance from the air-soil interface) $h \sim \cup(12, 18)$ cm, the soil relative permittivity $\varepsilon_r \sim \cup(14, 18)$, and the soil conductivity $\sigma \sim \cup(0.1, 9.9)$ mS/m. The considered type of soil is an average one and the ranges of expected permittivity and conductivity values are taken from [1]. The output of interest is the transient current in the centre of the wire. The frequency range for the transfer function $H(f)$ is 10 Hz – 28.64 GHz. For the Gaussian pulse of Equation (13): $V_0 = 1\,V$, $t_0 = 1.43$ ns, and $t_w = 2/3$ ns.

In order to investigate to which extent the three random input variables impact the output of interest, all possible combinations of input RVs are taken into account, starting from three univariate cases

https://doi.org/10.26376/GPR2018008

where $N = 1$, then considering all bivariate cases with $N = 2$, and finally studying the multivariate case with random dimension $N = 3$. The variance-based approach is used to obtain the Sensitivity Analysis (SA) of the presented stochastic model. The experimental design (ED) is built for 3 and 5 SC points, thus implying $3^3 + 5^3 = 152$ different deterministic simulations. The complete stochastic analysis is done as a post processing of results obtained for the defined ED, by using equations similar to (17) and (18). The execution time of a single deterministic simulation is 17.78 minutes on ASUS PC with i5-5200 CPU and 2.20 GHz processor, which is impractical for traditional Monte Carlo simulations. In order to ensure good convergence with Monte Carlo approach, at least 10,000 – 100,000 simulations are necessary. On the other hand, according to the literature, the SC method with far less simulations is proven to have good convergence, especially for small number of input RVs, which is the case in this computational setup [11], [12], [16], [17].

Figure 2(a) exhibits the mean trend of the transient current at the centre of the wire, when all three input variables are random (N=3). The results are presented for SC simulations with 3 and 5 sigma points. The crude estimate of confidence intervals is given as the mean ± 3 standard deviations. It is apparent that throughout the whole time interval the standard deviation of the current is not large. The confidence interval is almost negligible for the early time response: in the beginning of the simulation only the peaks exhibit a noticeable deviation from the mean trend. In the later time instances the deviation around the mean trend becomes larger and more or less uniform.

Figure 2(b) shows the subsequent time interval, from 15 ns to about 30 ns, for the same case study; from this plot, the convergence and accuracy of the stochastic approach can be appreciated. The results for 3 and 5 sigma points show a satisfactory agreement. This proves that, in order to access second order statistics (mean and standard deviation) for the current in the middle of the wire with three random input variables (ε_r, σ, and h) only 3 sigma points are required, i.e., 27 deterministic simulations. In the case of univariate scenario, when only σ is random, 5 sigma points were necessary; however, as it is going to be demonstrated later, the influence of this variable on the current is very small.

https://doi.org/10.26376/GPR2018008

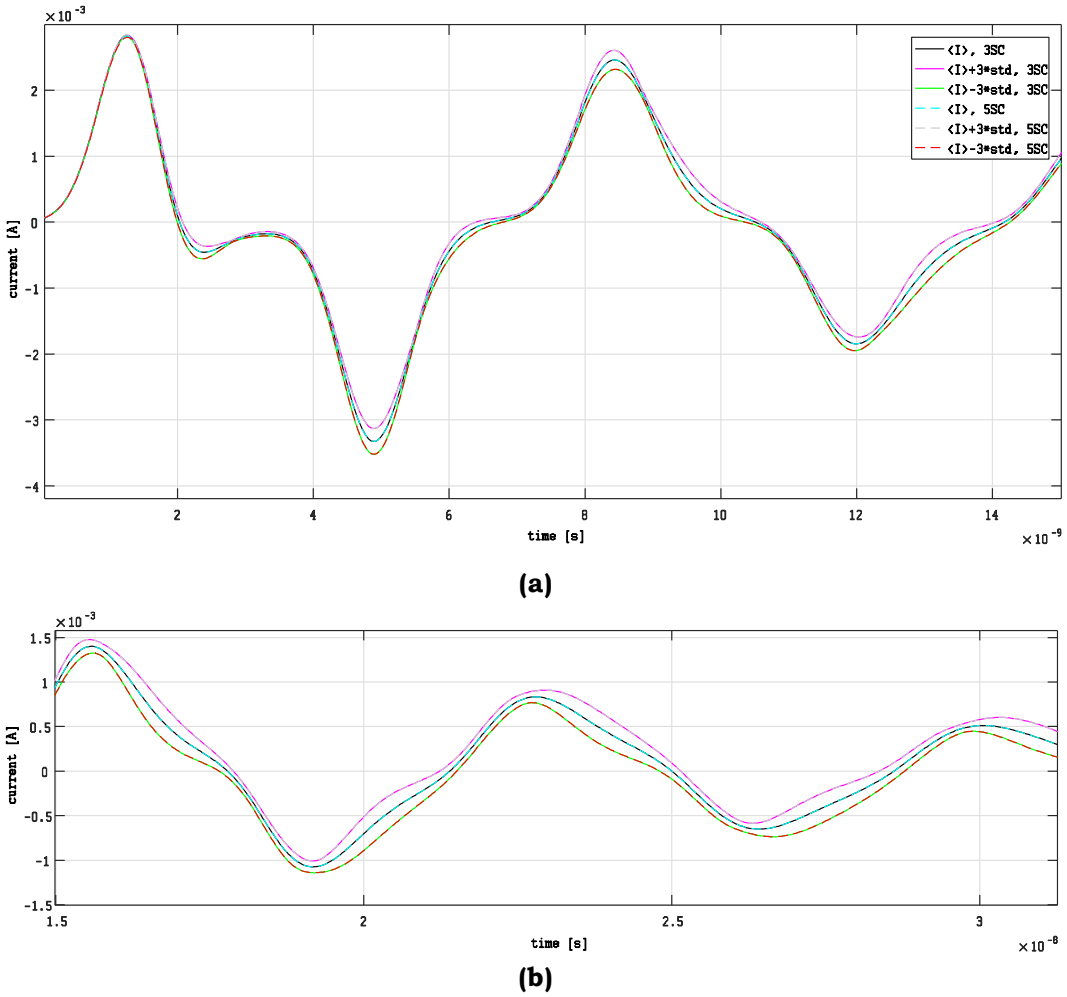

FIG. 2 – Statistics of the current at the centre of wire, for the multivariate test case: ⟨I⟩ is the stochastic expected value and std is the standard deviation: **(a)** Focus on interval 0-1.5 s **(b)** Focus on the time interval 15-30 ns.

The impact factors of each random input, calculated by using Equation (20), are shown in Figure 3. Throughout the whole simulation interval the height of the antenna has the highest impact. The influence of the first random variable, ε_r, cannot be ignored in the time instants where the current reaches its local minimum and maximum values. The overall influence of soil conductivity is small.

The impact factor of the combinations of input variables obtained from Equation (21) is depicted in Figure 4. The domination of the antenna height is obvious. The interactions of RVs have negligible impact on the total variation of the current.

https://doi.org/10.26376/GPR2018008

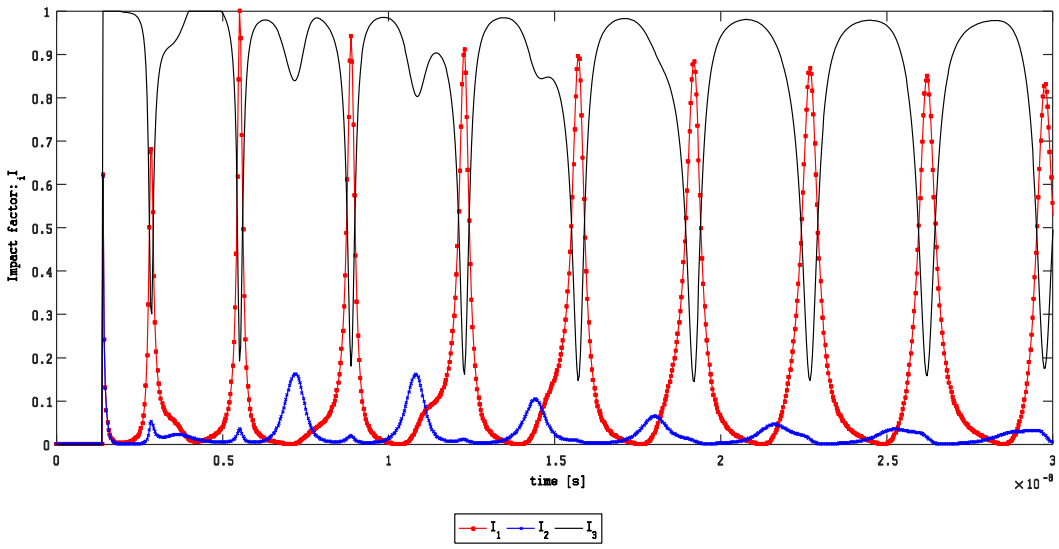

FIG. 3 – Impact factors of each input RV: $RV_1 = \varepsilon_{r,}$, $RV_2 = \sigma$, $RV_3 = h$.

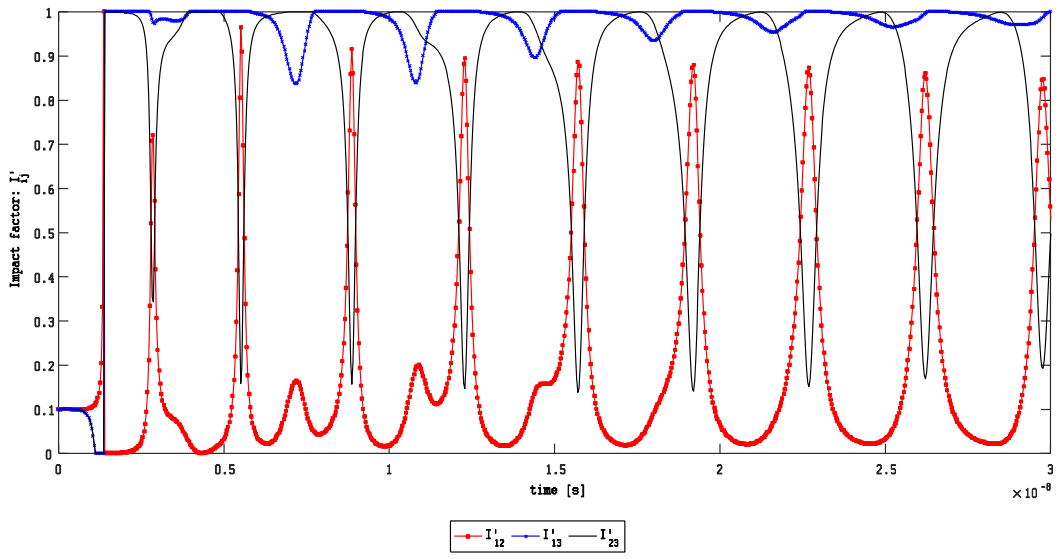

FIG. 4 – Impact factor of combinations of input random variables: $RV_{12} = [\varepsilon_r, \sigma]$, $RV_{13} = [\varepsilon_r, h]$, $RV_{23} = [\sigma, h]$.

4. CONCLUSIONS

This contribution presents a frequency domain stochastic-deterministic analysis of the current induced on a GPR dipole antenna placed above a lossy half-space. The current is governed by Pocklington's integro-

https://doi.org/10.26376/GPR2018008

differential equation in frequency domain, which is solved by means of Galerkin-Bubnov Indirect Boundary Element Method. The transient response is obtained by using inverse fast Fourier transform. The deterministic model is combined with Stochastic Collocation (SC) method in order to investigate to which extent random input parameters influence the induced current. Three input parameters are assumed to be uncertain: the permittivity and electrical conductivity of soil, and the wire distance from the soil, all following the prescribed uniform distributions. SC method showed a quick convergence in the calculation of stochastic moments, especially for the mean value. The obtained numerical results demonstrate that the variation of the wire height has the highest overall impact on the current distribution, for the considered average soil type.

The calculation of the current induced along the wire is the first step in analysing the electromagnetic behaviour of a GPR antenna and thus its scattered field. The stochastic approach in electromagnetic modelling is a natural and useful extension, arising from the inherent uncertainty of the parameters that belong to such environment. SC, in combination with existing deterministic models, is a powerful tool for the calculation of necessary statistics of the outputs of interest and allows a better understanding of the electromagnetic behaviour of a GPR system.

Acknowledgements

This work benefited from networking activities carried out within EU funded COST Action TU1208 “Civil Engineering Application of Ground Penetrating Radar” (www.gpradar.eu).

References

[1] H. M. Jol, Ground Penetrating Radar Theory and Applications, Amsterdam: Elsevier Science, 2009.

[2] C. Warren, N. Chiwaridzo, A. Giannopoulos, “Radiation Characteristics of a High-Frequency Antenna in Different Dielectric Environments,” Proc. 15th International Conference on Ground Penetrating Radar – GPR 2014, 30 June - 4 July 2014, Brussels, Belgium, pp. 767–772, doi: 10.1109/ICGPR.2014. 6970529.

[3] D. Poljak and V. Doric, “Transmitted field in the lossy ground from ground penetrating radar (GPR) dipole antenna,” Computational Methods and

https://doi.org/10.26376/GPR2018008

Experimental Measurements XVII 3, vol. 59, WIT Press, pp. 3-11, 2015, doi: 10.2495/CMEM150011.

[4] A. Giannopoulos, "Modelling ground penetrating radar by gprmax," Construction and Building Materials, vol. 19, no. 10, pp. 755-762, December 2005, doi: 10.1016/j.conbuildmat.2005.06.007.

[5] L. Gurel and U. Oguz, "Three-dimensional fdtd modelling of a ground penetrating radar," IEEE Transactions on Geoscience and Remote sensing, vol. 38, no. 4, pp. 1513–1521, 2000, doi: 10.1109/APS.2000.874882.

[6] T. Weiland, "A discretization model for the solution of Maxwell's equations for six-component fields," Archiv fuer Elektronik und Uebertragungstechnik, vol. 31, p. 116–120, 1977.

[7] D. Poljak, S. Sesnic, D. Paric, and K. El Khamlichi Drissi, "Direct Time Domain Modeling of the Transient Field Transmitted in a Dielectric Half-Space for GPR Applications," Proceedings of the International Conference on Electromagnetics in Advanced Applications (ICEAA), 7–11 September 2015, Torino, Italy, pp. 345–348, doi: 10.1109/ICEAA.2015.7297133.

[8] D. Poljak, S. Sesnic, A. Susnjara, D. Paric, K. El Khamlichi Drissi, S. Lallechere, "Direct time domain evaluation of the transient field transmitted into a lossy ground due to GPR antenna radiation," Engineering Analysis with Boundary Elements, vol. 82, pp. 27–31, 2017, doi: 10.1016/ j.enganabound. 2017.05.007

[9] C. Warren, L. Pajewski, D. Poljak, A. Ventura, A. Giannopoulos, and S. Sesnic, "A comparison of Finite-Difference, Finite-Integration, and Integral-Equation methods in the Time Domain for modelling Ground Penetrating Radar antennas," Proceedings of the 16th International Conference of Ground Penetrating Radar, 13–16 June 2016, Hong Kong, China, doi: 10.1109/ICGPR.2016. 7572676.

[10] C. Warren, S. Sesnic, A. Ventura, L. Pajewski, D. Poljak, and A. Giannopoulos, "Comparison of Time-Domain Finite-Difference, Finite-Integration, and Integral-Equation Methods for Dipole Radiation in Half-Space Environments," Progress In Electromagnetics Research M, vol. 57, pp. 175–183, 2017, doi: 10.2528/PIERM17021602.

[11] S. Lalléchère, S. Antonijevic, K. El Khamlichi Drissi, and D. Poljak, "Optimized Numerical Models of Thin Wire above an Imperfect and Lossy Ground for GPR Statistics," Proc. International Conference on Electromagnetics in Advanced Applications (ICEAA), 7–11 September 2015, Torino, Italy, pp. 907–910, doi: 10.1109/ICEAA.2015.7297246.

[12] S. Lalléchère, S. Sesnic, P. Bonnet, K. El Khamlichi Drissi, F. Paladian, D. Poljak, "Sensitivity analysis of the time transient currents induced along

https://doi.org/10.26376/GPR2018008

thin wires buried in lossy and uncertain environments," Proceedings of the 11th European Conference on Antennas and Propagation (EUCAP 2017), 19–24 March 2017, Paris, France doi: 10.23919/EuCAP.2017.7928291

[13] S. Sesnic, S. Lalléchère, D. Poljak, and K. El Khamlichi Drissi, "Stochastic collocation analysis of the transient current induced along the wire buried in a lossy medium," Computational Methods and Experimental Measurements XVII, Southampton, WIT Press, pp. 47–58, 2015, doi: 10.2495/CMEM150051.

[14] A. Susnjara, D. Poljak, S. Sesnic, and V. Doric, "Time Domain and Frequency Domain Integral Equation Method for the Analysis of Ground Penetrating (GPR) Antenna," Proceedings of the 24th International Conference on Software, Telecommunications and Computer Networks (SoftCOM 2016), 22–24 September 2016, Split, Croatia, pp. 1–4, doi: 10.1109/SOFTCOM.2016.7772184.

[15] Matlab Version 7.11.0.584 (R2010b), Massachusetts: The MathWorks Inc, 2010.

[16] S. Lalléchère, P. Bonnet, and F. Paladian, "Electrical stochastic modelling of cell for bio-electromagnetic compatibility applications," Annals of Telecommunications, vol. 69, pp. 295–308, 2014, doi: 10.1007/s12243-013-0364-9.

[17] H. Dodig, S. Lalléchère, P. Bonnet, and K. El Khamlichi Drissi, "Stochastic sensitivity of the electromagnetic distributions inside a human eye modeled with 3D hybrid BEM/FEM edge element method," Engineering Analysis with Boundary Elements, vol. 49, pp. 48–62, 2014, doi: 10.1016/j.enganabound.2014.04.005.

[18] A. Saltelli, M. Ratto, T. Andres, F. Campolongo, J. Cariboni, D. Gatelli, M. Saisana, and S. Tarantola, Global Sensitivity Analysis: The Primer, Ed. Wiley, January 2008.

[19] D. Poljak, Advanced Modeling in Computational Electromagnetic Compatibility. Hoboken, NJ: Wiley, 2007.

APPENDIX

Galerkin-Bubnov indirect boundary element solution of Pocklington integral equation

An operator form of Pocklington integro-differential equation (12) can be, for convenience, symbolically written as:

$$K\,I = E \tag{A1}$$

https://doi.org/10.26376/GPR2018008

where K is a linear operator and I is the unknown function to be found for a given excitation E.

The unknown current is expanded into a finite sum of linearly independent basis functions $\{f_\mathrm{i}\}$ with unknown complex coefficients α_i:

$$I \cong I_n \sum_{i=1}^{n} \alpha_\mathrm{i} f_\mathrm{i} \tag{A2}$$

Substituting (A2) into (A1) yields:

$$K\, I \cong I_n \sum_{\mathrm{i}=1}^{n} \alpha_\mathrm{i} K f_\mathrm{i} = E_n = p_n(E) \tag{A3}$$

where $p_n(E)$ is called projection operator [19]. Now the residual R_n is formed as follows:

$$R_n = K\, I_n - E = p_n(E) - E \tag{A4}$$

In accordance to the definition of the scalar product of functions in Hilbert function space, the error R_n is weighted to zero with respect to certain weighting functions $\{W_\mathrm{j}\}$, i.e.:

$$< R_n, W_\mathrm{j} > = 0; \quad \mathrm{j} = 1, 2, \ldots n \tag{A5}$$

where the expression in brackets stands for a scalar product of functions given by:

$$< R_n, W_\mathrm{j} > = \int_\Omega R_n W_\mathrm{j}^* d\Omega \tag{A6}$$

where Ω denotes the actual calculation domain. As the operator K is linear, a system of linear equations is obtained by choosing $W_\mathrm{j} = f_\mathrm{j}$, which implies the Galerkin-Bubnov procedure. Thus, the following equation can be written:

$$\sum_{\mathrm{i}=1}^{n} < K f_\mathrm{i}, f_\mathrm{j} > = < E, f_\mathrm{j} > \quad \mathrm{j} = 1, 2, \ldots, n \tag{A7}$$

Equation (A7) is the strong Galerkin-Bubnov formulation of Pocklington integral equation (12). By using the integral equation kernel symmetry, by taking into account Dirichlet boundary conditions for the current at the free ends of the dipole, and after integration by parts, Equation (A7) becomes:

https://doi.org/10.26376/GPR2018008

$$\sum_{\mathrm{i}=1}^{n} \alpha_{\mathrm{i}} \frac{1}{j4\pi\varepsilon} \left\{ \int_0^L \frac{df_{\mathrm{j}}(x)}{dx} \int_0^L \frac{df_{\mathrm{j}}(x)}{dx} g(x,x')dxdx' + k^2 \int_0^L f_{\mathrm{j}}(x) \int_0^L f_{\mathrm{i}}(x) g(x,x')dxdx' + \int_0^L f_{\mathrm{j}}(x) Z_S(x)dx \right\} = \int_0^L E_x^{exc}(x) f_{\mathrm{j}}(x)dx, \quad \mathrm{j} = 1,2,\dots n \tag{A8}$$

For the case of lossless conductors, Z_S=0. Equation (A8) represents the weak Galerkin-Bubnov formulation of the integral equation of (12). The resulting system of algebraic equations arising from the boundary element discretization of (A8) is given by [19]:

$$\sum_{\mathrm{j}=1}^{M} [Z]_{\mathrm{ji}} \{I\}_{\mathrm{i}} = \{V\}_{\mathrm{j}}, \qquad \mathrm{j} = 1,2,\dots M \tag{A9}$$

where $[Z]_{\mathrm{ji}}$ is the local matrix representing the interaction of the i-th source boundary element with the j-th observation boundary element:

$$[Z]_{\mathrm{ji}} = \frac{-1}{4j\pi\omega\varepsilon} \left(\int_{\Delta l_{\mathrm{j}}} \{D\}_{\mathrm{j}} \int_{\Delta l_{\mathrm{i}}} \{D'\}_{\mathrm{i}}^T g(x,x')dx\,dx' + k^2 \int_{\Delta l_{\mathrm{j}}} \{f\}_{\mathrm{j}} \int_{\Delta l_{\mathrm{i}}} \{f\}_{\mathrm{i}}^T g(x,x')\,dxdx' \right) + \int_{\Delta l_{\mathrm{j}}} Z_L(x) \{f\}_{\mathrm{j}} \{f\}_{\mathrm{i}}^T dx \tag{A10}$$

The vector $\{I\}$ contains the unknown coefficients of the solution and represents the local voltage vector. The matrices $\{f\}$ and $\{f'\}$ contain the shape functions, $\{D\}$ and $\{D'\}$ contain their derivatives, M is the total number of line segments, and Δl_{i}, Δl_{j} are the widths of the i-th, j-th segments.

https://doi.org/10.26376/GPR2018008

Ground Penetrating Radar
The first peer-reviewed scientific journal dedicated to GPR

ELECTROMAGNETIC MODELLING AND SIMULATION OF A HIGH-FREQUENCY GROUND-PENETRATING RADAR ANTENNA OVER A CONCRETE CELL WITH STEEL RODS

ALESSIO VENTURA (CORRESPONDING AUTHOR) & LARA PAJEWSKI

DEPARTMENT OF INFORMATION ENGINEERING, ELECTRONICS AND TELECOMMUNICATIONS,
SAPIENZA UNIVERSITY OF ROME, ROME, ITALY
ALESSIOVENTURA@HOTMAIL.COM, LARA.PAJEWSKI@UNIROMA1.IT

ABSTRACT

This work focuses on the electromagnetic modelling and simulation of a high-frequency Ground-Penetrating Radar (GPR) antenna over a concrete cell with reinforcing elements. The development of realistic electromagnetic models of GPR antennas is crucial for accurately predicting GPR responses and for designing new antennas. We used commercial software implementing the Finite-Integration technique (CST Microwave Studio) to create a model that is representative of a 1.5 GHz Geophysical Survey Systems, Inc. antenna, by exploiting information published in the literature (namely, in the PhD Thesis of Dr Craig Warren); our CST model was validated, in a previous work, by comparisons with Finite-Difference Time-Domain results and with experimental data, with very good agreement, showing that the software we used is suitable for the simulation of antennas in the presence of targets in the near field. In the current paper, we firstly describe in detail how the CST model of the antenna was implemented; subsequently, we present new results calculated with the antenna over a reinforced-concrete cell. Such cell is one of the reference scenarios included in the Open Database of Radargrams of COST Action TU1208 "Civil engineering applications of Ground Penetrating Radar" and hosts five circular-section steel rods, having different diameters, embedded at different depths into the concrete. Comparisons with a simpler model, where the physical structure of the antenna is not taken into account, are carried out; the significant differences between the results of the realistic model and the results of the simplified model confirm the importance of including accurate models of the actual antennas in GPR simulations; they also emphasize how salient it is to remove antenna effects as a pre-processing step of experimental GPR data. The simulation results of the antenna over the concrete cell presented in this paper are attached to the paper as 'Supplementary materials.'

KEYWORDS: Ground Penetrating Radar (GPR); Electromagnetic modelling; Finite-Integration technique (FIT); Antennas; TU1208 Open Database of Radargrams; concrete.

https://doi.org/10.26376/GPR2018009

1. INTRODUCTION

Electromagnetic simulations of Ground Penetrating Radar (GPR) [1] scenarios including realistic models of the antennas are not yet common. Accurate models of GPR antennas have been only occasionally developed during the past two decades [2]-[9]; rarely, they have been combined with realistic models of complex environments [10]. In most cases, GPR electromagnetic simulations use hertzian dipoles or lines of current to represent the transmitting antennas; the physical structure of the receiving antennas is usually not included in the models and the electric field impinging on the receivers is calculated [11]-[16]. This simplified approach is customarily adopted because easier to implement and computationally cheaper; in fact, nowadays running realistic models of GPR scenarios is still a challenging task, notwithstanding computing power is increasing and becoming more accessible.

In this paper, we employed commercial software implementing the Finite-Integration technique (FIT) [17] (CST Microwave Studio) for modelling and simulating an antenna representative of a widely used high-frequency commercial device manufactured by Geophysical Survey Systems, Inc. (GSSI). All necessary information about the antenna was taken from Dr Craig Warren's PhD Thesis [6], where the freeware tool GprMax3D [18] was used to develop a Finite-Difference Time-Domain (FDTD) model of the same antenna. It has to be noted that, in [6] and here, the numerical model does not exactly replicate the commercial antenna because the electromagnetic properties of some antenna materials are unknown, due to commercial sensitivity; the undisclosed values were estimated in [6] (the match between the real and synthetic crosstalk responses of the antenna in free-space was maximized, by using Taguchi's optimisation method). It is also worth mentioning that the FDTD model developed in [6] is currently included in the library of antennas of the open-source software gprMax [19, 20], therefore gprMax users can easily include this antenna into their simulations without having to build it step-by-step. The CST model that we developed was successfully validated via comparisons with synthetic and experimental data available in [6], in cooperation with colleagues from The University of Edinburgh (United Kingdom); such data were obtained with the antenna immersed in free space and in lossy dielectric environments, with and without a circular-section metallic target and some results of the performed comparisons were presented in a conference paper [21].

https://doi.org/10.26376/GPR2018009

In Section 2 of the present paper, we describe in detail how we developed the CST Microwave Studio model of the antenna; this information was not included in [21]. Then, in Section 3, we present new results that we obtained by simulating the antenna over a reinforced-concrete cell. Such cell is one of the reference scenarios included in the Open Database of Radargrams of COST Action TU1208 [22] and hosts a series of five circular-section steel rods, having different diameters and/or embedded at different depths into the concrete [23]. We compare results obtained by using the realistic CST antenna model, and results obtained by representing the transmitting antenna with a line of current and by neglecting the physical structure of the receiving antenna. The aim of this comparison is to confirm and further highlight the importance of including realistic models of the actual antennas in GPR simulations, whenever the objective of the simulations is to accurately replicate a real GPR response, or to exploit the simulation results into an inversion process. Moreover, the comparisons presented in this paper emphasize once more how strong are antenna effects, and therefore, how salient it is to develop methods for removing them as a pre-processing step of GPR data. The results of our simulations are attached to the paper as 'Supplementary materials.'

3. Building the CST Microwave Studio model of the antenna

We used CST Microwave Studio to simulate an antenna representative of the 1.5 GHz (Model 5100) device manufactured by GSSI, which is a high-frequency high-resolution antenna using bowties as transmitting and receiving elements. As already mentioned in the Introduction, all information about the electromagnetic and geometrical properties of the antenna was taken from Dr Craig Warren's PhD Thesis [6].

The bowtie is a compact, light and cheap to produce broadband antenna, which is very often used in GPR systems [24]. The bowtie size and flare angle are critical to the performance of the antenna. The bowties simulated in this paper have a flare angle of 76°, with rectangular patches added to their open ends (these extensions introduce a delay in the signal path and create destructive interference patterns that reduce unwanted resonance phenomena); the triangle base and height are 22 mm and 15 mm long, respectively; the size of the additional rectangular patches is 22 mm × 14 mm (see Figure 1).

https://doi.org/10.26376/GPR2018009

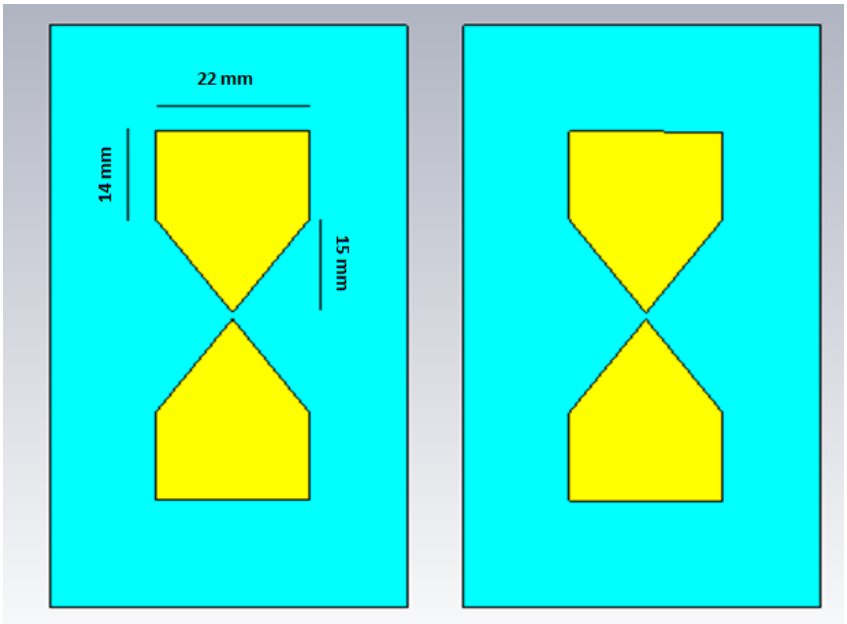

FIG. 1 – Geometrical sketch of the simulated bowties.

The simulated bowties are etched from 1-mm thick copper onto Printed Circuit Boards (PCB); they are enclosed in glass fibre boxes and then in rectangular metal boxes, which act as shields (shields are important to prevent electromagnetic emissions from the antenna interfering with surrounding electronic equipment, as well as to reduce the exposure of the human operator to the electromagnetic fields). Open-cell carbon-loaded foam is used, which acts as a broadband electromagnetic absorber to reduce unwanted resonance in the cavities behind the transmitting and receiving bowties. Some components of the GSSI antenna are made from plastics: in particular, the enclosure of the overall antenna is made of polypropylene (PP) and the 2-mm thick skid plate is made of High-Density Polyethylene (HDPE) (the skid plate is a replaceable component designed to protect the base of the antenna from damage).

In CST Microwave Studio, we modelled the shields and any other metallic components as perfectly conducting (PEC), apart from the bowties. Indeed, for the copper bowties we assumed a constant relative permittivity $\varepsilon_{copper} = 1$ and a conductivity $\sigma_{copper} = 59.6\ 10^6$ S/m (same as in [6]).

https://doi.org/10.26376/GPR2018009

For the plastics, all values were taken from [6]. In particular, for the HDPE skid plates, for the PP case, and for the glass fibre of the PCB, the following constant relative permittivity values were used: $\varepsilon_{HDPE} = 2.35$, $\varepsilon_{PP} = 2.26$, and $\varepsilon_{PCB} = 3$, respectively; moreover, losses were neglected ($\sigma_{HDPE} = \sigma_{PP} = \sigma_{PBC} = 0$). The electromagnetic properties of the absorbers are unknown, for commercial reasons; the following values were estimated in [6] via comparisons between experimental and synthetic results: $\varepsilon_{abs} = 6.49$ and $\sigma_{abs} = 0.252$ S/m. We used the same values in our CST models.

In Figure 2, geometrical sketches are reported, to better clarify the geometry of the modelled device and the size of all its parts (such sketches are generated by the computer-aided drafting tool of CST); a photo of the real antenna can be found in Fig. 24 of [6].

In the real antenna, the transmitter and receiver bowties are connected to circuits that generate the input pulses and process the received signals. The physical electronic components of these circuits were not modelled in [6] and also here, for two reasons: because the circuit design and components properties are unknown; and, because to accurately model components of that size a sub-millimetre mesh should be used, which would increase the computational requirements. In CST, for the receiver circuitry of both antennas we used a lumped resistance in the gap between the receiver bowtie arms. The software offers the possibility to insert simple electronic components in the model, called 'Lumped Network Elements' (LEMs). Three different circuits can be used: RLC-Serial, RLC-Parallel and Diode: see Figure 3(a)-(c). Obviously, it is possible to model sub-circuits of these RLC circuits by setting one or more components to 0 (this removes the respective components from the circuit). In [6], resistance components were modelled by specifying the corresponding conductivity of a single-cell edge. Although we adopted in our models the same value as in [6] for the resistance at the receiver, i.e., $R_{Rx} = 925\ \Omega$, it has to be kept in mind that the resistance is modelled differently in GprMax3D and CST, which may cause small differences in the results. For what concerns the feeding, CST provides three different source elements to excite a model: 'waveguide ports', 'plane waves', and 'discrete ports' ('edge' and 'face'). We opted for a discrete face port to simulate a lumped element source. Three different discrete face ports are available in CST, where the excitation is considered as a voltage, as current source, or as an

https://doi.org/10.26376/GPR2018009

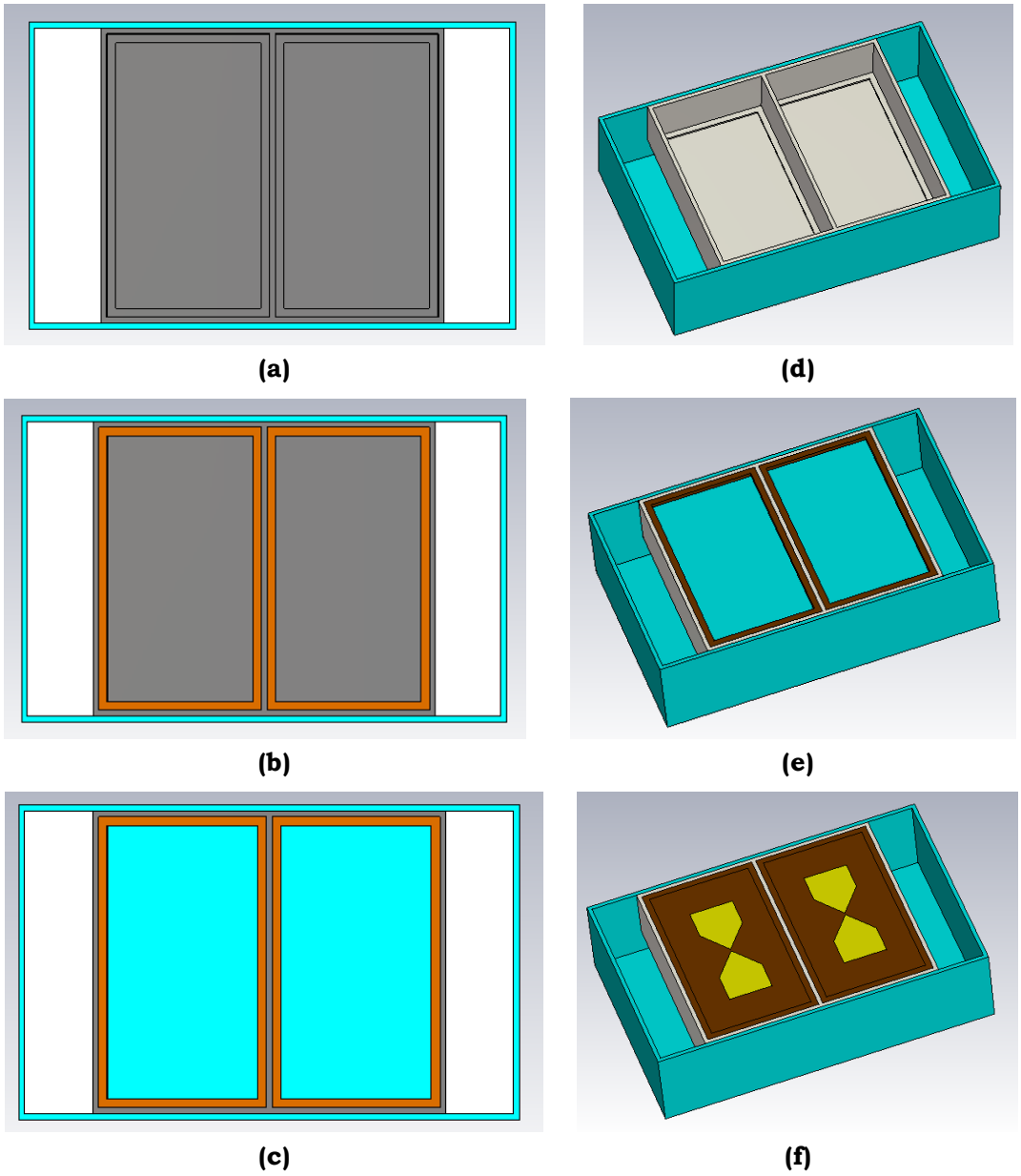

FIG. 2 – Geometrical sketches of antenna parts: **(a)** PP enclosure (170 mm × 107 mm × 43 mm; the PP thickness is 2 mm) and metal shielding structure (120 mm × 103 mm × 27 mm; PEC thickness is 2 mm); **(b)** PP enclosure, metal shielding structure and two glass fibre boxes (57 mm × 99 mm x 24 mm; the glass fibre thickness is 3 mm); **(c)** PP enclosure, metal shielding structure, glass fibre boxes and microwave absorbers (51 mm × 93 mm × 23 mm), on which the antennas sketched in Figure 1 are finally placed; **(d)** PP enclosure and metal shielding structure; **(e)** PP enclosure, metal shielding structure, glass fibre boxes and microwave absorbers; **(f)** the whole antenna structure, with bowties embedded in PCB.

https://doi.org/10.26376/GPR2018009

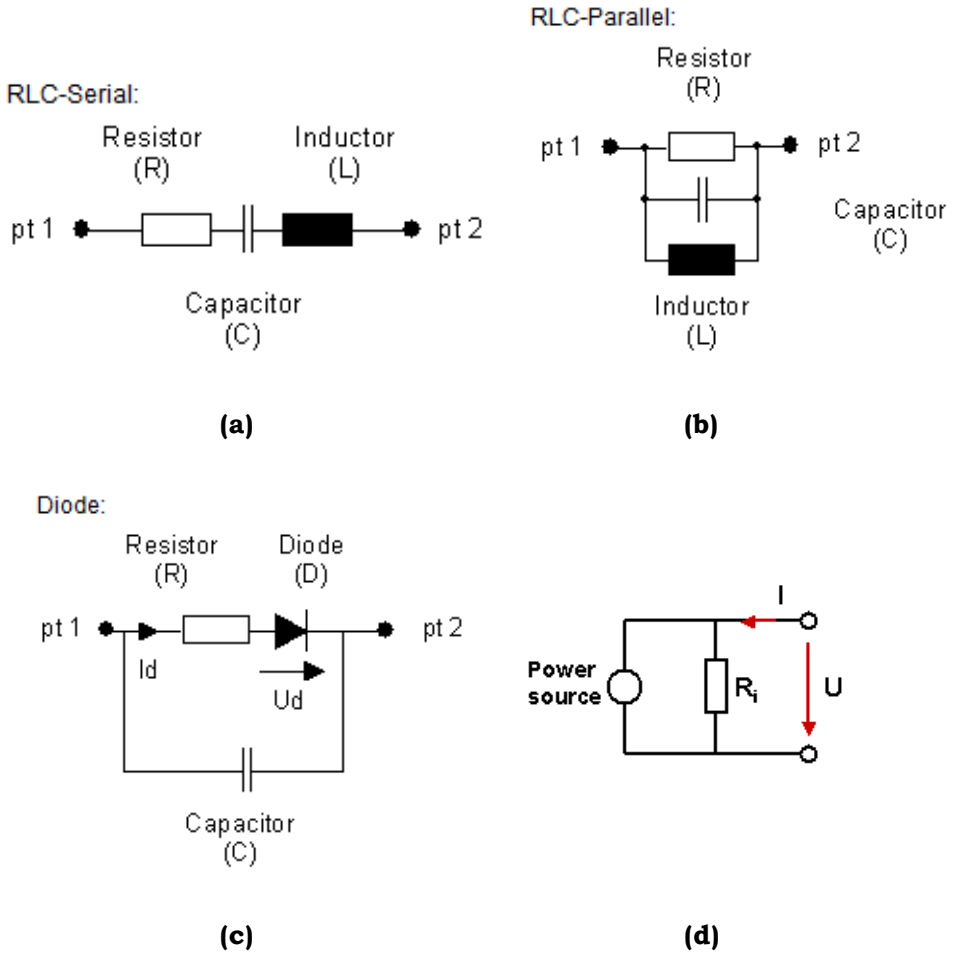

FIG. 3 – **(a)-(c)** Lumped Network Elements available in CST; **(d)**: Equivalent circuit of the CST S-parameter discrete face port.

impedance element that also absorbs some power and enables S-parameter calculation; we used the latter, which equivalent circuit is shown in Figure 3(d). The resistance at the drive point was R_{Tx} = 10 kΩ, whereas in [6] the optimized value of the drive-point resistance was 4 Ω because a different feeding model was used (with series instead of parallel resistance). We estimated the best value of our resistance in an empiric way: we performed several simulations and compared the CST crosstalk response of the antenna in a vacuum with the GprMax3D response taken from [6]; then, we adopted the resistance value that provided the best agreement.

https://doi.org/10.26376/GPR2018009

Concerning the shape and frequency content of the emitted pulse, those used by GSSI are unknown parameters; in [6], it was decided to use a Gaussian pulse because this is a common choice in GPR simulations. The expression of the Gaussian pulse of unit amplitude is:

$$V_G(t) = exp[-2\pi^2 f^2 (t - 1/f)^2] \quad (1)$$

where f is the pulse centre frequency and t is the time. The first derivative with respect to time of the Gaussian pulse is often used in GPR simulations, too:

$$V_{DG}(t) = -4\pi^2 f^2 exp[-2\pi^2 f^2 (t - 1/f)^2](t - 1/f) \quad (2)$$

A centre frequency equal to 1.71 GHz (different than the frequency stated by the manufacturer) was identified in [6] by measuring the crosstalk response of the real antenna. With this value of the centre frequency, the amplitude of the pulses (1) and (2) is plotted versus time in Figure 4(a); the spectral content of the pulses is shown in Figure 4(b). By comparing the time shape of the Gaussian pulse with the curves in Figure 3 of [21], it is already clear that the antenna structure has a strong influence on the signal recorded by a GPR. For all results presented in the following Section, the emitted pulse shape was Gaussian and the centre frequency was 1.71 GHz.

3. NUMERICAL RESULTS

The CST model that we developed was validated via comparisons with synthetic and experimental data available in [6], in cooperation with our colleagues from The University of Edinburgh; the considered data were obtained with the antenna in free space and over lossy half-spaces (emulsions), with and without a circular-section metallic target; the achieved agreement was very good and some comparisons were presented in the conference paper [21].

In this Section, we present new results obtained by simulating the antenna over a reinforced-concrete cell hosting five circular-section steel rods with different diameters and/or burial depths. This cell was first proposed in [23] and its cross-section is shown in Figure 5. In the simulations, the relative permittivity of concrete is 6 and its conductivity is 0.01 S/m; the relative permittivity of the compacted fill is 16 and its conductivity is 0.005 S/m; the circular-section cylinders

https://doi.org/10.26376/GPR2018009

embedded in concrete are assumed to be PEC. Results are calculated in five different positions, namely with the center of the overall antenna above the axes of the five targets; the bowtie axes are always parallel to the axes of the cylinders.

We also used GprMax2D to implement and execute a simplified two-dimensional model of the same scenario, where the transmitting antenna is represented by a line source, the receiving antenna is not modelled, and the electric field impinging on the receiver is calculated. As already mentioned in the Introduction, this kind of simplified simulation is most often found in the GPR scientific literature, because easier to implement and less demanding from a computational point of view than the simulation of a realistic three-dimensional model.

In Figure 6, the amplitude of the signal received by the GPR is plotted as a function of time when the antenna is positioned above the cylinder having a 2-cm diameter and buried at 6 cm from the air-concrete interface (i.e., the first cylinder starting from the left in Figure 5); CST results for the realistic model and GprMax2D results for the simplified model are shown, and both curves have been normalized to their absolute maximum value for a better readability of the comparison. In Figure 7, the same is shown when the antenna is above the cylinder having a 2-cm diameter and buried at 9 cm from the air-concrete interface (i.e., the second cylinder starting from the left in Figure 5). Analogously, in Figure 8 the same is shown when the antenna is above the cylinder having a 2-cm diameter and buried at 12 cm from the air-concrete interface (i.e., the third cylinder starting from the left in Figure 5). In Figure 9, the same is shown when the antenna is above the cylinder having a 1-cm diameter and buried at 9 cm from the air-concrete interface (i.e., the fourth cylinder starting from the left in Figure 5). And, in Figure 10 the same is shown when the antenna is above the largest cylinder having a 3 cm diameter and buried at 9 cm from the air-concrete interface (i.e., the fifth and last cylinder starting from the left in Figure 5).

To ease the Reader's comprehension and interpretation of the curves presented in Figures 6-10, in Figure 11 a synthetic B-Scan is reported, which was obtained by moving the antenna above the entire concrete cell, with a 5 mm spatial step (this B-Scan was calculated by using GprMax2D, for the simplified model).

https://doi.org/10.26376/GPR2018009

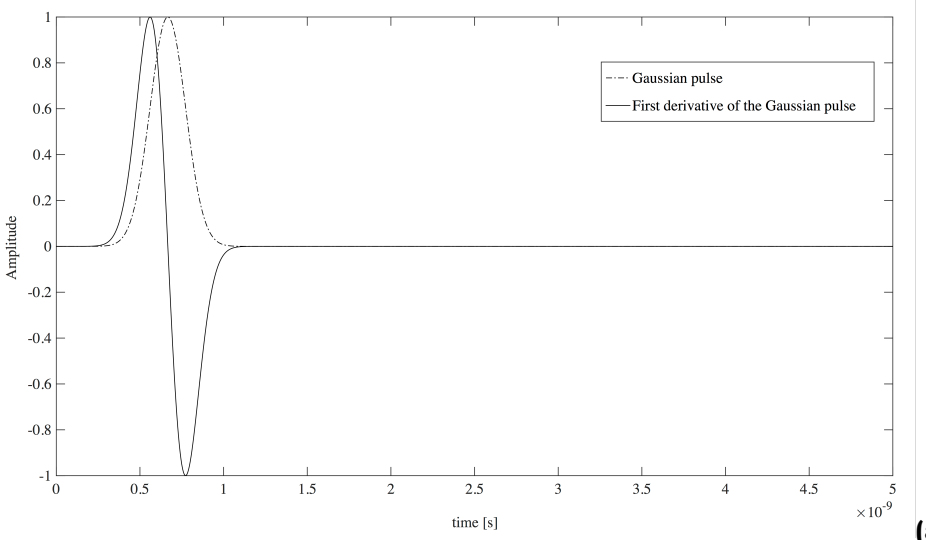

(a)

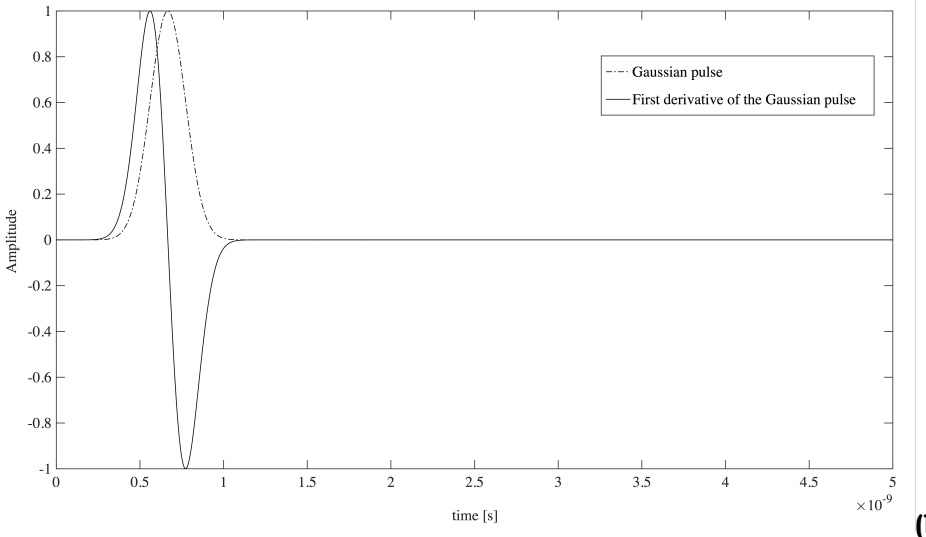

(b)

FIG. 4 – **(a)** Amplitude (a.u.) of the pulses (1) and (2) versus time; (b) single-sided spectrum of the pulses (1) and (2) (a.u.). In the simulations presented in this paper, a Gaussian pulse is used.

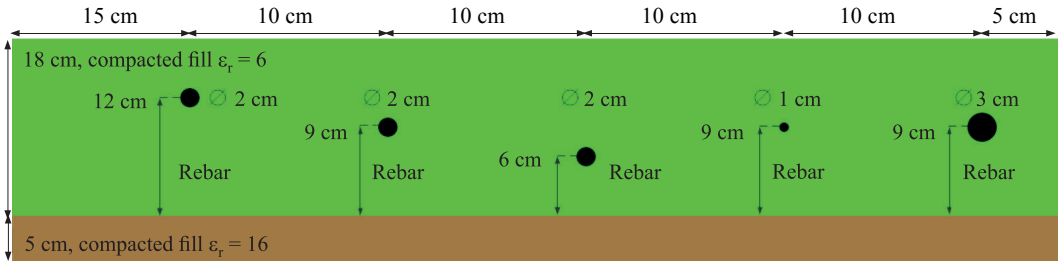

FIG. 5 – Geometry of the concrete cell proposed in [23].

https://doi.org/10.26376/GPR2018009

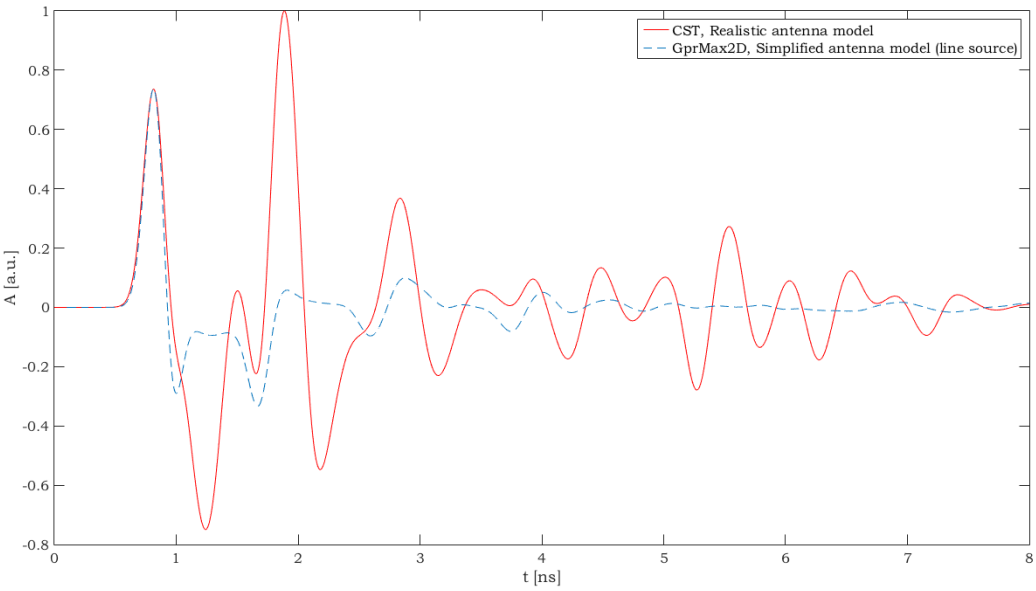

FIG. 6 – Amplitude of the signal received by the GPR, normalized to its absolute maximum value, as a function of time; the antenna is positioned above the cylinder having a 2-cm diameter and buried at 6 cm from the air-concrete interface.

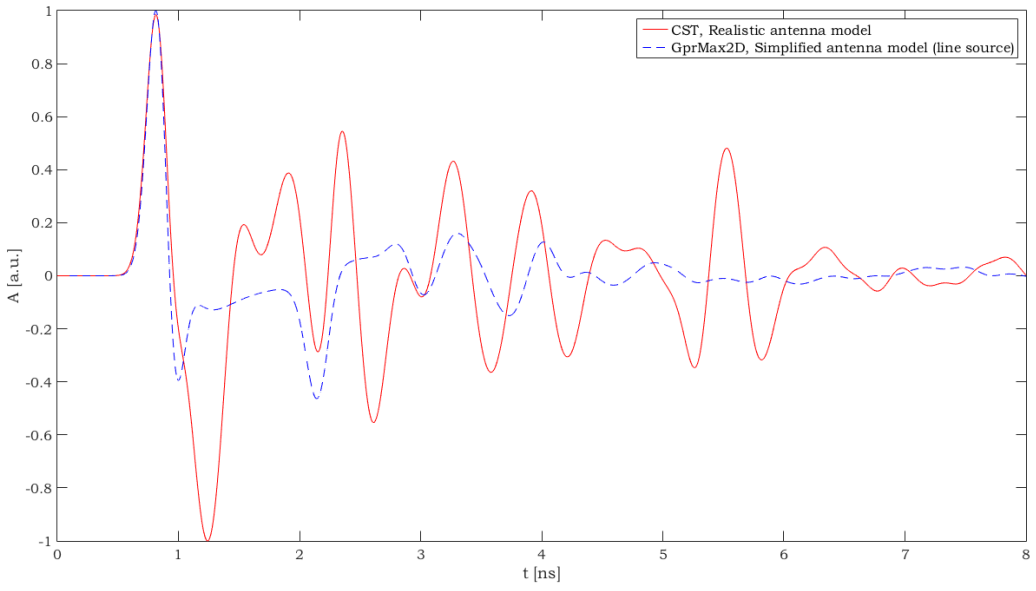

FIG. 7 – Same as in Fig. 6, when the antenna is positioned above the cylinder having a 2-cm diameter and buried at 9 cm from the air-concrete interface.

https://doi.org/10.26376/GPR2018009

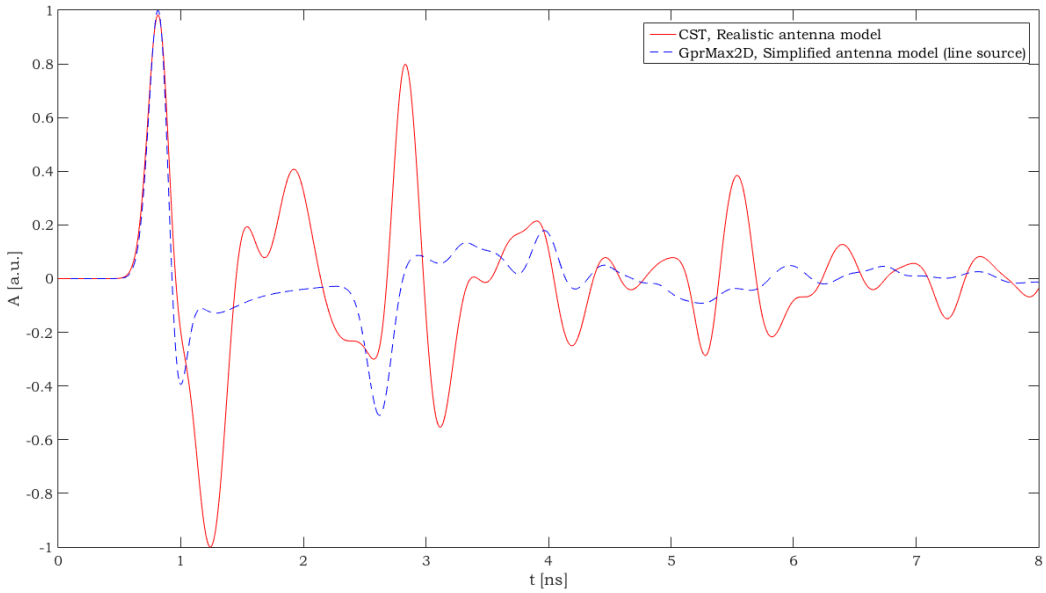

FIG. 8 – Same as in Fig. 6, when the antenna is positioned above the cylinder having a 2-cm diameter and buried at 12 cm from the air-concrete interface.

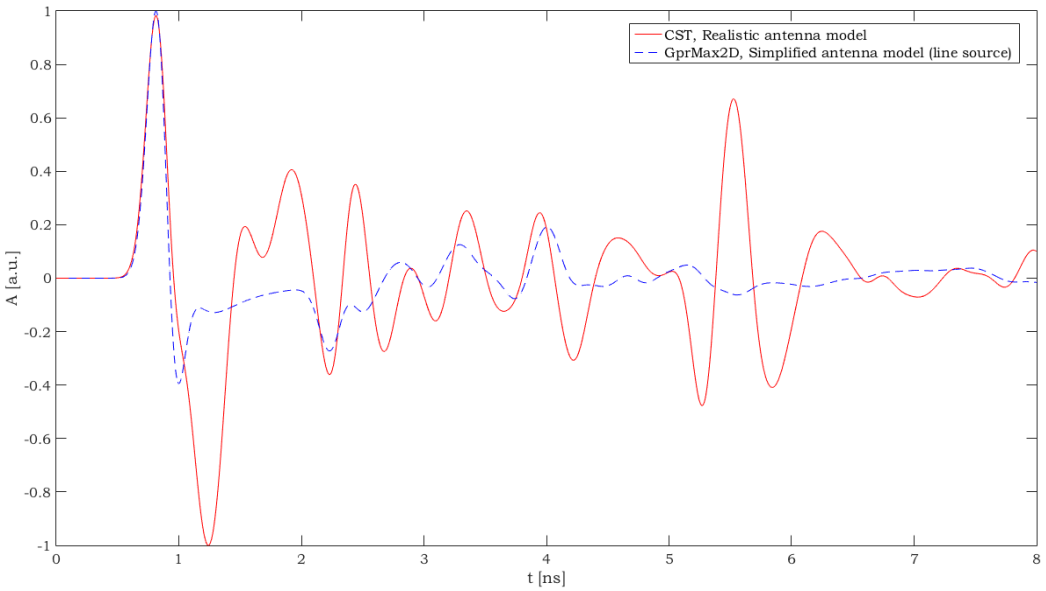

FIG. 9 – Same as in Fig. 6, when the antenna is positioned above the cylinder having a 1-cm diameter and buried at 9 cm from the air-concrete interface.

https://doi.org/10.26376/GPR2018009

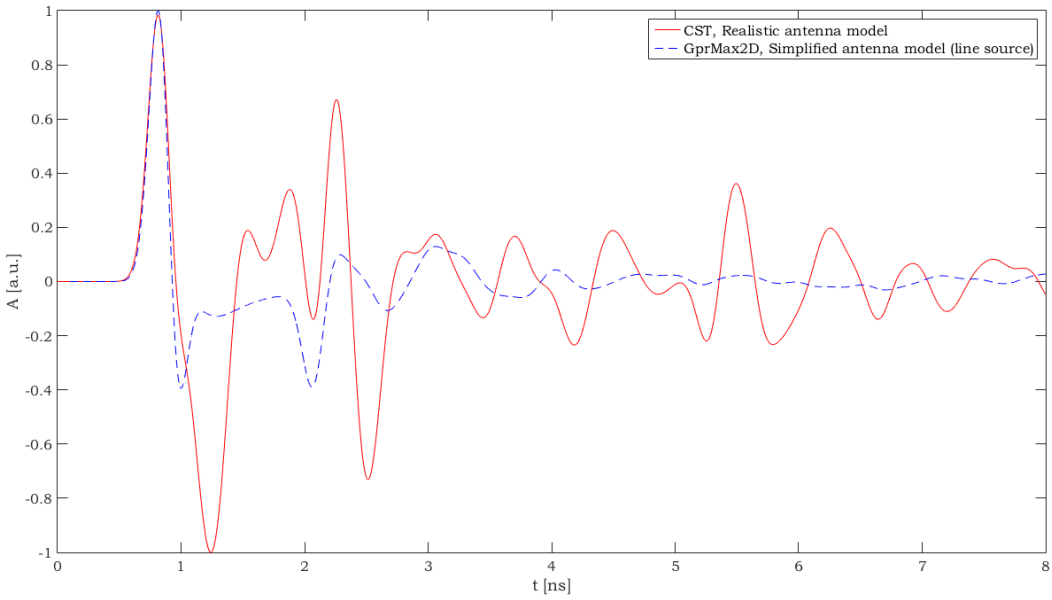

FIG. 10 – Same as in Fig. 6, when the antenna is positioned above the cylinder having a 3-cm diameter and buried at 9 cm from the air-concrete interface.

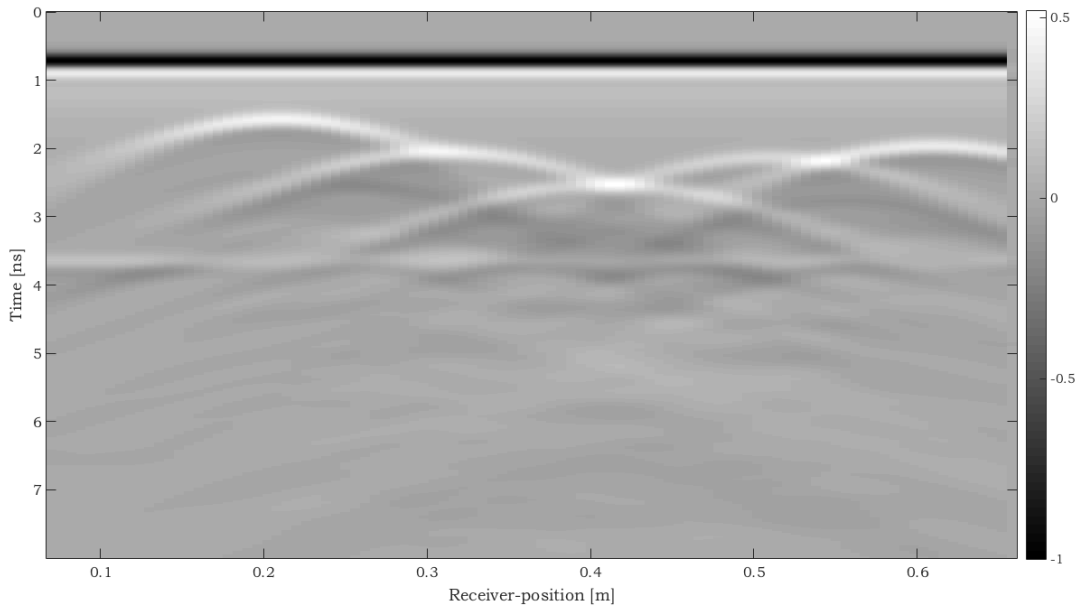

FIG. 11 – B-Scan obtained by moving the GPR antenna above the entire concrete cell, with a 5 mm spatial step (GprMax2D results for the simplified model).

https://doi.org/10.26376/GPR2018009

From Figures 6-10, it is apparent that the differences between the simulation results of the realistic model and those of the simplified model are significant. It can be noticed that, in many cases, the arrival time of echoes coming from the targets are in good agreement (the worst agreement is in Figure 8, when the antennas are in the middle of the scenario and the electromagnetic interactions between the targets are stronger). The amplitude and shape of the various echoes, instead, are highly different for the two models.

The presented comparisons confirm that for an accurate simulation of GPR scenarios (i.e., for obtaining a synthetic response close to the real one) it is crucial to develop detailled and unidealized models, not only of the environment (surveyed ground or structure and targets) but also of the antennas, which makes absolutely sense, because the antennas strongly affect the responses recorded by the radar.

Furthermore, the comparisons shown in this paper emphasize how salient it is to filter out the antenna effects as a pre-processing step of GPR data, whenever GPR data wish to be used not only for estimating the depth of interfaces and targets (from the arrival instants of the relevant echoes) but also for assessing other geometrical and physical properties, such as the size and relative permittivity of targets (by analyzing the amplitude and shape of the various echoes) [25], [26]. Prominent efforts are being done in this sense; a Belgian research team recently developed a novel approach for the removal of antenna effects [27], [28], which allows filtering out the antenna multiple internal reflections, the antenna-medium ringing, and the antenna height variation effects from GPR data acquired in near-field conditions above a locally multilayered medium.

4. Conclusions

Realistic models of Ground-Penetrating Radar (GPR) antennas in complex environments are not common in the scientific literature. In this paper, a full-wave electromagnetic model of a high-frequency GPR antenna over a concrete cell with reinforcing elements was implemented by using the commercial software CST Microwave Studio, which makes use of the Finite-Integration technique. The simulated antenna is representative of a 1.5 GHz device manufactured by Geophysical Survey

https://doi.org/10.26376/GPR2018009

Systems, Inc. All information to build the antenna model was taken from the PhD thesis of Dr Craig Warren [6], where the same device was simulated for the first time by using the well-known Finite-Difference Time-Domain software GprMax3D; our exercise was possible because [6] is very clearly written and all steps are explained in an exhaustive way. The simulated concrete cell with reinforcing elements is one of the reference scenarios included in the Open Database of Radargrams of COST Action TU1208 "Civil engineering applications of Ground Penetrating Radar" and hosts five circular-section steel rods, having different diameters, embedded at different depths into the concrete [23].

In Section 2 of this paper, the implementation of the CST Microwave Studio antenna model was described in detail.

In Section 3, new results calculated with the antenna over the above-mentioned concrete cell were presented. Comparisons with a simpler model, where the physical structure of the antenna was not taken into account, were carried out. The aim of such comparisons was to confirm and further highlight the importance of including realistic models of the actual antennas in GPR simulations, whenever the objective of the simulations is to replicate the real GPR response or to exploit the forward-scattering results into an inversion process. This is especially true when GPR is used for locating and identifying shallow targets in a heterogeneous environment (e.g., landmines in the soil) or multiple closely separated targets embedded at a limited depth in a structure (e.g., reinforcing elements, voids and cracks in concrete). For such applications, high-frequency antennas are used, to achieve sufficient resolution; the responses from the sought targets arrive at the receiving antenna very soon and are often superimposed between each other, moreover strong electromagnetic interactions between targets, as well as between antennas and targets, take place (therefore, the recorded responses strongly depend on the properties of the transmitting and receiving antennas). The comparisons presented in this paper are also a reminder of how salient it is to remove antenna effects as a pre-processing step of GPR data; additionally, they show how the simulation of simplified models can be useful to aid the interpretation of experimental responses (and of synthetic responses generated by executing more complex models).

An archive containing the results of the simulations of the antenna over the reinforced concrete cell are attached to this paper as

https://doi.org/10.26376/GPR2018009

'Supplementary materials'. Reproducing these results may be a useful exercise for a University student who wishes to learn how to use an electromagnetic simulator; actually, the work presented herein was mostly developed during the Master thesis in Electronic Engineering of the first author, under the supervision of the second author.

Acknowledgements

The work presented in this paper was carried out as a contribution to COST (European Cooperation in Science and Technology) Action TU1208 "Civil Engineering Application of Ground Penetrating Radar". The authors are grateful to COST for funding and supporting COST Action TU1208.

Supplementary materials

Data presented in Figures 7-12 can be downloaded at the following url:

http://gpradar.eu/onewebmedia/SupplementaryMaterials_GPR-1-2-3.zip

References

[1] A. Benedetto and L. Pajewski, Eds. "Civil Engineering Applications of Ground Penetrating Radar," Publishing House: Springer International; Book Series "Springer Transactions in Civil and Environmental Engineering;" April 2015; e-book ISBN: 9783319048130; hardcover ISBN: 9783319048123; doi: 10.1007/9783319048130; 371 pp.

[2] L. Gurel and U. Oguz, "Three-dimensional FDTD modeling of a Ground-Penetrating Radar," IEEE Transactions on Geoscience and Remote Sensing, vol. 38, no. 4, pp. 1513–1521, July 2000, doi: 10.1109/36.851951.

[3] S. Lambot, E. C. Slob, I. van den Bosch, B. Stockbroeckx, and M. Vanclooster, "Modeling of Ground-Penetrating Radar for accurate characterization of subsurface electric properties,'" IEEE Transactions on Geoscience and Remote Sensing, vol. 42, no. 11, pp. 2555–2568, November 2004, doi: 10.1109/TGRS.2004.834800.

[4] G. Klysz, X. Ferrieres, J. Balayssac, and S. Laurens, "Simulation of direct wave propagation by numerical FDTD for a GPR coupled antenna," NDT & E International, vol. 39, no. 4, pp. 338–347, November 2006, doi: 10.1016/ j.ndteint.2005.10.001.

https://doi.org/10.26376/GPR2018009

[5] A. Ahmed, Y. Zhang, D. Burns, D. Huston, and T. Xia, “Design of UWB Antenna for Air-Coupled Impulse Ground-Penetrating Radar,” IEEE Geoscience and Remote Sensing Letters, vol. 13, no. 1, pp. 92–96, January 2016, doi: 10.1109/LGRS.2015.2498404.

[6] C. Warren, “Numerical modelling of high-frequency ground-penetrating radar antennas,” PhD Thesis, The University of Edinburgh, 2009 (available for download at http://hdl.handle.net/1842/4074 - last checked 2 July 2018).

[7] C. Warren and A. Giannopoulos, “Creating FDTD models of commercial GPR antennas using Taguchi's optimisation method,” Geophysics, vol. 76, no. 2, pp. G37–G47, March 2011, doi: 10.1190/1.3548506.

[8] N. Diamanti and A. P. Annan, “Characterizing the energy distribution around GPR antennas,” Journal of Applied Geophysics, vol. 99, pp. 83–90, December 2013, doi: 10.1016/j.jappgeo.2013.08.001.

[9] C. Warren and A. Giannopoulos, “Experimental and Modeled Performance of a Ground Penetrating Radar Antenna in Lossy Dielectrics,” IEEE Journal of Selected Topics in Applied Earth Observations and Remote Sensing, vol. 9, no. 1, pp. 29–36, Jan. 2016, doi: 10.1109/JSTARS.2015.2430933.

[10] I. Giannakis, A. Giannopoulos, and C. Warren, “A Realistic FDTD Numerical Modeling Framework of Ground Penetrating Radar for Landmine Detection,” IEEE Journal of Selected Topics in Applied Earth Observations and Remote Sensing, vol. 9, no. 1, pp. 37–51, January 2016, doi: 10.1109/ JSTARS.2015.2468597.

[11] A. Benedetto, F. Tosti, L. Pajewski, F. D’Amico, and W. Kusayanagi, “FDTD Simulation of the GPR Signal for Effective Inspection of Pavement Damages,” Proceedings of the 15th International Conference on Ground Penetrating Radar (GPR 2014), Brussels, Belgium, 30 June – 4 July 2014, pp. 513–518, doi: 10.1109/ICGPR.2014.6970477.

[12] P. Shangguan and I. L. Al-Qadi, “Calibration of FDTD Simulation of GPR Signal for Asphalt Pavement Compaction Monitoring,” IEEE Transactions on Geoscience and Remote Sensing, vol. 53, no. 3, pp. 1538–1548, March 2015, doi: 10.1109/TGRS.2014.2344858.

[13] M. Solla, R. Asorey-Cacheda, X. Núñez-Nieto, and B. Conde-Carnero, “Evaluation of historical bridges through recreation of GPR models with the FDTD algorithm,” Construction and Building Materials, vol. 77, pp. 19–27, January 2016, doi: 10.1016/j.ndteint.2015.09.003.

[14] M. Loewer and J. Igel, “FDTD simulation of GPR with a realistic multi-pole debye description of lossy and dispersive media,” Proceedings of the 16th International Conference on Ground Penetrating Radar (GPR 2016), Hong Kong, 13– 6 June 2016, pp. 1–5, doi: 10.1109/ICGPR.2016.7572599.

https://doi.org/10.26376/GPR2018009

[15] J. Igel, S. Stadler, and T. Günther, "High-resolution investigation of the capillary transition zone and its influence on GPR signatures," Proceedings of the 16th International Conference on Ground Penetrating Radar (GPR 2016), Hong Kong, 13–16 June 2016, pp. 1–5, doi: 10.1109/ICGPR.2016.7572603.

[16] A. Benedetto, F. Tosti, L. Bianchini Ciampoli, A. Calvi, M. G. Brancadoro, and A. M. Alani, "Railway ballast condition assessment using ground-penetrating radar – An experimental, numerical simulation and modelling development," Construction and Building Materials, vol. 140, pp. 508–520, June 2017, doi: 10.1016/j.conbuildmat.2017.02.110.

[17] T. Weiland, "A discretization model for the solution of maxwell's equations for six-component fields," Archiv Elektronik und Uebertragungstechnik, vol. 31, pp. 116–120, 1977.

[18] A. Giannopoulos, "Modelling ground penetrating radar by GprMax," Construction and building materials, vol. 19, no. 10, pp. 755–762, December 2005, doi: 10.1016/j.conbuildmat.2005.06.007.

[19] C. Warren, A. Giannopoulos, and I. Giannakis, "gprMax: Open source software to simulate electromagnetic wave propagation for Ground Penetrating Radar," Computer Physics Communications, vol. 209, pp. 163–170, December 2016, doi: 10.1016/j.cpc.2016.08.020.

[20] C. Warren, A. Giannopoulos, N. Diamanti, and P. Annan, "An extension module to embed commercially sensitive antenna models in gprMax," Proceedings of the 8th International Workshop on Advanced Ground Penetrating Radar (IWAGPR 2015), 7–10 July 2015, Florence, Italy, pp. 1–3, doi: 10.1109/IWAGPR.2015.7292623.

[21] C. Warren, L. Pajewski, A. Ventura, and A. Giannopoulos, "An Evaluation of Finite-Difference and Finite-Integration Time-Domain Modelling Tools for Ground Penetrating Radar Antennas," Proceedings of the 10th European Conference on Antennas and Propagation (EuCAP 2016), 10–15 April 2016, Davos, Switzerland, pp. 1–5, doi: 10.1109/EuCAP.2016.7482010.

[22] X. Dérobert and L. Pajewski, "TU1208 Open Database of Radargrams: The Dataset of the IFSTTAR Geophysical Test Site," Remote Sensing, vol. 10, article ID 530, pp. 1–50, March 2018, doi: 10.3390/rs10040530.

[23] L. Pajewski and A. Giannopoulos, "Electromagnetic Modelling of Ground Penetrating Radar Responses to Complex Targets," Short Term Scientific Missions and Training Schools – Year 1, COST Action TU1208, L. Pajewski & M. Marciniak, Eds., Aracne Editrice, Rome, Italy, May 2014, ISBN 9788854872257, pp. 7–45 (available for download at www.GPRadar.eu).

[24] L. Pajewski, F. Tosti, and W. Kusayanagi, "Antennas for GPR Systems," Chapter 2 in A. Benedetto and L. Pajewski, Eds. "Civil Engineering

https://doi.org/10.26376/GPR2018009

Applications of Ground Penetrating Radar," Publishing House: Springer International; Book Series "Springer Transactions in Civil and Environmental Engineering;" April 2015; e-book ISBN: 9783319048130; hardcover ISBN: 9783319048123; doi: 10.1007/9783319048130; 371 pp.

[25] F. Frezza, P. Martinelli, L. Pajewski, and G. Schettini, "A CWA-Based Detection Procedure of a Perfectly-Conducting Cylinder Buried in a Dielectric Half-Space," Progress In Electromagnetics Research B, vol. 7, 265–280, 2008, doi: 10.2528/PIERB08032603.

[26] F. Frezza, P. Martinelli, L. Pajewski, and G. Schettini, "Short-Pulse Electromagnetic Scattering by Buried Perfectly Conducting Cylinders," IEEE Geoscience and Remote Sensing Letters, vol. 4, no. 4, pp. 611–615, October 2007, doi: 10.1109/LGRS.2007.903078.

[27] A. De Coster and S. Lambot, "Full-wave removal of internal antenna effects and antenna-medium coupling for improved ground-penetrating radar," IEEE Transactions on Geoscience and Remote Sensing, Submitted (TGRS-2018-00050).

[28] A. De Coster and S. Lambot, "Fusion of Multifrequency GPR Data Freed From Antenna Effects," in IEEE Journal of Selected Topics in Applied Earth Observations and Remote Sensing, vol. 11, no. 2, pp. 664-674, February 2018, doi: 10.1109/JSTARS.2018.2790419.

https://doi.org/10.26376/GPR2018009

Ground Penetrating Radar
The first peer-reviewed scientific journal dedicated to GPR

GPR RESEARCH IN WOJANÓW RAILWAY TUNNEL, SUDETES MTS., POLAND

ADAM SZYNKIEWICZ

KART-GEO, WROCLAW, POLAND, ADAM.SZYNKIEWICZ@GMAIL.COM

ABSTRACT

In the area of Wojanów railway tunnel (Sudetes Mts., Poland), Ground Penetratind Radar (GPR) was employed in the context of a geotechnical research for the purposes of designing the tunnel renovation. Various antennas were used, with 100 MHz, 250 MHz, and 800 MHz central frequencies. The sections recorded above the tunnel with 100 MHz antennas allowed estimating at what distance from the tunnel casing, behind the housing, there is a solid rock. The cross-sections recorded with 250 MHz antennas allowed figuring out the structure of the ground behind the tunnel casing. The analysis of data obtained with 800 MHz antennas made it possible to precisely determine the condition of the tunnel casing and of the casing reinforcement zone. An attempt was also made to analyse GPR data in a three-dimensional system, to study the general state of the ground behind the tunnel casing; the analysis indicated loosening rocks and empty spaces behind the tunnel casing.

KEYWORDS: Ground Penetrating Radar (GPR); Civil engineering; Railway tunnel.

1. INTRODUCTION

Ground-penetrating radar (GPR) is a safe and valuable method for the non-destructive testing of transport infrastructures, including tunnels [1], [2]. In the scientific literature, several works address the successful use of GPR for the assessment of roads and bridges, whereas a rather limited number of case studies deal with the use of this technique for the investigation of tunnels [3]–[23]. This is probably due to the fact that tunnel inspections present considerable practical difficulties, compared to roads and bridges, therefore they are less frequent. The objectives of this paper are to present the results of a GPR survey carried out in Wojanów railway tunnel, in Poland, and to provide practical guidelines for GPR inspection of tunnels.

https://doi.org/10.26376/GPR2018010

Location of Wojanów railway tunnel

Wojanów railway tunnel is located in the Sudetes Mts., in the south west of Poland, about 15 km east of Jelenia Góra.

The tunnel is carved in granite and is located at an altitude of about 376 m above sea level, about 30 m below the ridge of the tunnel mountain and about 20 m above the water level in the Bóbr river. The water level in the Bóbr river is at an average height of about 356 m above sea level.

Wojanów railway tunnel was built in 1867. The length of the tunnel is 293.15 m, the vertical height is 6.82–7.22 m, and the maximum horizontal width of the tunnel is 7.09–7.38 m. The walls of the tunnel are enclosed with granite blocks, which dimensions are: 1–0.35 m × 0.4–0.6 m. The granite housing blocks have a weight of 600–1200 kg. Eastern and Western tunnel entrances (E and W inlet to the tunnel) are enclosed with stone portals made of granite blocks.

After 150 years of operation and progressing degradation, this tunnel requires renovation and protection. In the tunnel housing there are numerous cracks and displacements of the rock blocks of the casing. In the ceiling of the tunnel there are numerous gaps between the housing blocks. Recently, wooden wedges have been torn into these gaps to prevent block housing from falling out. On the ceiling and side walls there are numerous places of slow water outflow and precipitation of calcium carbonate ($CaCO_3$ speleothems). In the eastern part of the tunnel, water flows out from the gaps between the housing blocks in the form of a stream.

Geological situation

Wojanów railway tunnel was forged in granite rocks of the Upper Carboniferous [24]–[26]. This granite is coarse-grained, cracked and cut with quartz veins and veins of aplite. There are cracks in the granite, inclined towards the south. In the south-eastern part of the tunnel mountain, there is an old mining tunnel (about 200 m long) where vertical veins of quartz and aplite, running NE–SW, have been found. In the outcrops, occurring near the western outlet of the tunnel, dislocations of rocks in direction NW–SE and discharges towards the south were observed.

https://doi.org/10.26376/GPR2018010

Horizontal geological drilling in the tunnel

In the walls of Wojanów tunnel, fifteen horizontal geological drillings were drilled to a depth of 2–4 m (Figure 1). Nine holes were made in the northern wall of the tunnel (from the T1 side) and six in the southern wall of the tunnel (from the T2 side). Geological drilling holes (indicated by "otw." in Figure 1) were made in the walls at a height of 1, 2, and 3 m above the floor (for borehole locations, see also Figure 2). The drilling shows that the granite blocks of the tunnel casing have a thickness of 30–55 cm. Behind the housing there is a strengthening zone (concrete, cement), which has a thickness up to 1.1 m (in some places up to 2 m). From 0.7 to 4.5 m there are granite debris, gravels and sands. Behind the casing of the tunnel, at a distance of 2–4 m, there is weathered granite, heavily cracked granite, or hard granite with rare cracks.

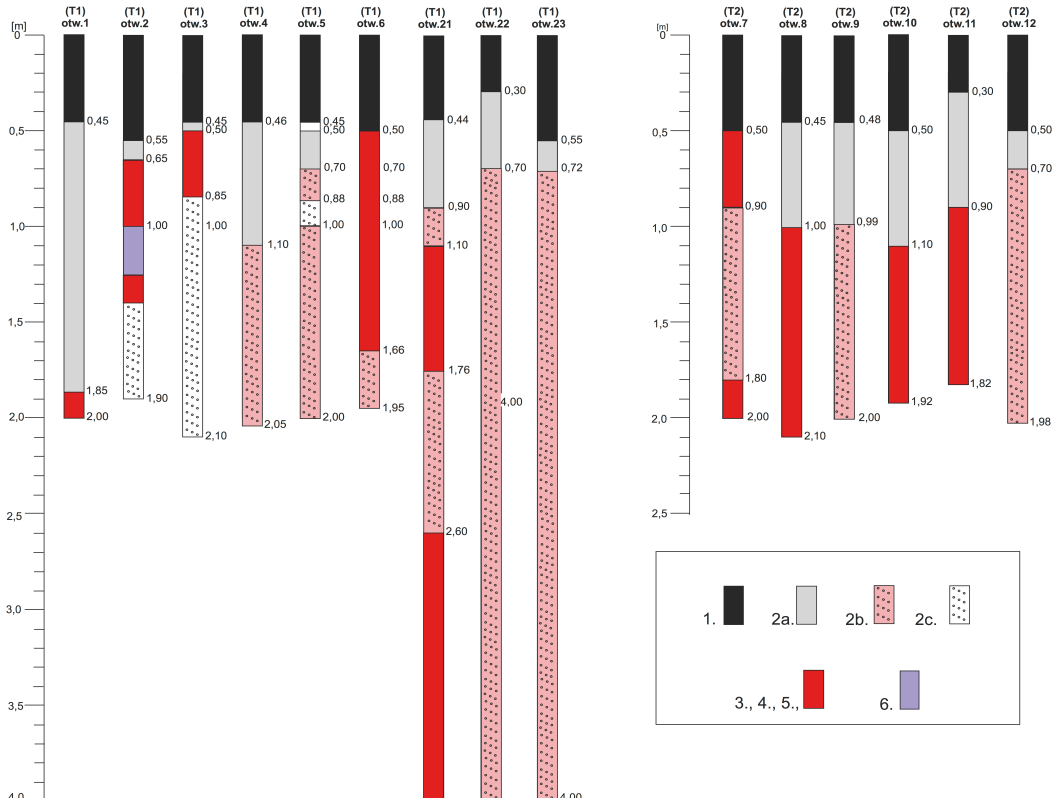

FIG. 1 – Lithology information about Wojanów tunnel, obtained by drilling its walls. Legend: 1 – housing made of granite rock block; 2a – concrete, cementation zone; 2b – granite weathering (gravel) plus granite fragments; 2c – gravel and sand; 3 – weathered granite; 4 – granite strongly cracked; 5 – solid granite (rare cracks); 6 – aplit.

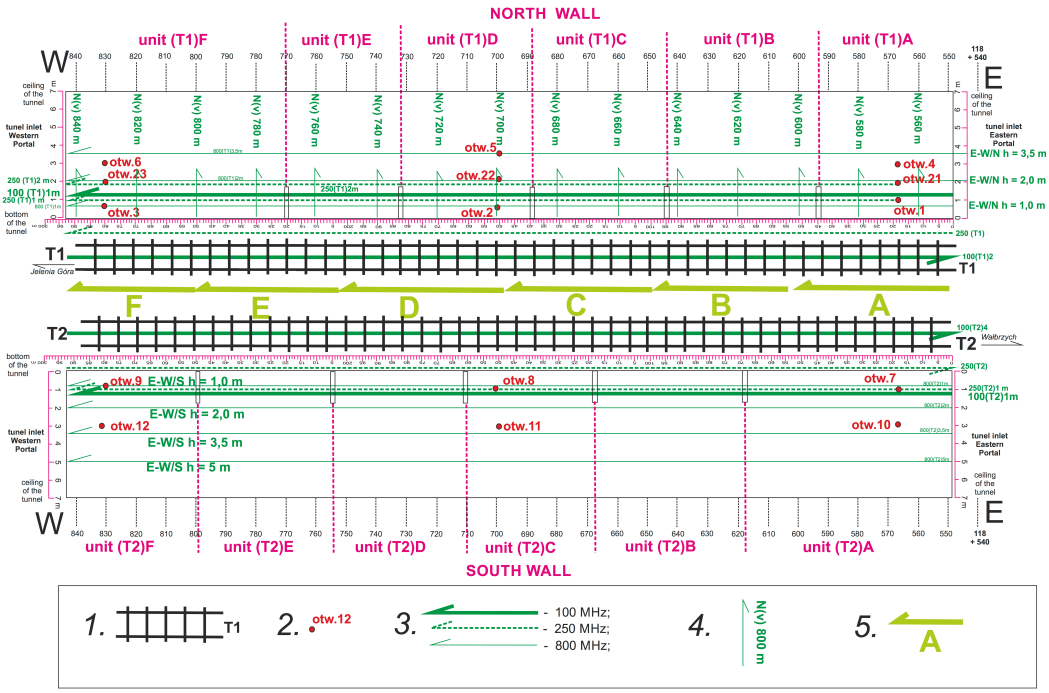

FIG. 2 – Scheme illustrating the GPR cross-section and borehole locations in Wojanów tunnel. Legend: 1) Tracks; 2) Horizontal boreholes; 3) Horizontal GPR cross-sections; 4) Vertical GPR cross-sections on the northern wall (800 MHz antenna); 5) GPR cross-section on the celling (800 MHz antenna).

Water in the area of the tunnel

The scheme of basic hydraulic properties for areas of occurrence of crystalline rocks [27] was used to visualize groundwater in the area of the tunnel. There are three aquifers (see Figure 3):

- Zone I - A weathering cover with variable thickness, high water capacity and low water conductivity. This is the zone that affects most the eastern and western inlets of the tunnel.
- Zone II - A densely fractured rock mass with high conductivity and low capacity.
- Zone III – A zone of deep circulatory pathways, which includes cracks accompanying fault zones, with the lowest capacity and hydraulic conductivity.

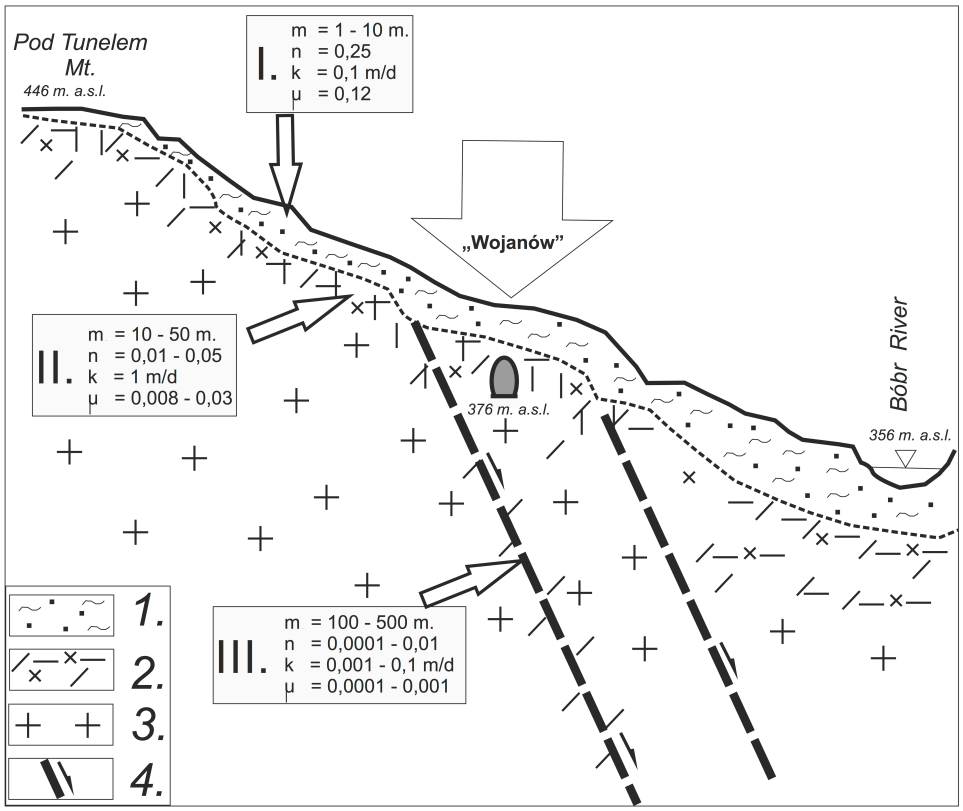

FIG. 3 – Occurrence of groundwater in Wojanów tunnel region, in areas of igneous and metamorphic rocks with low porosity but relatively high fissures, with reference to the geological and topographic situation of the tunnel. Legend: 1) Weathering cover; 2) Weathered and strongly cracked granite; 3) Cracked granite; 4) Fault zone. Symbols: m - thickness of the wet zone, n - effective porosity, k - filtration coefficient, μ - gravitational drainage.

2. METHODOLOGY OF GPR RESEARCH

GPR data collection

GPR research was carried out for the purposes of designing the tunnel renovation. To facilitate the description of research results and the identification of rock mass variability occurring behind the housing, the entire length of the tunnel (from the eastern portal towards the western portal) was divided into sections denominated as follows: from (T1)A to (T1)F and from (T2)A to (T2)F (see again Figure 2; note that the kilometers of the railway route are also reported in the scheme).

GPR measurements were carried out at night, when there was no train movement and it was possible to switch off the electricity in the

https://doi.org/10.26376/GPR2018010

electric traction. To work at the tunnel ceiling, a train was used which is normally employed to repair the electric traction. All tests were made with antennas facing the tunnel walls (Figure 4). Shielded antennas were used, with three central frequencies: 100, 250, and 800 MHz.

The following cross-sections were recorded with the use of 100 MHz antennas: over the tunnel, along the walls of the tunnel at a height of 1 m, and on the bottom of the tunnel (between the rails of railway tracks). The following cross-sections were recorded with the use of 250 MHz antennas: along the walls of the tunnel, at heights of 1 meter and 2 meter, along the tunnel bottom and along the base of the walls of the tunnel casing. Finally, cross-sections with the use of 800 MHz antennas were recorded along the tunnel walls, at heights of 1, 2, 3.5, and 5 m, as well as along the ceiling of the tunnel (see Figures 2 and 5).

Methodology for GPR data interpretation

Various color palettes and customary filter combinations were used to analyze GPR data. In Figure 6, an example of processed radargram is presented; this is a fragment of a cross-section recorded with 800 MHz antennas along the north wall, at 1 m height (the (T1) 800_1m cross-section). By using suitable filters, it was possible to improve the visualization of the gaps in the tunnel casing (radargram A in Figure 6) and of the housing blocks (part B in Figure 6). The calibration of the GPR radargram depth scale was made on the basis of drilling (Figure 7).

After selecting the color palette, applying filters, calibrating the depth scale, and obtaining a more readable image of the GPR data, the geological interpretation started. On the various GPR sections, the following lithological assemblies were distinguished: housing made of granite rock blocks; concrete and cementation zone; granite weathering (gravel) with granite fragments; weathered granite; strongly cracked granite; solid granite with rare cracks. An example is presented in Figure 8, where the following features are also shown: control points; niches in the tunnel walls; locations of drilling holes; housing border (housing blocks); boundary of cementing/concreting zone; boundaries between housing blocks together with cementation and clastic pieces behind the housing; boundary between mashing (weathered) and cracked, weathered granite rocks; detected anomalies. This approach was applied to all GPR cross-sections and a series of images were created.

https://doi.org/10.26376/GPR2018010

FIG. 4 – GPR research in Wojanów tunnel: 800 MHz antennas directed towards the ceiling of the tunnel housing.

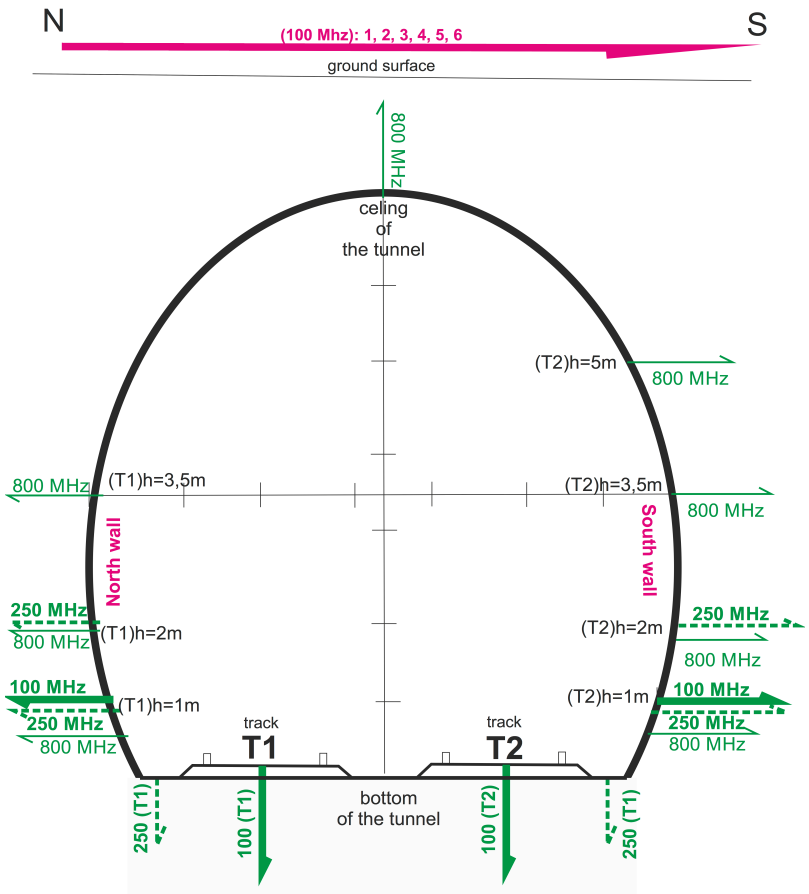

FIG. 5 – Location of GPR sections in Wojanów tunnel (schematic sketch).

https://doi.org/10.26376/GPR2018010

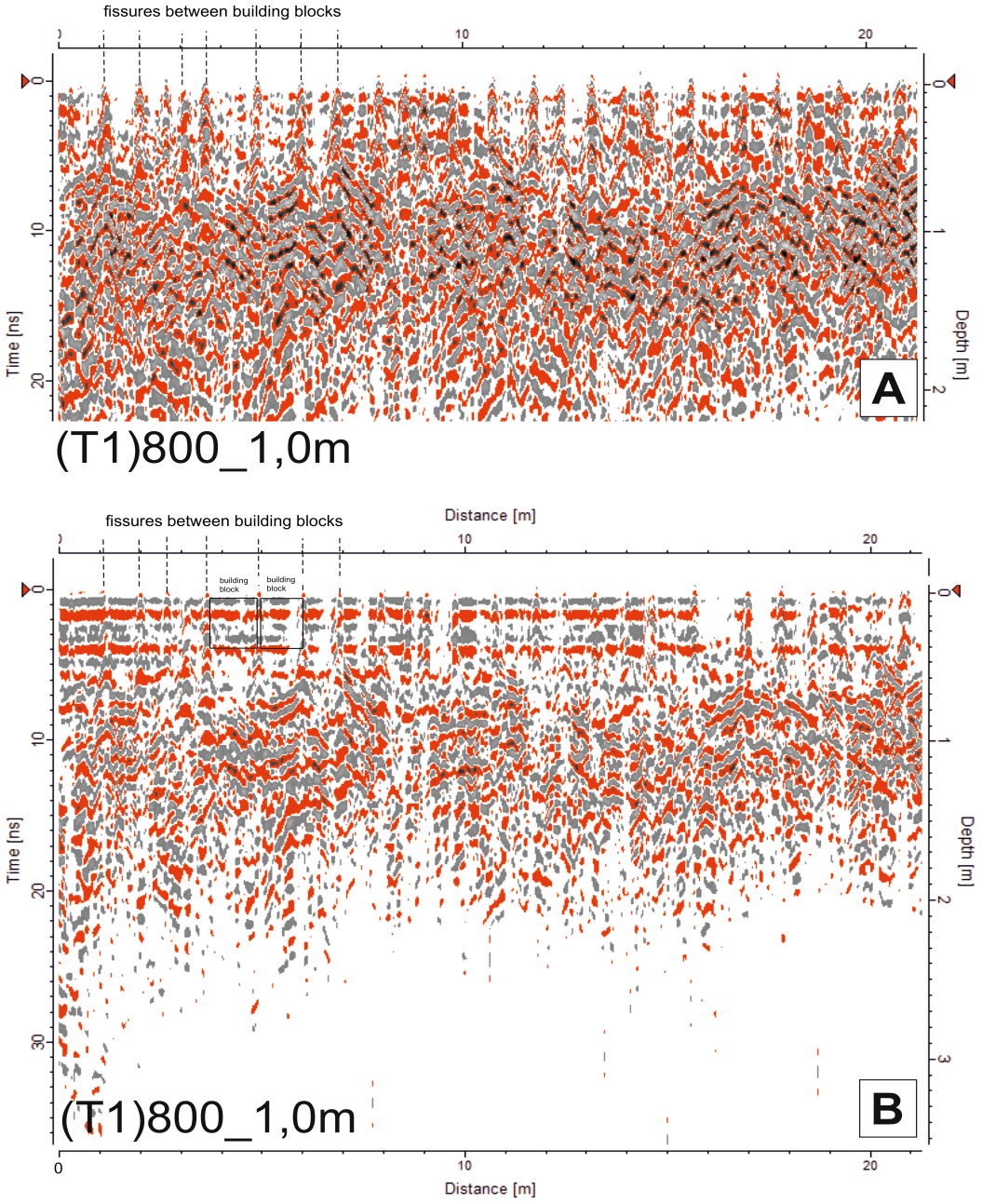

FIG. 6 – Fragment of a processed GPR cross-section recorded with 800 MHz antennas. Radargram A: the gaps between the housing blocks can be noticed; Radargram B: the blocks of the tunnel casing can be observed.

https://doi.org/10.26376/GPR2018010

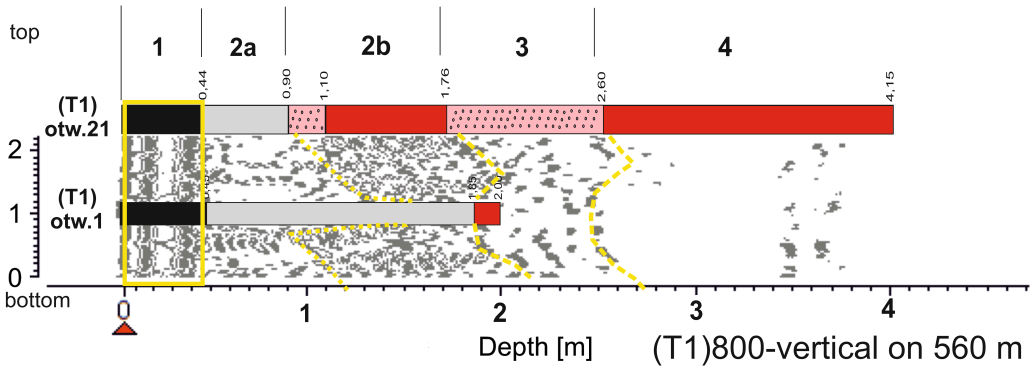

FIG. 7 – Depth-scale calibration and interpretation of GPR data, by exploiting two geological horizontal drillings in the northern wall of the tunnel, namely drillings (T1)otw.1 and (T1)otw.21. The GPR radargram is (T1)800MHz-vertical, at 560 m. The legend used for the lithology is the same as in Figure 1.

As expected, GPR cross-sections give information about the ground structures until different depths, when antennas working at different frequencies are used. In particular, the 100 MHz antennas allow reaching a depth of about 21-60 m from the ground surface; the 250 MHz antennas provide information up to about 7-9 m from the tunnel wall; and, the 800 MHz antennas allow reaching a depth of about 4 m from the wall surface of the tunnel. On two-dimensional GPR cross-sections, the depth error has been estimated as follows: approximately ± 1 m with the 100 MHz antennas, ± 0.5 m with the 250 MHz antennas, and ± 0.1 m with the 800 MHz antennas. On the GPR sections, the cementation zone cannot be distinguished from the weathering; this is probably due to the almost 100-year impact of destructive processes on the structure of the tunnel and on the rocks surrounding the tunnel.

3. RESULTS

From GPR tests carried out on the surface of the terrain over the tunnel it follows that behind the tunnel casing there is a zone of debris and rubble reaching up to a depth of about 5 m; see Figures 9 and 10 (the rubble and debris region is indicated with 2 in Figure 10). Behind, there is a zone of crumbled (and possibly weathered) granite that reaches

https://doi.org/10.26376/GPR2018010

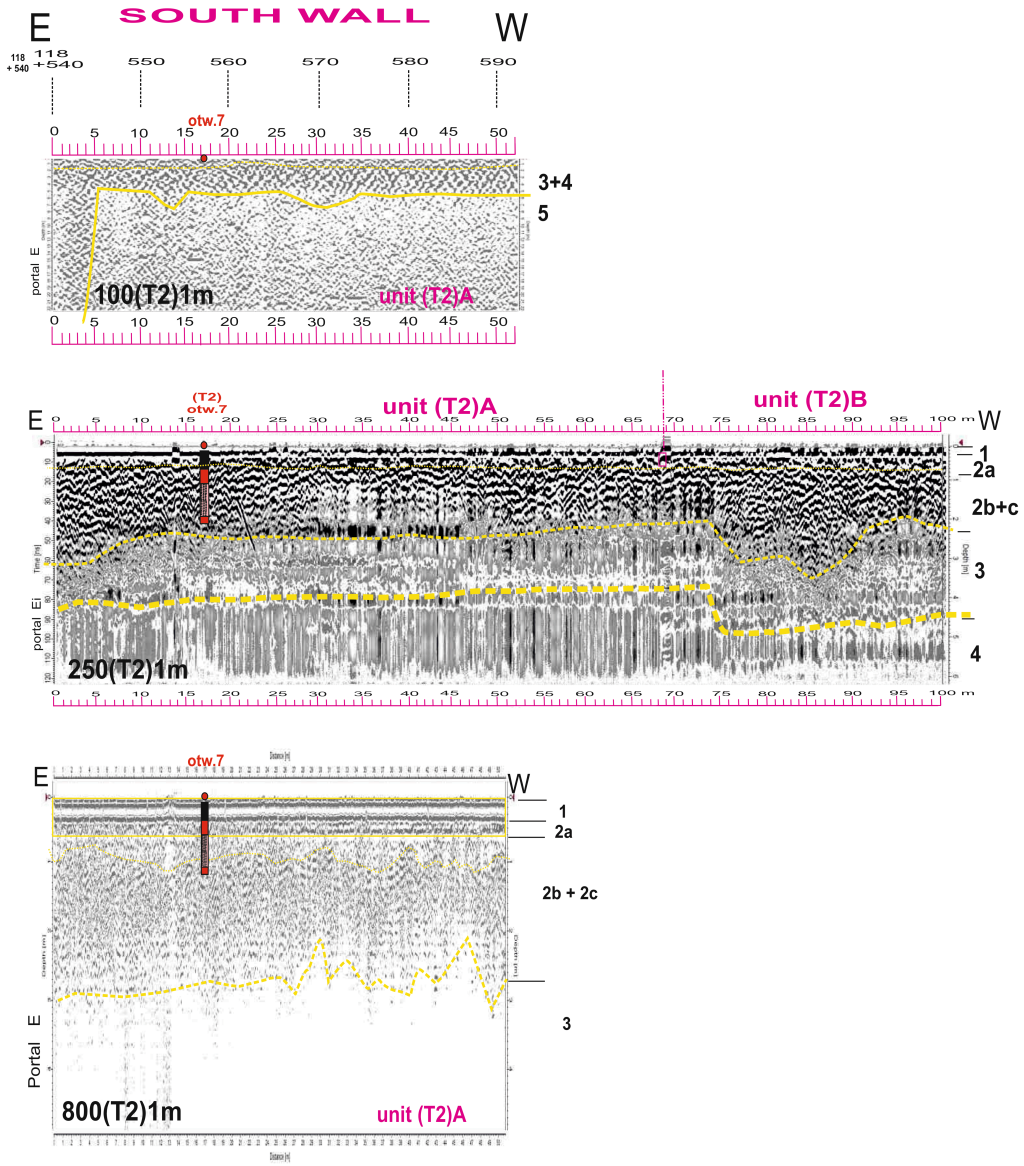

FIG. 8 – Comparison of GPR data obtained with different antennas (100 MHz, 250 MHz, 800 MHz) over a fragment of the southern wall of the tunnel (unit (T2)A). Cross-sections obtained at 1 m height from the floor of the tunnel. The legend used for the lithology is the same as in Figure 1.

north and south up to about 15 m from the tunnel's axis (indicated with 3 in Figure 10). It was also pointed out that on all cross-sections (made over the tunnel) there are characteristic structures of ground subsidence (4 in Fig. 10).

https://doi.org/10.26376/GPR2018010

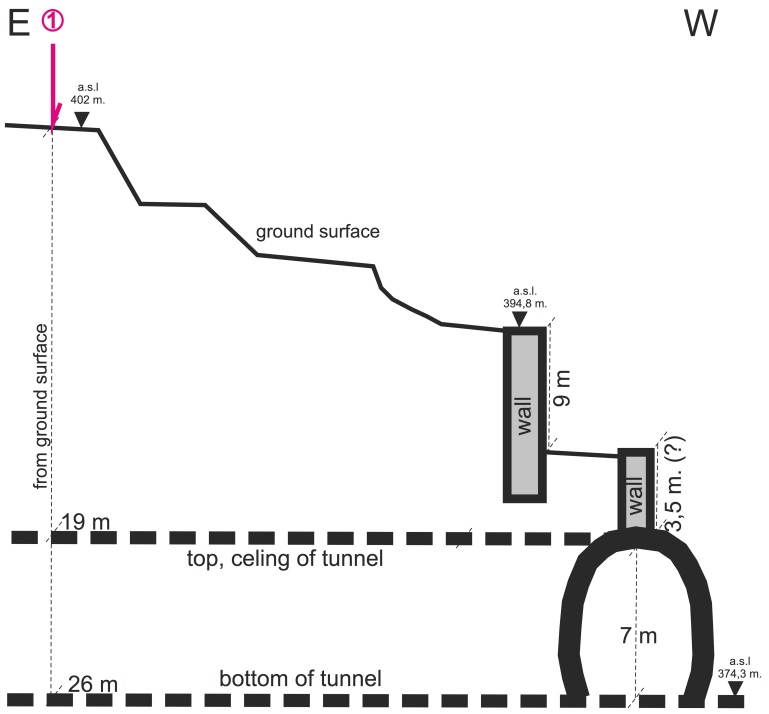

FIG. 9 – Location of GPR cross-section No. 1 (100 MHz), above the tunnel.

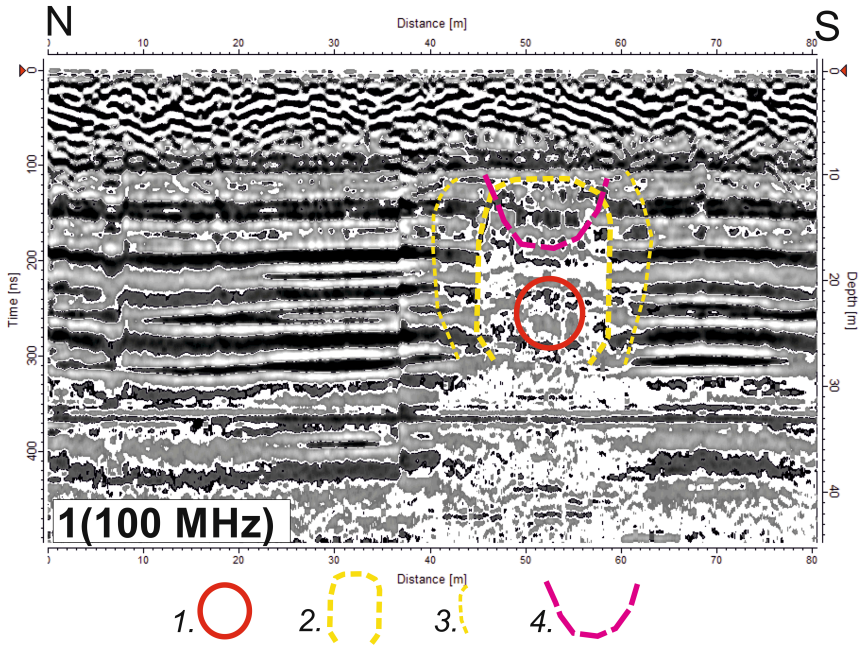

FIG. 10 – GPR Cross-section No. 1 (100 MHz), above the tunnel. Geological interpretation: 1) Tunnel, 2) Destroyed rock mass, sprinkle, weathered rocks; 3) Granite strongly cracked, weathered; 4) Ground subsidence zone above the tunnel ceiling.

https://doi.org/10.26376/GPR2018010

An exemplary fragment of a GPR cross-section recorded on the tunnel ceiling is presented in Figure 11 and clearly shows the condition of the ceiling. It is apparent that the housing blocks moved against each other, with a tendency to fall into the tunnel interior (1 in radargram A, in Figure 11). The cementing zone behind the casing in some places may be up to 1 m thick (2a in radargrams A and B, in Figure 11), and the rocks are crushed after it (2b in radargrams A and B, in Figure 11). The loss of housing blocks inside the tunnel is also confirmed by visual observations of the tunnel walls. In order to temporarily stop the movements of the housing blocks, suitable wooden wedges have been hammered into the interstices between the blocks (Figure 12).

Figures 13, 14 and 15 resume the results obtained by inspecting with GPR the north tunnel wall, at the T1 track and at a height of 1 m from the tunnel floor. In particular, results in Figure 13 were recorded by using the 100 MHz antennas; in Figure 14, results obtained with the 250 MHz antennas are presented; and, in Figure 15 results of investigations conducted with the 800 MHz antennas are shown.

The data obtained by using 100 MHz antennas allow to recognize only the boundaries between weathering and crumbling rocks (3/4 in Figure 13) and between crushed rocks and hard rocks (4/5 in Figure 13). This means that, with the help of 100 MHz antennas, the distance from the case to the hard rocks can be determined (5 in Figure 13) and the remaining boundaries are very poorly legible. These data do not provide information on the condition of the tunnel housing.

The results of the 250 MHz antenna tests allow to recognize only the boundary between weathered and weathered rocks (2/3 in Figure 14) and the boundary between weathered granites and strongly cracked rocks (3/4 in Figure 14). The cementation zone (2a in Figure 14) is barely visible, and the tunnel casing (1 in Figure 14) is poorly visible.

Finally, the data obtained by using the 800 MHz antennas clearly reveal the condition of the tunnel casing (1 in Figure 15), the cementing zone (2a in Figure 15), as well as the zone of weathered, gravel-sandy fillings (2b in Figure 15). The remaining boundaries are very poorly legible. A thorough analysis of data obtained from the 800 MHz antennas allows to visualize the gap widths in the tunnel casing (e.g., radargram A in Figure 6) and to illustrate the state of the tunnel casing blocks (e.g., radargram B in Figure 6).

https://doi.org/10.26376/GPR2018010

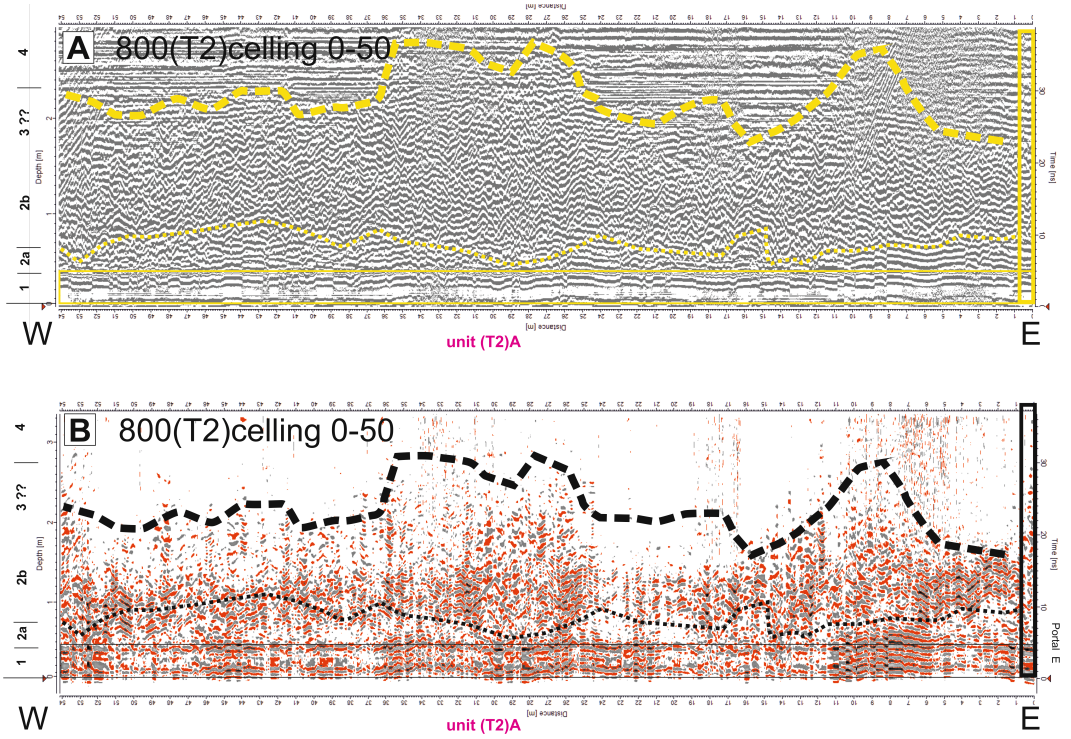

FIG. 11 – The ceiling of the tunnel: interpretation of GPR data recorded with 800 MHz antennas. Lithology numbers are the same as in Figure 1.

FIG. 12 – Photo of the tunnel ceiling, showing the falling blocks of the housing and the wooden wedges hammered into fissures between blocks to temporarily stop their movements.

https://doi.org/10.26376/GPR2018010

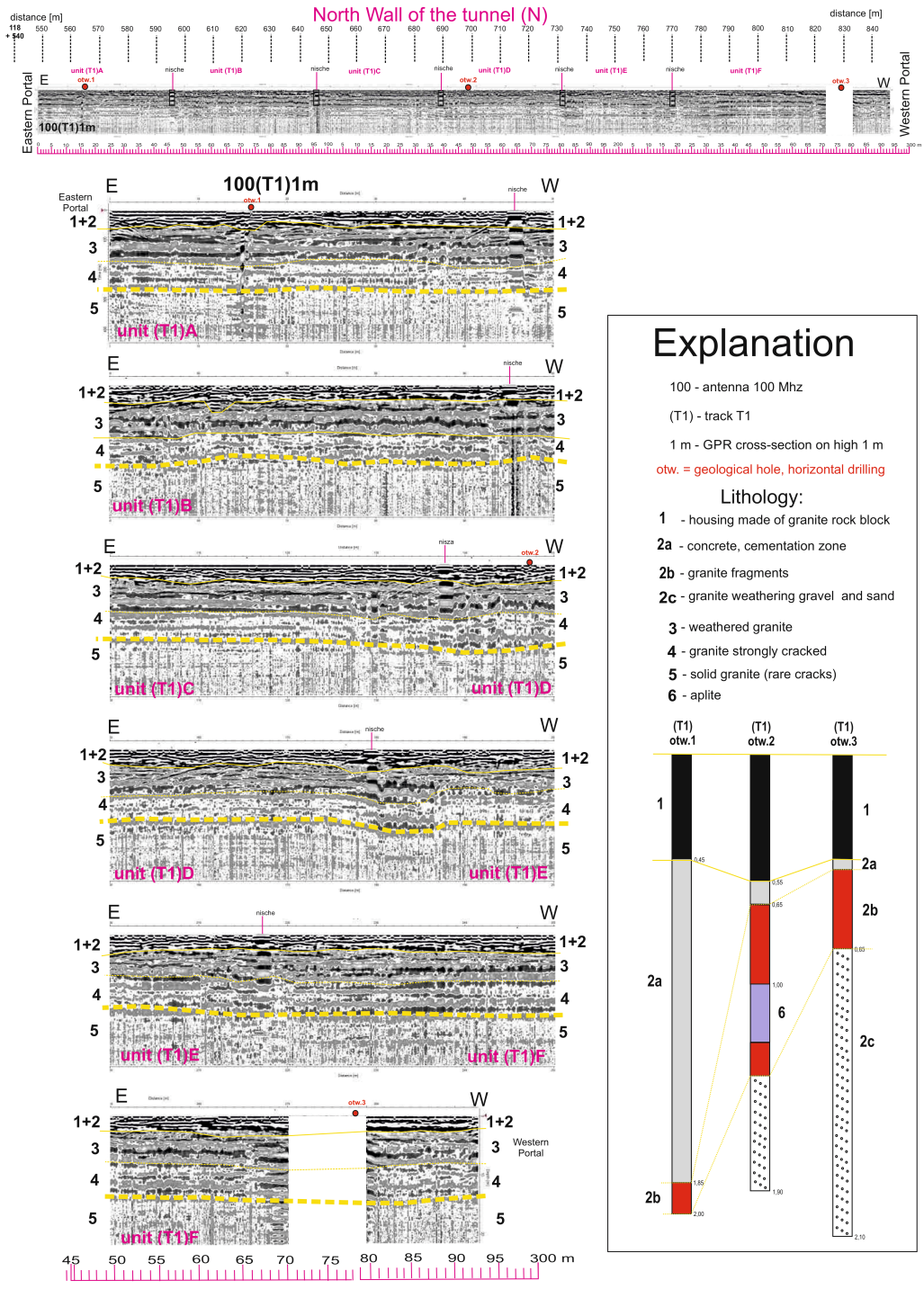

FIG. 13 – GPR cross-section obtained with 100 MHz antennas along the northern wall of the tunnel, at the T1 track and at a height of 1 m from the tunnel floor.

https://doi.org/10.26376/GPR2018010

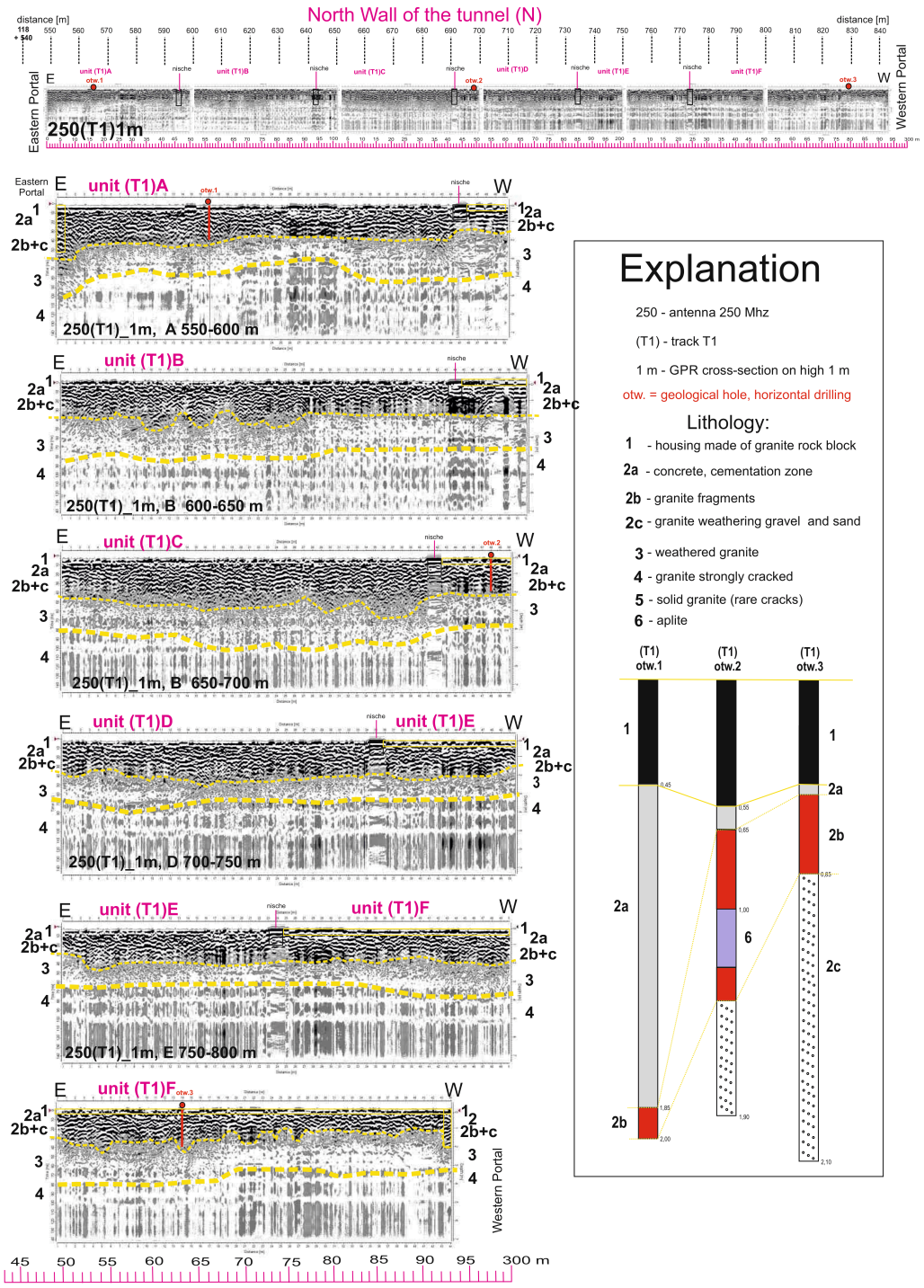

FIG. 14 – GPR cross section obtained with 250 MHz antennas along the northern wall of the tunnel, at the T1 track and at a height of 1 m from the tunnel floor.

https://doi.org/10.26376/GPR2018010

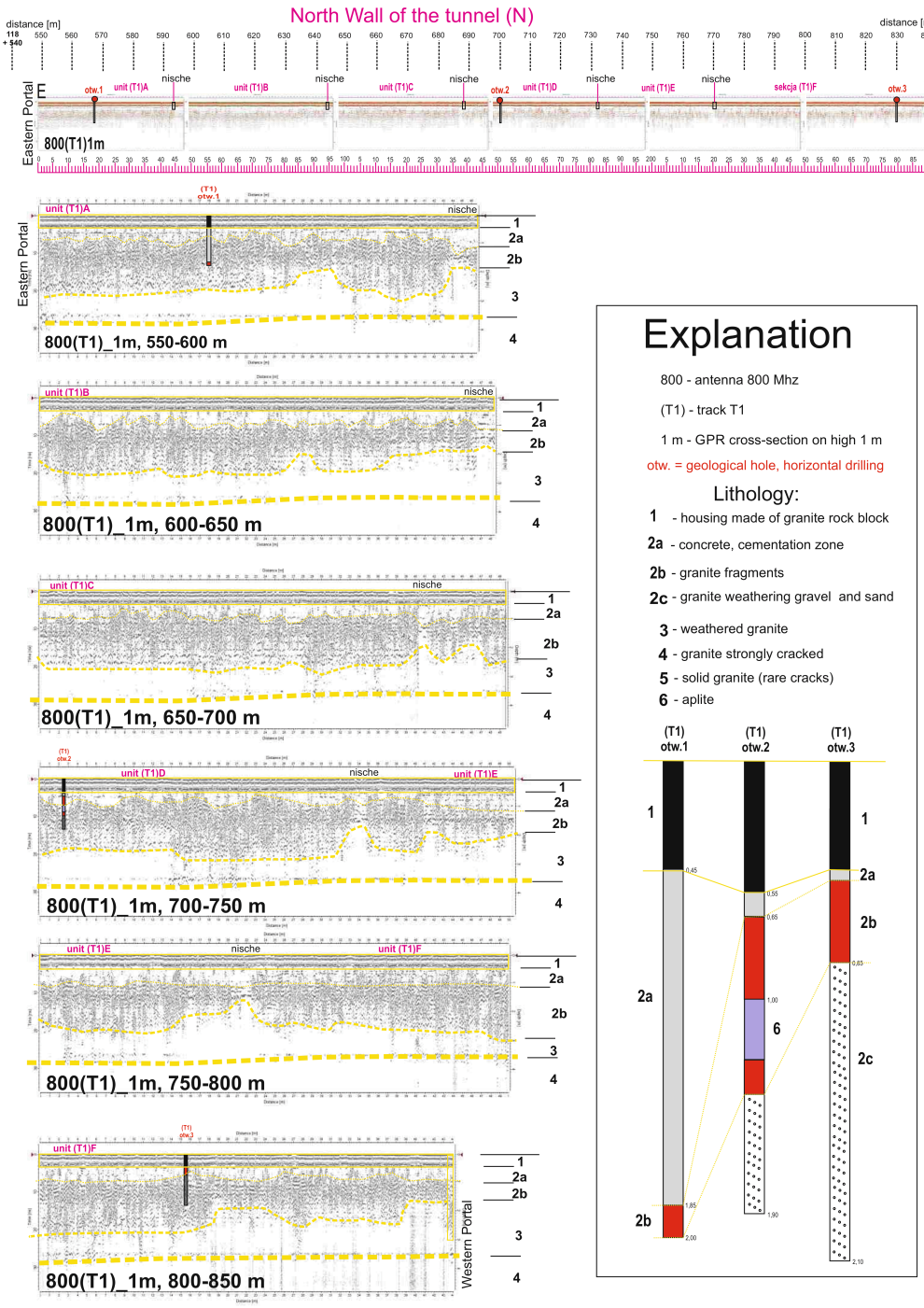

FIG. 15 – GPR cross section obtained with 800 MHz antennas along the northern wall of the tunnel, at the T1 track and at a height of 1 m from the tunnel floor.

https://doi.org/10.26376/GPR2018010

A preliminary analysis of GPR data in a three-dimensional system was done by Magdalena Udyrysz (Sumo Services, Poland). This was just a "trial analysis" because, due to budget constraints, the ordering company of this GPR study accepted to pay for the execution of just a few lines along the walls of the tunnel. It would have been interesting to implement a three-dimensional analysis for some vertical sections of the tunnel, too (e.g., from the base of the walls to the axis of the tunnel ceiling, at intervals of 1 m).

By using the 800 MHz antennas, horizontal, parallel cross-sectional lines were recorded at a height of 1, 2, and 3.5 m from the tunnel floor on wall N, as well as at a height of 1, 2, 3.5, and 5 m from the tunnel floor on wall S. Based on these data, an analysis in a three-dimensional system was performed; unfortunately, while maintaining the same scales (horizontal and vertical), the obtained drawings turned out to be too long and with low height (so they are poorly legible).

To illustrate the results of the analysis, examples are presented in Figures 16 and 17, for the southern and nothern walls of the tunnel, respectively. In the figures, sections and locations of bores made in the tunnel walls have been marked. On shallow time slices (e.g., from 0-0.15 m) niches in the tunnel walls can be clearly noticed (red points). On these "horizontal" time slices, warm colors (red, orange, yellow) correspond to anomalous spots indicating loosening in the tunnel casing or behind the tunnel casing.

In particular, let us examine more in detail Figure 16, recorded on the southern wall of the tunnel along T2: three examples of time cuts were chosen, corresponding to depths of 0-0.05 m, 2.49-2.54 m, and 3.28-3.33 m. Very poor condition of the housing (red, orange, yellow hues) can be observed on the tunnel section 0-56 m (time slice at a depth of 2.49-2.54 m) as well as on the tunnel section 2.40-2.95 m (time slice at a depth of 3.28-3.33 m), i.e., near the eastern and western tunnel portal.

Let us now examine more in detail Figure 17, recorded on the northern wall of the tunnel along track T1. In this case, very poor condition of the housing is on the tunnel section 0.8-2.15 m (time slice for a depth of 0.2-0.5 m). The worst situation is observed on the tunnel section 1.2-1.75 m (cut at a depth of 0.2-0.44 m).

https://doi.org/10.26376/GPR2018010

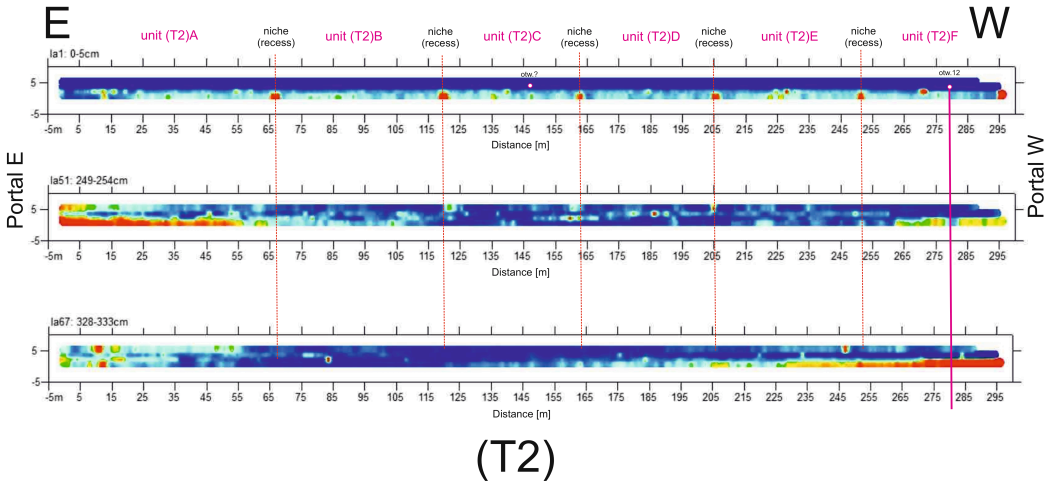

FIG. 16 – Southern wall of the tunnel, T2 track. Selected time slices.

For what concerns the bottom of the tunnelm, GPR cross-sections made in the tunnel along the railway tracks indicate that the sleepers under the rails lie on a subgrade build with crushed rock. Below, there is no concrete reinforcement (e.g., concrete slabs): the subgrade lies directly on a granite weathered cover or on cracked rock. Under the tracks, the covers of weathering, including the cracked rocks lying under them, extend until a depth of about 3-3.5 m. Below there are fractured granites in which fault zones have been found. These results are illustrated in Figure 18.

4. CONCLUSIONS

GPR tests in the area of Wojanów railway tunnel were made, with antennas having the following central frequencies: 100 MHz, 250 MHz, and 800 MHz. The linear profiling method was used and data were represented in a two-dimensional system.

GPR profiling was carried out: above the tunnel, near the west portal; along the ceiling of the tunnel; along the northern wall of the tunnel (1, 2, and 3.5 m above the tunnel's base); along the southern wall of the tunnel (1, 2, 3.5, and 5 m above the tunnel's base); all along the tunnel floor, on the two tracks, as well as close to the tunnel walls.

https://doi.org/10.26376/GPR2018010

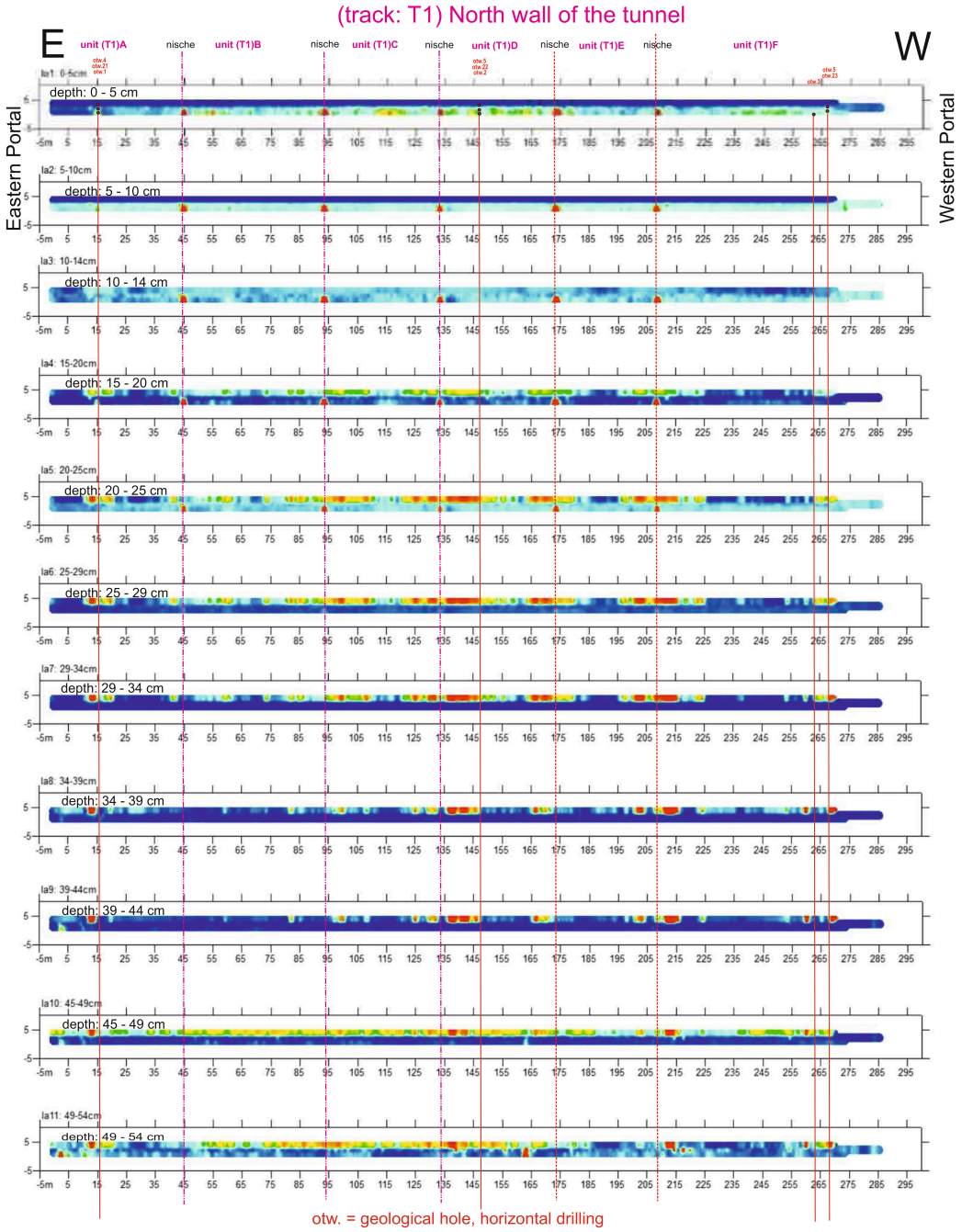

FIG. 17 – Northern wall of the tunnel, T1 track. Selected time slices.

https://doi.org/10.26376/GPR2018010

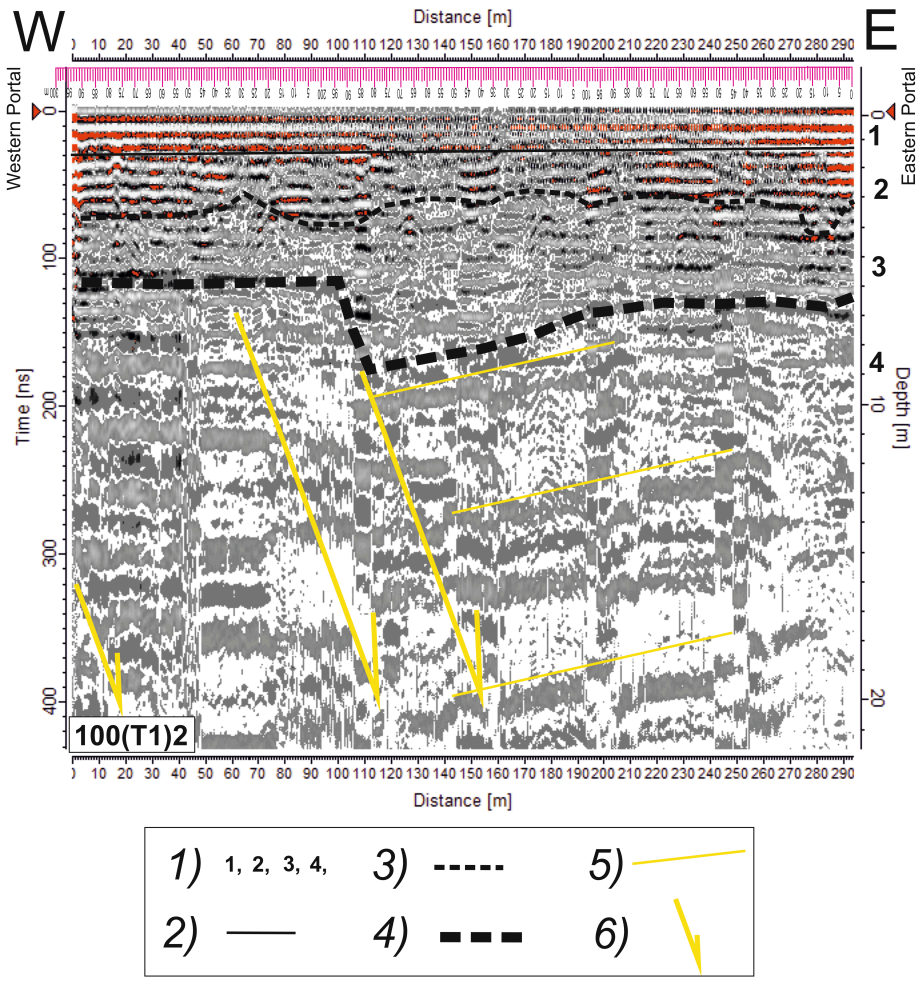

FIG. 18 – Floor of the railway tunnel, subgrade of the track. Interpretation of GPR data (100 MHz antennas). Lithology: 1) 1 – track foundations and subgrade crushed rock; 2 – weathered rock; 3 – strongly fractured rocks; 4 – solid granite; 2) subgrade limit; 3) weathered rocks limit; 4) strongly fractured rocks limit; 5) boundaries of rock layers; 6) faults, dislocations.

Calibration of the depth scale on GPR cross-sections was made on the basis of data from 15 horizontal geotechnical drillings. The estimated depth error on the vertical scale is: 1 m with the 100 MHz antenna, 0.5 m with the 250 MHz antenna, and 0.1 m with the 800 MHz antenna. The obtained GPR cross-sections give information about the ground structure down to the following depths: about 21-60 m from the ground surface with the 100 MHz antenna, approximately 7-9 m

https://doi.org/10.26376/GPR2018010

from the tunnel area/wall with the 250 MHz antenna, and about 4 m from the wall surface of the tunnel with the 800 MHz antenna.

On GPR cross-sections the following lithological assemblies can be distinguished and the forecasted boundaries between them are shown: 1) housing/granite blocks; 2a) concrete, cementation zone; 2b) granite debris (gravel) + granite fragments; 2c) gravel, sand; 3) weathered granite; 4) granite strongly cracked; 5) solid granite (rare cracks). On some cross-sections the systems of cracks in granite and possible faults can be observed. These structures have an inclination towards south.

The analysis of GPR data obtained with the 100 MHz antenna shows that behind the casing there is a zone of debris and rubble reaching down to a depth of about 5 m.

The analysis of GPR data obtained with the 250 MHz antennas shows that behind the housing there is a zone of cementation and weathering reaching down to a depth of about 2-4 m, behind such zone there is a crumbled zone of granite rocks (weathered?), which goes to a depth of 4-5 m from the surface of the tunnel casing.

The cross-sections obtained with the 800 MHz antenna show the condition of the tunnel casing (extended blocks, gap between the blocks, thickness of the housing blocks). However, a careful analysis of these data was not the goal of the research. To answer the question what is the condition of the housing, it would be necessary to enlarge the cross-sections and describe each block of housing separately.

The analysis of GPR data recorded with the 800 MHz antenna also shows that the housing blocks have variable thickness (up to 0.55 m). Behind the housing there is a variable thickness of the cementing zone. The cementing zone can reach a depth of 1.1 m (locally up to 2 m). Behind the casing there is a zone of debris and rock rubble reaching down to a depth of about 4 m (counting from the surface of the casing).

A preliminary analysis of GPR data in a three-dimensional system highlights a very poor condition of the housing and the zone behind the housing close to the western portal and near to the eastern portal (along sections of about 50 m).

For the anomalous zones detected in the two-dimensional system, it would be useful – as a future study – to perform a GPR survey on a

https://doi.org/10.26376/GPR2018010

fine grid and analyze data in a three-dimensional system (parallel cross-sections could be collected every 1 m or, even better, every 0.5 m), from the tunnel floor to the ceiling axis of the tunnel.

For accurate GPR tests in tunnels, it is recommended to divide the tunnel under test into smaller parts (units) and analyze them separately.

Acknowledgements

Thanks for financing and technical assistance during field tests to Wilhelm Janusz Szczurek (Biuro Inżynierskie Wrocław, Poland), Piotr Szczurek (Geostandard, Wrocław, Poland), Oktawia Ciapka (Politechnika Wrocławska, Wrocław, Poland), and to Magdalena Udyrysz (Sumo Services, Upton Severn, Worcestershire, England) for helping with the three-dimensional method.

References

[1] A. Benedetto and L. Pajewski, Eds. “Civil Engineering Applications of Ground Penetrating Radar,” Publishing House: Springer International; Book Series "Springer Transactions in Civil and Environmental Engineering;" April 2015; e-book ISBN: 9783319048130; hardcover ISBN: 9783319048123; doi: 10.1007/9783319048130; 371 pp.

[2] W. Wai-Lok Lai, X. Dérobert, and P. Annan, “A review of Ground Penetrating Radar application in civil engineering: A 30-year journey from Locating and Testing to Imaging and Diagnosis,” NDT & E International, vol. 96, pp. 58–78, June 2018, doi: 10.1016/j.ndteint.2017.04.002.

[3] O. Abraham and X. Dérobert, “Non-destructive testing of fired tunnel walls: the Mont-Blanc Tunnel case study,” NDT & E International, vol. 36, pp. 411–418, September 2003, doi: 10.1016/S0963-8695(03)00034-3.

[4] E. Cardarelli, C. Marrone, and L. Orlando, “Evaluation of tunnel stability using integrated geophysical methods,” Journal of Applied Geophysics, vol. 52, pp. 93–102, February 2003, doi: 10.1016/S0926-9851(02)00242-2

[5] A. G. Davis, M. K. Lim, and C. G. Petersen, “Rapid and economical evaluation of concrete tunnel linings with impulse response and impulse radar non-destructive methods,” NDT & E International, vol. 38, no. 3, pp. 181–186, April 2005, doi: 10.1016/j.ndteint.2004.03.011.

[6] G. Parkinson and C. Ekes, “Ground penetrating radar evaluation of concrete tunnel linings,” Proceedings of the 12th International Conference on

https://doi.org/10.26376/GPR2018010

Ground Penetrating Radar (GPR 2008), 16–19 June 2008, Birmingham, United Kingdom, 2008.

[7] F. Lehmann, "Practical application of non-destructive test methods at a single-shell tunnel lining," Proceedings of the 7th fib PhD Symposium, Stuttgart, Germany, 11–13 September 2008, published on the December 2008 issue of the e-Journal of Nondestructive Testing, pp. 1-10.

[8] A. Laluge and I. Hoff, "Determination of space behind precast concrete elements in tunnels using GPR," Proceedings of the 13th International Conference on Ground Penetrating Radar (GPR 2010), 21–25 June 2010, Lecce, Italy, doi: 10.1109/ICGPR.2010.5550195.

[9] F. Zhanga, X. Xie, and H. Huang, "Application of ground penetrating radar in grouting evaluation for shield tunnel construction," Tunnelling and Underground Space Technology, vol. 25, pp. 99-107, March 2010, doi: 10.1016/j.tust.2009.09.006.

[10] M.-J. Li, Y.-G. Zhao, H. Liu, Z. Wan, J.-C. Xu, X.-P. Xu, Y. Chen, and W. Bin, "Layer recognition and thickness evaluation of tunnel lining based on ground penetrating radar measurements," Journal of Applied Geophysics, vol. 73, no. 1, pp. 45–48, January 2011, doi: 10.1016/j.jappgeo.2010.11.004.

[11] J. Karlovsek, A. Schuerann, and D. J. Williams, "Investigation of voids and cavites in bored tunnels using GPR," Proc. 14th International Conference on Ground Penetrating Radar (GPR 2012), 4–8 June 2012, Shanghai, China, pp. 496–501, doi: 10.1109/ICGPR.2012.6254916.

[12] H.-Z. Yu, Y.-F. Ouyang, and H. Chen, "Application of Ground Penetrating Radar to Inspect the Metro Tunnel," Proc. 14th International Conference on Ground Penetrating Radar (GPR 2012), 4–8 June 2012, Shanghai, China, pp. 759–763, doi: 10.1109/ICGPR.2012.6254963.

[13] X. Xie and C. Zeng, "Non-destructive evaluation of shield tunnel condition using GPR and 3D laser scanning," Proceedings of the 14th International Conference on Ground Penetrating Radar (GPR 2012), 4-8 June 2012, Shanghai, China, pp. 479–484, doi: 10.1109/ICGPR.2012.6254913.

[14] X. Xiong, Q. Zhou, T. Zhou, Y. Ma, and K. Wan, "Application of GPR Technique and Research on High-speed Railway Tunnel," Proceedings of the 14th International Conference on Ground Penetrating Radar (GPR 2012), 4–8 June 2012, Shanghai, China, pp. 524–529, doi: 10.1109/ICGPR.2012 .6254920.

[15] Y. Hai-zhong, O. Yu-feng, and C. Hong, "Application of Ground Penetrating Radar to Inspect the Metro Tunnel," Proceedings of the 14th International Conference on Ground Penetrating Radar (GPR 2012), 4–8 June 2012, Shanghai, China, pp. 759–763, doi: 10.1109/ICGPR.2012.6254963.

https://doi.org/10.26376/GPR2018010

[16] L. Xiang, H.-L. Zhou, Z. Shu, S.-H. Tan, G.-Q. Liang, and J. Zhu, "GPR evaluation of the Damaoshan highway tunnel: a case study," NDT & E International, vol. 59, pp. 68–76, October 2013, doi: 10.1016/j.ndteint.2013.05.004.

[17] Q. Cun-chang, Z. Hui-lin, Y. Qi-ming, and Y. Xu, "Automatic detection of the grout layer of metro tunnel by GPR," Applied Mechanics and Materials, vol. 556–562, pp. 2719–2722, May 2014, doi: 10.4028/www.scientific.net/AMM.556-562.2719.

[18] A.M. Alani and K. Banks, "Applications of ground penetrating radar in Medway Tunnel – inspection of structural joints," Proceedings of the 15th International Conference on Ground Penetrating Radar (GPR 2014), Brussels, Belgium, 30 June – 4 July 2014, pp. 461–464, doi: 10.1109/ICGPR.2014.6970466.

[19] X. Núñez-Nieto, M. Solla, F. J. Prego, and H. Lorenzo, "Assessing the applicability of GPR method for tunnelling inspection: Characterization and volumetric reconstruction," Proceedings of the 8th International Workshop on Advanced Ground Penetrating Radar (IWAGPR 2015), Florence, Italy, 7–10 July 2015, pp. 1–4, doi: 10.1109/IWAGPR.2015.7292633.

[20] J. White, S. Hurlebaus, P. Shokouhi, and A. Wimsatt, "Nondestructive Testing Methods for Underwater Tunnel Linings: Practical application at Chesapeake channel tunnel," Proceedings of the 2015 International Symposium on Non-Destructive Testing in Civil Engineering, Berlin, Germany, 15–17 September 2015, pp. 1–4.

[21] Q.-M. Yu, H.-L. Zhou, Y.-H. Wang, and R.-X. Duan, "Quality monitoring of metro grouting behind segment using ground penetrating radar," Construction and Building Materials, vol. 110, pp. 189–200, May 2016, doi: 10.1016/j.conbuildmat.2015.12.109.

[22] A. Lalague, M. Lebens, I. Hoff, E. Grov, "Detection of Rockfall on a Tunnel Concrete Lining with Ground-Penetrating Radar (GPR)," Rock Mechanics and Rock Engineering, vol 49, pp. 2811-2823, July 2016, doi: 10.1007/s00603-016-0943-y.

[23] A. M. Alani and F. Tosti, "GPR applications in structural detailing of a major tunnel using different frequency antenna systems," Construction and Building Materials, vol. 158, pp. 1111–1122, January 2018, doi: 10.1016/j.conbuildmat.2017.09.100.

[24] S. Cwojdziński and W. Kozdrój, "Detailed Geological Map of Poland on a scale of 1:50000, sheets Wojcieszów," [In Polish] "Szczegółowa Mapa Geologiczna Polski w skali 1:50000, ark. Wojcieszów," Państwowy Instytut Geologiczny - PIB, Warszawa, Poland, 2006.

https://doi.org/10.26376/GPR2018010

[25] M. Mierzejewski, “Decision regarding damage to a linear tunnel at km 118.548–118.841 railway line Wrocław-Jelenia Góra,” [In Polish] “Orzeczenie w sprawie uszkodzeń tunelu liniowego w km 118.548–118.841 linii kolejowej Wrocław–Jelenia Góra,” in: A. Solecki and W. Śliwiński, “Results of geophysical profiling using the EM31 apparatus in the tunnel on the Wrocław-Jelenia Góra route,” [In Polish] “Wyniki profilowania geofizycznego przy użyciu aparatu EM31 w tunelu na trasie Wrocław–Jelenia Góra,” Instytut Nauk Geologicznych Uniwersytetu Wrocławskiego Pracownia Usług Geologicznych “WRO-MIN,” Wrocław, Dec. 1995, pp. 4 + 2 Figs.

[26] M. Szałamacha and K. Tucholska, “Detailed Geological Map of the Sudetes in the scale of 1:25000, Jelenia Góra East sheet,” [In Polish] “Szczegółowa Mapa Geologiczna Sudetów w skali 1:25000. Ark. Jelenia Góra Wschód,” Wydawanie Geologiczne, Warszawa, 1957.

[27] S. Staśko and R. Tarka, “Supply and drainage of groundwater in mountain areas on the basis of research in the Śnieżnik massif,” [In Polish] “Zasilanie i drenaż wód podziemnych w obszarach górskich na podstawie badań w masywie Śnieżnika,” Acta Universitatis Wrat., Prace Geologiczne-Mineralogiczne, 2528, pp. 1–86, Uniwersytet Wrocławski, 2002.

https://doi.org/10.26376/GPR2018010

Ground Penetrating Radar
The first peer-reviewed scientific journal dedicated to GPR

MODEL-BASED CLUTTER REDUCTION METHOD FOR FORWARD LOOKING GROUND PENETRATING RADAR IMAGING

YUKINORI FUSE[1], BORJA GONZALEZ-VALDES[2],
JOSE A. MARTINEZ-LORENZO[1] & CAREY M. RAPPAPORT[1]

[1] DEPARTMENT OF ELECTRICAL AND COMPUTER ENGINEERING, NORTHEASTERN UNIVERSITY, BOSTON, MASSACHUSETTS, UNITED STATES OF AMERICA – YFUSE@ECE.NEU.EDU; JMARTINE@ECE.NEU.EDU; RAPPAPORT@COE.NEU.EDU

[2] UNIVERSITY OF VIGO, VIGO, SPAIN – BGVALDES@COM.UVIGO.ES

ABSTRACT

Model based imaging methods for a dual-band fully polarimetric vehicle-based Forward-Looking Ground Penetrating Radar (FLGPR) are presented. The radar consists of two fully polarimetric arrays of wideband horns - one at L-band and one at X-band - that form synthetic apertures as the vehicle advances. Model-based clutter suppression image processing is used to clean the Synthetic Aperture Radar (SAR) image obtained from the VV polarized L-band radar by employing a mixed binary mask. This clutter mask is formed from the second (X-band) frequency and the VH cross-polarized L-band responses. Receiver Operating Characteristic (ROC) curves using measured field data are used to evaluate the enhancement of the target signal to clutter ratio. The proposed methods reduce the false alarm rate and improve the detection performance of the system.

KEYWORDS: Imaging system; Synthetic Aperture Radar (SAR); Forward-Looking Ground Penetrating Radar (FLGPR).

1. INTRODUCTION

Ground Penetrating Radar (GPR) is widely used to detect subsurface objects [1] including explosive devices such as mines and Improvised Explosive Devices (IEDs). Other detection sensors include infrared (IR) cameras [2], [3], acoustic detectors [4], and laser-induced breakdown spectroscopy [5]. Forward-Looking Ground Penetrating Radar (FLGPR) has the advantages of sensing below the ground surface while having a large stand-off distance between the sensor systems and buried threats, and covering a wide detection area [6], [7]. These advantages lead to improved safety and efficiency for operators during the detection process. However, a major problem with FLGPR is clutter resulting from

https://doi.org/10.26376/GPR2018011

scattering from the rough ground surface; including large rocks, large depressions, and objects on the surface like trees, bushes, and manmade items. It is important to suppress this clutter from on- or above-ground objects in order to detect threatening objects below the ground surface and reduce the false alarm rate. Several methods have been proposed to solve this problem. One approach is based on extracting the characteristics and features of the target signal and classifying the received signals to extract the target signals from FLGPR image [8]–[10]. Another reduces the false alarms by combining FLGPR image results with other types the sensors. Combined FLGPR and IR sensor information has been studied in [11], [12]. The IR features are extracted from a vehicle mounted IR camera and IR images provide the clutter locations, which are not available in FLGPR, to eliminate false alarms. Another sensor combination (FLGPR and visible-spectrum colour camera) has been studied in [13]. The information from the visible camera is used for reducing the false alarms. FLGPR image data is used directly while the camera is used to extract the features of the target signals or eliminate the clutter. In this work, a model-based clutter suppression method is presented. The method is validated with field measurement data experimentally generated by the United States (US) Army, Communications-Electronics Research, Development and Engineering Center (CERDEC), Night Vision and Electronic Sensors Directorate (NVESD). The FLGPR system is a dual-band radar system with L-band (0.75 ~ 3.2 GHz) and X-band (8 ~ 12 GHz) radars (Table I).

The L-band radar is fully polarimetric while X-band radar is VV (vertical transmitting, vertical receiving) - polarized. The scattering from above-ground objects tends to be strong for both X-band and L-band radar, while the X-band and the VH (vertical transmitting, horizontal receiving) cross-polarization responses of buried targets are weak. This is due to higher frequency waves being attenuated as they propagate through soil, and the depolarizing effects of the wave refraction at the ground interface for VH scattered waves. Using X-band and VH L-band signals to identify clutter signals with minimal response from subsurface objects provides a method to uniquely distinguish buried targets. The model-based response at the receiving array due to the primary clutter objects is subtracted from the original VV polarized L-band signal, and a new clutter-suppressed Synthetic Aperture Radar (SAR) image is generated.

https://doi.org/10.26376/GPR2018011

TABLE I – FLGPR SYSTEM.

	L-band radar	**X-band radar**
Antennas	8 transmitters, 8 receivers	32 transmitters, 4 receivers
Frequency bandwidth	0.75 GHz – 3.2 GHz	8.4 GHz – 10.4 GHz
Polarization	VV, HH, VH, HV	VV

2. MODEL BASED CLUTTER SUPPRESSION METHOD

This section presents the methodology for selectively suppressing above-ground clutter. The proposed dual-wideband FLGPR system properties are described in Table I. The L-band radar has 8 transmitters and 8 receivers, and the X-band radar has 32 transmitters and 4 receivers. A Global Positioning System (GPS) is mounted on the system so that the array position can be obtained at each location. The reconstructed wideband array based images can be added together coherently with using multiple frames in range direction to form SAR image.

The main steps of this method are as follows:

Step 1) Generate the VV L-band SAR image.
Step 2) Generate the VH L-band SAR image.
Step 3) Generate the VV X-band SAR image.
Step 4) Segment the reconstruction area into four sub-regions in range for separate processing.
Step 5) Form binary masks with a 1 at pixels with reflectivity above - or 0 for reflectivity below - a given threshold.
Step 6) Multiply the original image from 1) with the binary masks.
Step 7) Model the response at the L-band receiving antenna array due to just the masked reconstructions at each sub-region.
Step 8) Compute the VV L-band SAR image from the cleaned response.

2.1 SAR imaging and reflectivity reconstruction

The reflectivity of all objects in the imaging area is reconstructed using wideband array-based radar imaging as given by:

https://doi.org/10.26376/GPR2018011

$$x(X_p, Y_p) = \sum_n^N \sum_m^M \sum_k^K b(f_k)\ exp\left[j\frac{2\pi f_k}{c} L_{mn}(X_p, Y_p)\right] \quad (1)$$

where x is output SAR image pixel value, $b(f_k)$ is measured observed data set, f_k is the k^{th} operating frequency and $L_{mn}(X_p, Y_p)$ is the total path length between the n^{th} transmitter at $(X_{trs,n}, Y_{trs,n}, Z_{trs,n})$ to the p^{th} image pixel at (X_p, Y_p), and then to the m^{th} receiver at $(X_{rcv,m}, Y_{rcv,m}, Z_{rcv,m})$. So $L_{mn}(X_p, Y_p)$ can be expressed as:

$$L_{mn}(X_p, Y_p) = \sqrt{(X_{rcv,m} - X_p)^2 + (Y_{rcv,m} - Y_p)^2 + Z_{rcv,m}^2} + \sqrt{(X_{trs,n} - X_p)^2 + (Y_{trs,n} - Y_p)^2 + Z_{trs,n}^2} \quad (2)$$

The geometry of the FLGPR imaging system is shown in Figure 1.

Equation (1) can be expressed in a reshaped matrix form approximate solution given by [14]:

$$\mathbf{x} = \mathbf{A}^{\dagger} \cdot \mathbf{b} \quad (3)$$

where $\mathbf{x}$ and $\mathbf{b}$ are $p \times 1$ and $mnk \times 1$ column matrices representing the reflectivities (or image) and the measured radar responses, respectively, and $\mathbf{A}^{\dagger}$ is the adjoint (conjugate transpose) of the scattering matrix $\mathbf{A}$. The image x can be added coherently for multiple frames in the down-track direction. The final SAR image is given by the coherent (complex) sum:

$$x_{multi}(X_p, Y_p) = \sum_{fr} x(X_p, Y_p) \quad (4)$$

where fr is the number of frames in the range direction.

2.2 Mask formulation

A binary mask is derived from the L-band VV polarization, VH polarization, and the X-band VV polarization SAR images. The imaging area is nominally divided into four sub-regions. This is necessary to compensate for the spreading of the radiated waves, which reduces the amplitude of the received signals from distant scatterers. The binary mask $\mathbf{m}$ is generated by finding the pixel values with magnitude exceeding a given threshold and setting them to 1, while all other pixels are set to 0. The details of the procedure of the mask formulation are in Sub-section 2.4.

https://doi.org/10.26376/GPR2018011

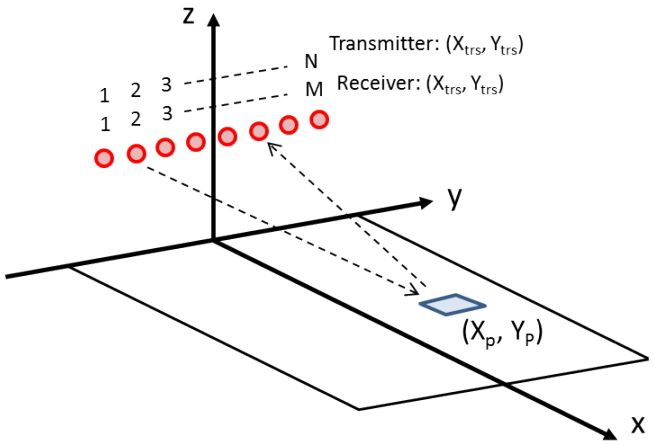

FIG. 1 – Imaging system geometry.

2.3 Masking L-band data

A matrix is overlaid on the original L-band image by simply multiplying pixel by pixel: $\hat{x}_i = m_i x_i$. The $\hat{\mathbf{x}}$ image is now used to derive the new simulated observed clutter-only response $\hat{\mathbf{b}}$ given by:

$$\widehat{\mathbf{b}} = \mathbf{A} \cdot \hat{\mathbf{x}} \tag{5}$$

Finally, the new suppressed clutter image $\mathbf{x}'$ is expressed as:

$$\mathbf{x}' = \mathbf{A}^{\dagger} \cdot (\mathbf{b} - B\hat{\mathbf{b}}) \tag{6}$$

where B is a normalizing amplitude adjustment coefficient. B is expressed as the ratio between the maximum magnitudes of $\hat{\mathbf{x}}$ and the maximum magnitudes of the SAR image $\mathbf{x}'_2$ given by the new cleaned measured response $\hat{\mathbf{b}}$. The amplitude adjustment coefficient B can be written as:

$$B = Max(\hat{\mathbf{x}})/Max\,(\mathbf{x}'_2) \tag{7}$$

with

$$\mathbf{x}'_2 = \mathbf{A}^{\dagger} \cdot \hat{\mathbf{b}} \tag{8}$$

In the case of the plural masks in one image, B has to be derived in each sub-region area, respectively, to obtain the best-subtracted SAR image. In addition, this procedure can be used repeatedly to suppress the clutter signals using the same mask in each frame. The effect of this iteration is shown in the following sections.

https://doi.org/10.26376/GPR2018011

2.4 Mask creation procedure

The procedure for combining the L-band VV, VH, and X-band masks is presented in this subsection. The masking image is derived from L-band VV pol, VH pol SAR images and the X-band SAR image. The pixel values with magnitude exceeding a given threshold are set to 1, while all other pixels are set to 0, creating a binary mask row matrix.

The masking area is created based on the shape of the L-band VV pol mask, because these regions constitute the dominant clutter in the simulated SAR image. The region shapes are weighted with the other sensor data to ensure that they do not represent target signal responses. The combination of the responses are eventually subtracted from the original L-band VV polarization received signals. The concept of mask creation is described in Figure 2. The final mask is composed of two parts: the fundamental part and the extended part. Fundamental part is able to cover the most part of the clutter region, however when some large clutter signals exist at the roadside, they could be potential false alarms. The spatially filtered mask with a lower threshold can be applied only for the roadside region. In the fundamental part of the mask, each region of L-band VH pol binary mask and X-band binary mask is compared to the region of L-band VV pol binary mask, and the intersection is selected as the masking area. The combined L-band VV and VH pol mask and the combined L-band VV and X-band binary mask are added to form the final mixed binary mask. The thresholds are selected from calibration cases to be as low as possible without compromising the target signal response.

In the extended part, the masks are formed with the lower threshold to cover a wider clutter area. The region of L-band VH pol binary mask with a lower threshold is compared to the region of L-band VV pol binary mask with a similar lower threshold. In addition, the L-band VH pol binary mask with a lower threshold is used as one of the selected masking areas. The union of the binary masks forms the final masking image for the extended part. Afterward, the combined mask is spatially selected for the roadside area: -10 ~ -4 m and 4 ~ 10 m in cross-range, and added to the final mask for the fundamental part. The thresholds are derived by the average valued of the road-side clutter in a frame in test lane.

https://doi.org/10.26376/GPR2018011

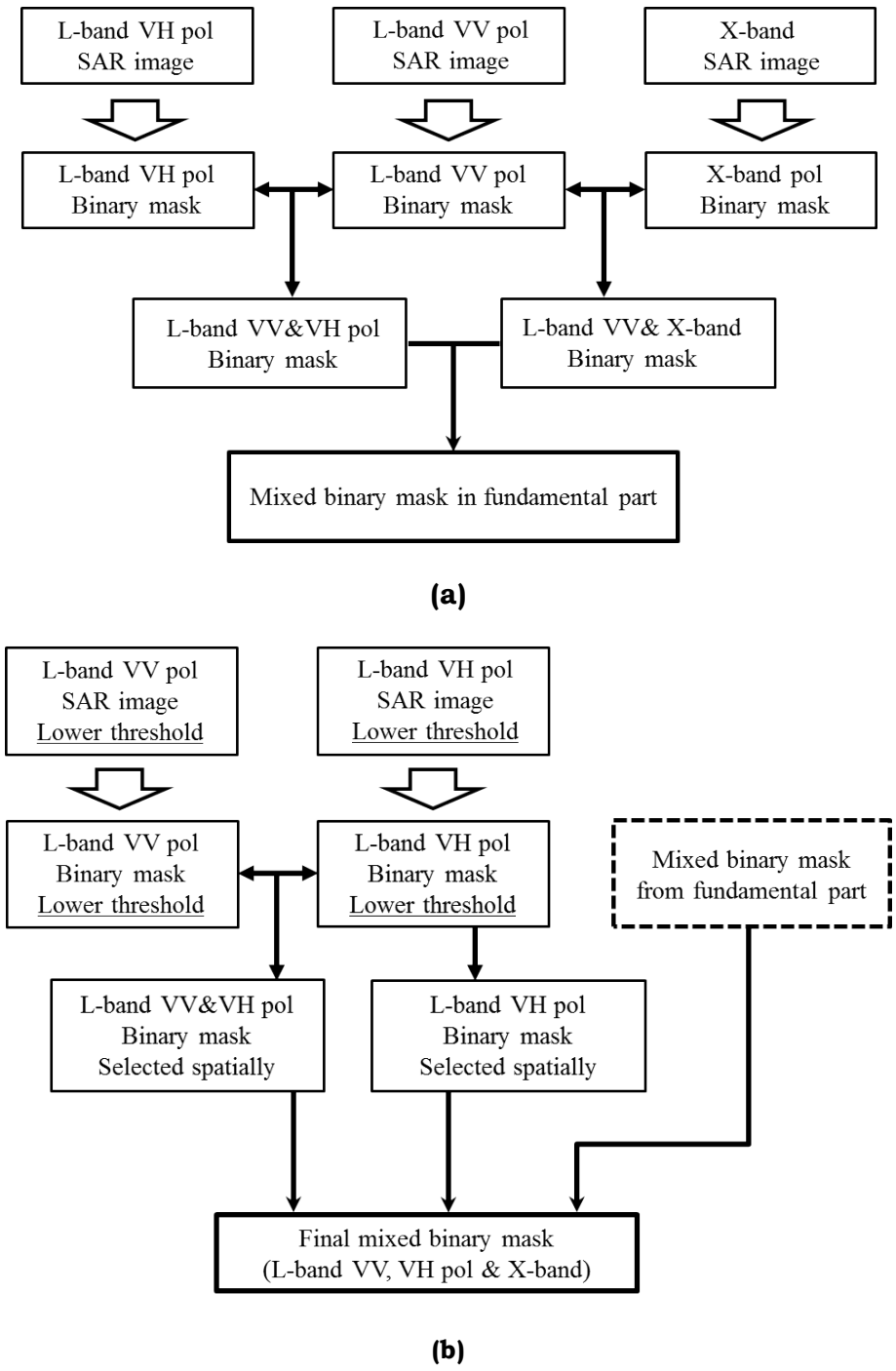

FIG. 2 – Procedure of the mask creation: **(a)** Fundamental part of the mask; **(b)** Extended part of the mask.

https://doi.org/10.26376/GPR2018011

3. RESULTS

3.1 Mask effectiveness

Examples of the fundamental part of each SAR image, and binary mask of L-band VV pol, VH-pol, and X-band radar are presented from Figure 3 [15] to Figure 5. Figure 6 shows the mixed binary mask for the fundamental part and the extended part. Green triangle marker shows the buried target position. In this case, some targets are buried at almost the same location. It is observed that the mixed binary mask covers just the clutter area and not the target image positions.

3.2 Iterative clutter suppression method

The effect of iteration on the masking process with multiple frames is presented. The $\hat{\mathbf{b}}$ in (5) is obtained with the L-band VV polarization image multiplied by the mixed binary mask, and the new processed SAR image is created. This procedure can be applied repeatedly until the clutter signal is sufficiently suppressed. The process is applied iteratively up to 7 times, with the goal of reducing the clutter power below the power of the buried target images.

The processed images can be combined by coherent averaging. Several combinations are proposed in Table II and some examples of masking process results are presented in Figure 7. The representative clutter power levels are chosen from two clutter regions which are highlighted with light green rectangles in Figure 3(a). Based on this figure, by increasing the number of iterations, the clutter power is getting smaller while the target signals still remain. The effect of these combinations is quantified in Figure 8(a), and Figure 8(b) shows the result without coherent averaging, for comparison.

The clutter signals are mixed and effectively cancelled out by taking the average of multiple iterations. The clutter signal's power is decreased about 26.5 dB compared to the original SAR image. It indicates achieving about 5.03 dB reductions in the clutter signal's power by combining the images. The combination of smaller intensities (6 and 7 times iterations) produces the best pattern in this consideration.

https://doi.org/10.26376/GPR2018011

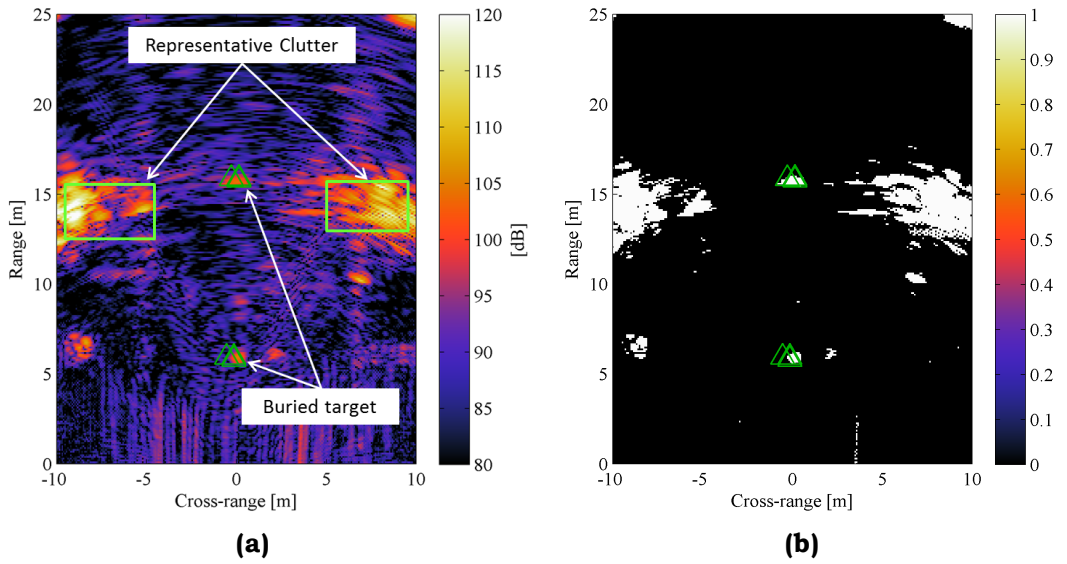

FIG. 3 – L-band VV pol result: **(a)** SAR image [15]; **(b)** Binary mask image for fundamental part. (Δ : True buried target position)

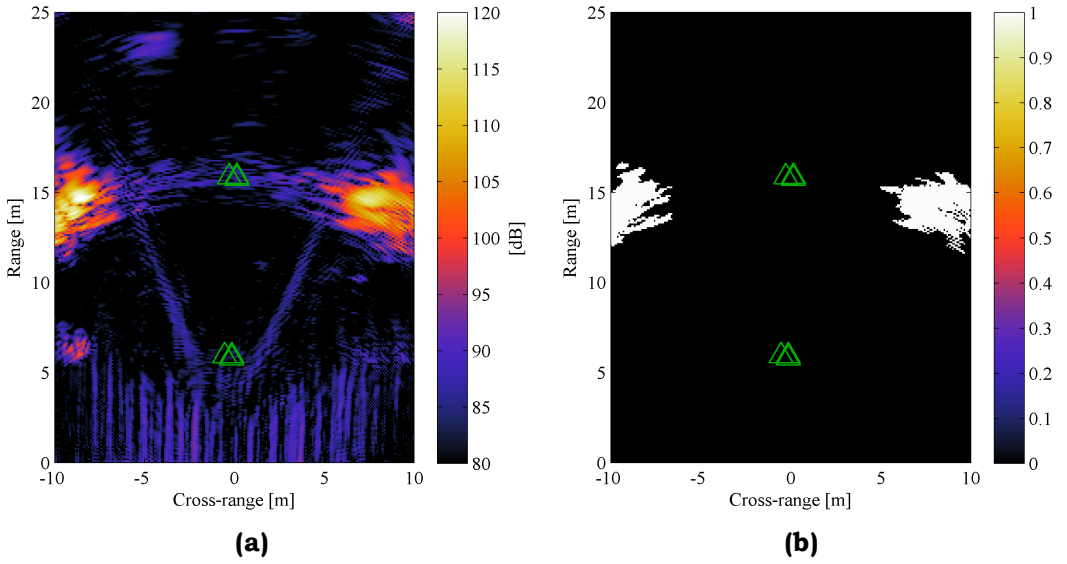

FIG. 4 – L-band VH pol result: **(a)** SAR image; **(b)** Binary mask image for fundamental part. (Δ : True buried target position)

https://doi.org/10.26376/GPR2018011

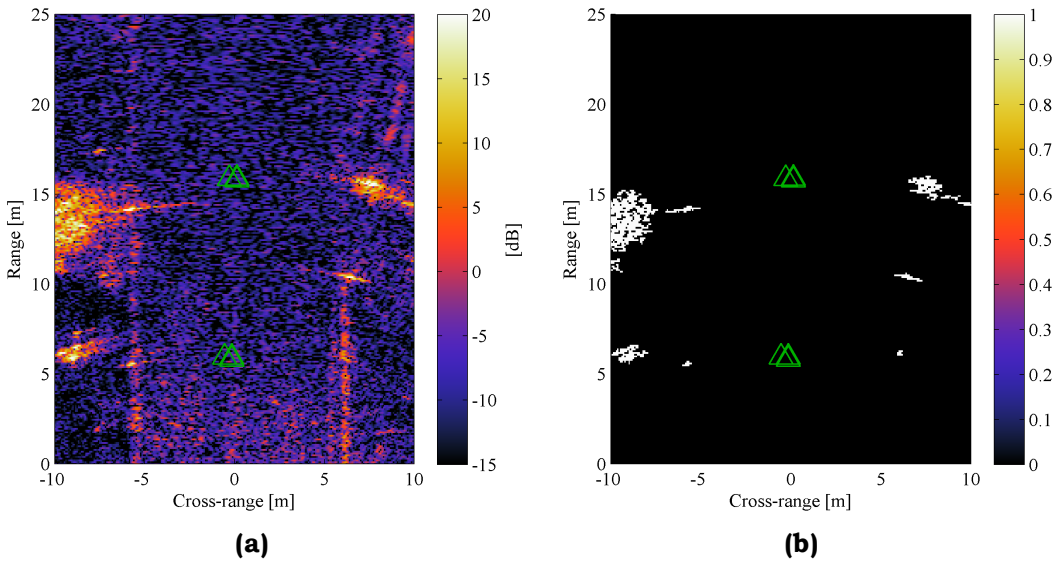

FIG. 5 – X-band result: **(a)** SAR image; **(b)** Binary mask image for fundamental part (Δ : True buried target position.)

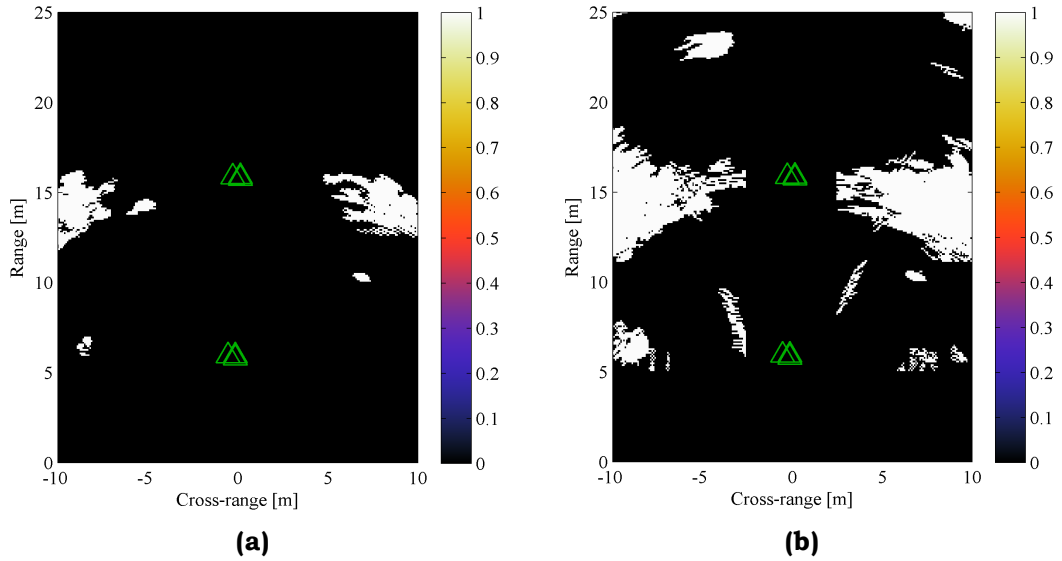

FIG. 6 – Mixed binary mask: **(a)** Fundamental part; **(b)** Extended part. (Δ : True buried target position)

https://doi.org/10.26376/GPR2018011

TABLE II - COMBINATION PATTERN FOR AVERAGE.

Combination index #	**Output images**
0	Original SAR image
1	Iterations 1 and 2 times
2	Iterations 2 and 3 times
3	Iterations 3 and 4 times
4	Iterations 4 and 5 times
5	Iterations 5 and 6 times
6	Iterations 6 and 7 times

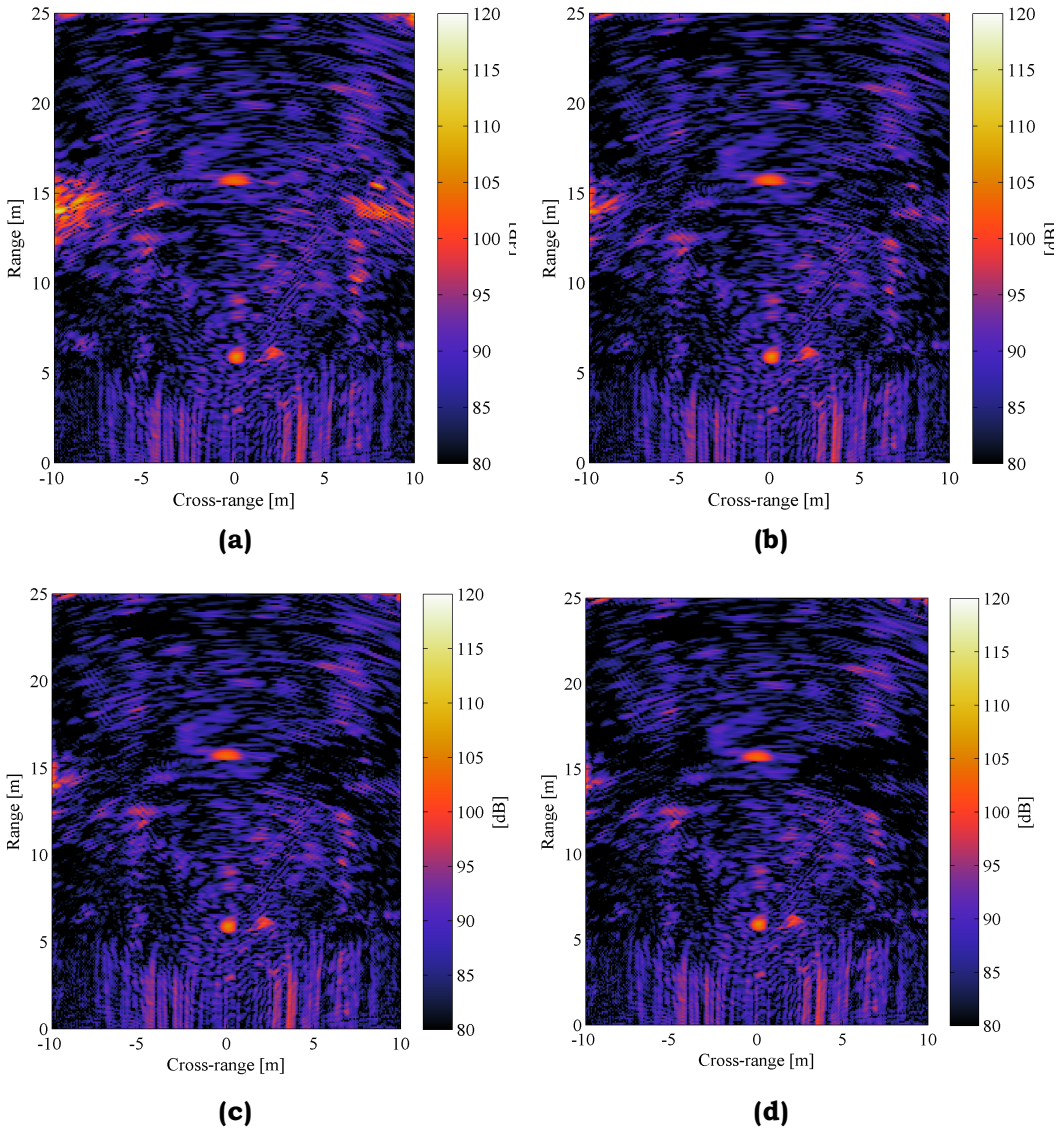

FIG. 7 – Averaging images to reduce clutter: **(a)** #1; **(b)** #3; **(c)** #4; **(d)** #6. Targets are in the same position as in Figure 3(a).

https://doi.org/10.26376/GPR2018011

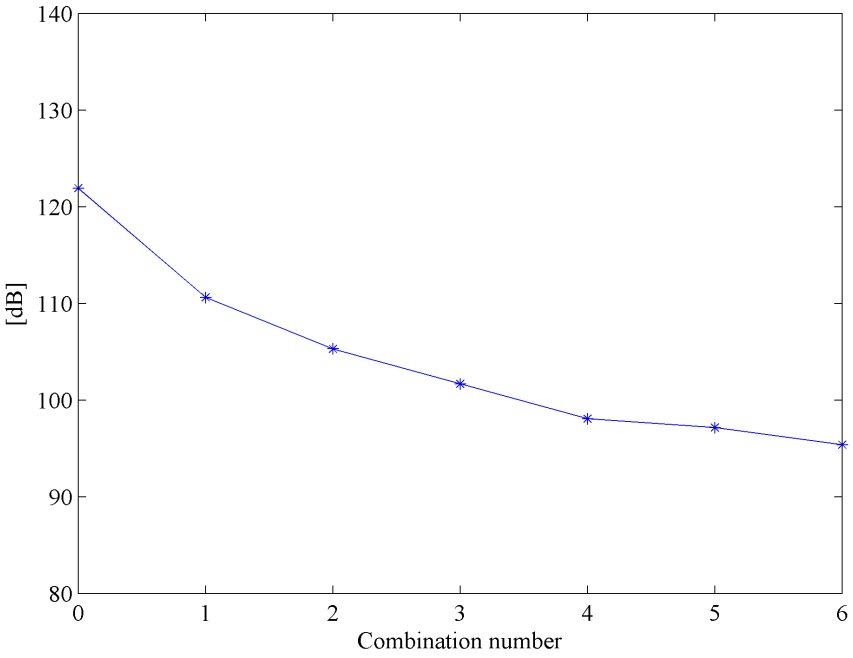

(a)

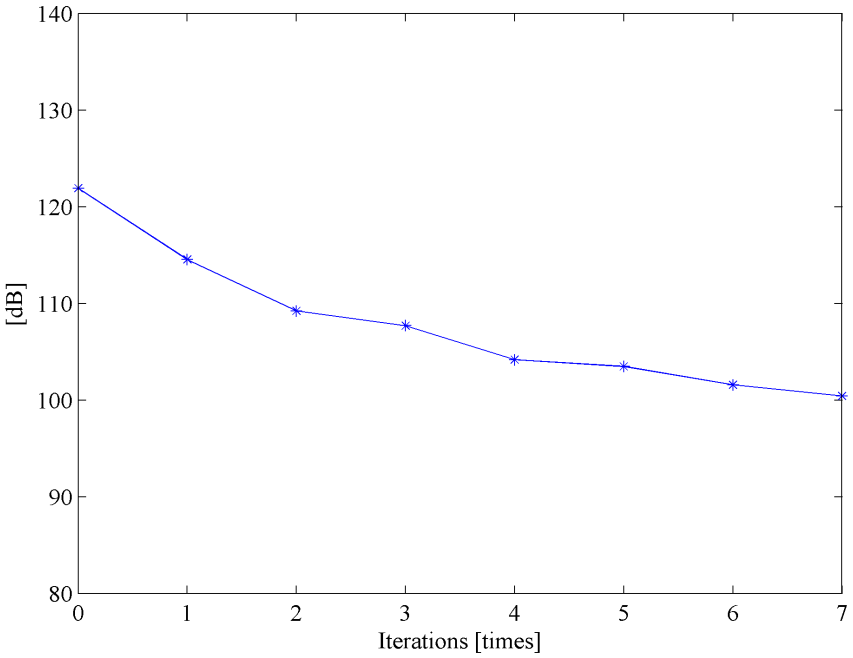

(b)

FIG. 8 – Clutter signal as a function of iteration number and in combination: **(a)** Without averaging; **(b)** With averaging, as indicated by index number.

https://doi.org/10.26376/GPR2018011

4. Evaluation

The proposed method for FLGPR system is validated on two arid test lanes, with metal targets buried at different depths.

The ROC curve quantifies detection performance, presenting the relationship between the probability detection (P_d) and the false alarm rate (FAR). FAR is calculated as the number of false alarms per the total sensing area, and the total sensing area is the accumulated detection area for all measured frames. In this paper, the detection area is set with cross-range span -7 ~ 7 m and down track span 5 ~10 m. The halo area for evaluation of the detected target is a circle centred at the ground truth target, with a diameter of 1 m. A signal is positively declared when it is over the threshold and located within the halo.

The resulting ROC curves in the two lanes are presented in Figure 9. They show the results for the original SAR imaging and the model-based clutter suppression processed SAR image. Based on these figures, the false alarm rate is significantly improved by using the proposed model-based clutter suppression method.

5. Conclusion

An advanced model-based clutter suppression method, which suppresses clutter signals in FLGPR SAR imaging, was presented. The method applies a mixed binary mask created from L-band VV, VH pol image, and X-band SAR images. The effect of the clutter suppression method has been validated with the measurement data. The result of the test lane shows that the method significantly reduces the false alarm rate.

Ackwnowledgement

This paper is supported by United States Army, Communications-Electronics Research, Development and Engineering Center, Night Vision and Electronic Sensors Directorate (W909MY12C0028).

https://doi.org/10.26376/GPR2018011

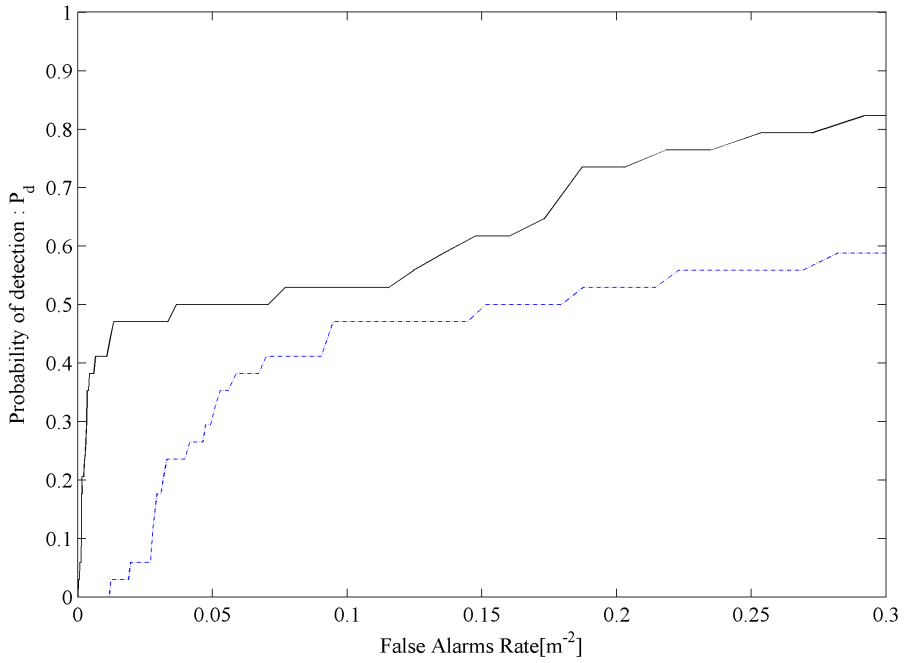

(a)

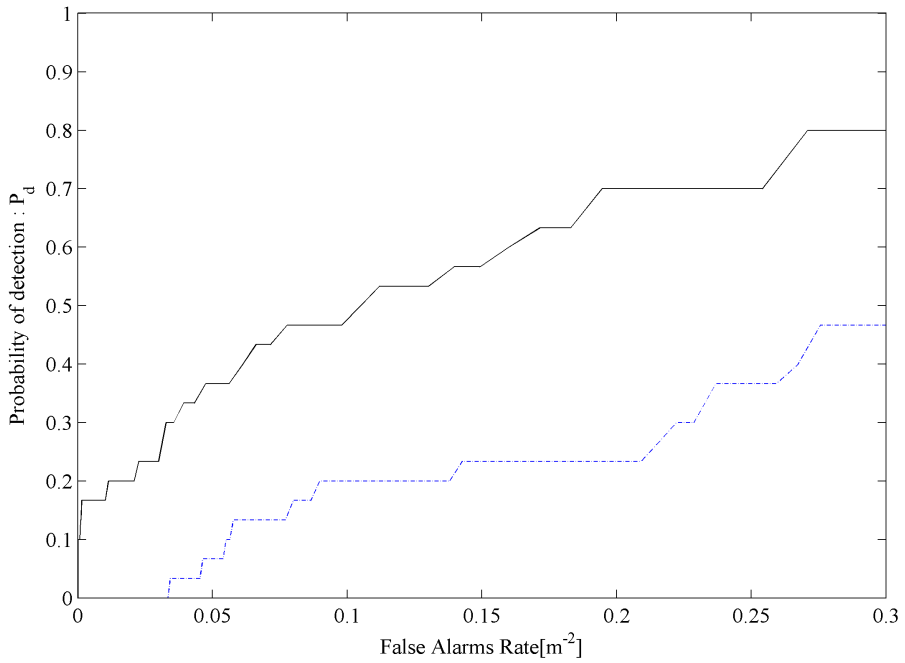

(b)

Fig. 9 – ROC results: **(a)** Lane A; **(b)** Lane B. (--------, With processing; ———, Without processing)

https://doi.org/10.26376/GPR2018011

REFERENCES

[1] D. J. Daniels, "A review of GPR for landmine detection," Sensing and Imaging: An international journal, vol. 7, no. 3, pp. 90–123, September 2006, doi: 10.1007/s11220-006-0024-5.

[2] N. Playle, D. M. Port, R. Rutherford, I. A. Burch, and R. Almond, "Infrared polarization sensor for forward-looking mine detection," 2002 AeroSense conference of the International Society for Optics and Photonics, Orlando, FL, US – Proceedings of the SPIE, vol. 4742: Detection and Remediation Technologies for Mines and Minelike Targets VII, August 2002, pp. 11–18, doi: 10.1117/12.479086.

[3] K. P. Gurton and M. Felton, "Remote detection of buried land-mines and ieds using lwir polarimetric imaging," Optics Express, vol. 20, no. 20, pp. 22344–22359, September 2012, doi: 10.1364/OE.20.022344.

[4] R. D. Costley, J. M. Sabatier, and N. Xiang, "Forward-looking acoustic mine detection system," 2001 Aerospace/Defense Sensing, Simulation, and Controls conference of the International Society for Optics and Photonics, Orlando, FL, US – Proceedings of the SPIE, vol. 4394: Detection and Remediation Technologies for Mines and Minelike Targets VI, October 2001, pp. 617–626, doi: 10.1117/ 12.445514.

[5] J. Moros, F. J. Fortes, J. M. Vadillo, and J. J. Laserna, "Libs detection of explosives in traces," Chapter 13 in Laser-Induced Breakdown Spectroscopy, Springer Series in Optical Sciences, vol. 182, pp. 349–376, 2014, ISBN 9783642450846.

[6] G. Liu, Y. Wang, J. Li, and M. R. Bradley, "SAR imaging for a forward-looking GPR system," 2003 Aerospace/Defense Sensing, Simulation, and Controls conference of the International Society for Optics and Photonics, Orlando, FL, US – Proceedings of the SPIE, vol. 5089: Detection and Remediation Technologies for Mines and Minelike Targets VIII, September 2003, pp. 322–333, doi: 10.1117/12.485687.

[7] T. Ton, D. Wong, and M. Soumekh, "Alaric forward-looking ground penetrating radar system with standoff capability," Proceedings of the 2010 IEEE International Conference on Wireless Information Technology and Systems, 28 August – 3 September 2010, Honolulu, HI, US, pp. 1–4, doi: 10.1109/ ICWITS.2010.5611911.

[8] T. Wang, J. M. Keller, P. D. Gader, and O. Sjahputera, "Frequency subband processing and feature analysis of forward-looking ground-penetrating radar signals for land-mine detection," IEEE Transactions on Geoscience and Remote Sensing, vol. 45, no. 3, pp. 718–729, February 2007, doi: 10.1109/TGRS.2006.888142.

https://doi.org/10.26376/GPR2018011

[9] T. C. Havens, K. Ho, J. Farrell, J. M. Keller, M. Popescu, T. T. Ton, D. C. Wong, and M. Soumekh, "Locally adaptive detection algorithm for forward-looking ground-penetrating radar," 2010 Defense, Security, and Sensing conference of the International Society for Optics and Photonics, Orlando, FL, US – Proceedings of the SPIE, vol. 7664: Detection and Sensing of Mines, Explosive Objects, and Obscured Targets XV, April 2010, Article ID 76642E, 9 pp., doi: 10.1117/12.851512.

[10] T. C. Havens, K. Stone, D. T. Anderson, J. M. Keller, K. Ho, T. T. Ton, D. C. Wong, and M. Soumekh, "Multiple kernel learning for explosive hazard detection in forward-looking ground-penetrating radar," 2012 Defense, Security, and Sensing conference of the International Society for Optics and Photonics, Baltimore, MD, US – Proceedings of the SPIE, vol. 8357: Detection and Sensing of Mines, Explosive Objects, and Obscured Targets XVII, May 2012, Article ID 83571D, 15 pp, doi: 10.1117/12.920482.

[11] D. Anderson, J. M. Keller, and O. Sjahputera, "Algorithm fusion in forward-looking long-wave infrared imagery for buried explosive hazard detection," 2011 Defense, Security and Sensing symposium of the International Society for Optics and Photonics, Orlando, FL, US – Proceedings of the SPIE, vol. 8017: Detection and Sensing of Mines, Explosive Objects, and Obscured Targets XVI, May 2011, Article ID 801722, doi: 10.1117/12.884600.

[12] K. Stone, J. Keller, K. Ho, M. Busch, and P. Gader, "On the registration of FLGPR and IR data for a forward-looking landmine detection system and its use in eliminating FLGPR false alarms," 2008 Defense, Security and Sensing symposium of the International Society for Optics and Photonics, Orlando, FL, US – Proceedings of the SPIE, vol. 6953: Detection and Sensing of Mines, Explosive Objects, and Obscured Targets XIII, April 2008, Article ID 695314, 12 pp. doi: 10.1117/12.782238.

[13] T. C. Havens, C. J. Spain, K. Ho, J. M. Keller, T. T. Ton, D. C. Wong, and M. Soumekh, "Improved detection and false alarm rejection using FLGPR and color imagery in a forward-looking system," in 2010 Defense, Security and Sensing symposium of the International Society for Optics and Photonics, Orlando, FL, US – Proceedings of the SPIE, vol. 7664: Detection and Sensing of Mines, Explosive Objects, and Obscured Targets XV, April 2010, Article ID 76641U, 12 pp., doi: 10.1117/12.852274.

[14] B. Gonzalez-Valdes, Y. Alvarez, J. A. Martinez-Lorenzo, F. Las-Heras, and C. M. Rappaport, "On the combination of SAR and model based techniques for high-resolution real-time two-dimensional reconstruction," IEEE Transactions on Antennas and Propagation, vol. 62, no. 10, pp. 5180–5189, October 2014, doi: 10.1109/TAP.2014.2346203.

https://doi.org/10.26376/GPR2018011

[15] Y. Fuse, B. Gonzalez-Valdes, J. A. Martinez-Lorenzo, and C. M. Rappaport, “Advanced SAR imaging methods for forward-looking ground penetrating radar,” Proceedings of the 10th European Conference on Antennas and Propagation (EuCAP 2016), Davos, Switzerland, 10–15 April 2016, pp. 1–4, doi: 10.1109/EuCAP.2016.7481192.

https://doi.org/10.26376/GPR2018011

Ground Penetrating Radar
The first peer-reviewed scientific journal dedicated to GPR

FALSE ALARM REDUCTION BY TARGET TRACKING FOR FORWARD LOOKING GROUND PENETRATING RADAR

YUKINORI FUSE[1], MASOUD ROSTAMI[1],
BORJA GONZALEZ-VALDES[2] & CAREY M. RAPPAPORT[1]

[1] DEPARTMENT OF ELECTRICAL AND COMPUTER ENGINEERING, NORTHEASTERN UNIVERSITY, BOSTON, MASSACHUSETTS, UNITED STATES OF AMERICA – YFUSE@ECE.NEU.EDU; MROSTAMI@ECE.NEU.EDU; RAPPAPORT@COE.NEU.EDU

[2] UNIVERSITY OF VIGO, VIGO, SPAIN – BGVALDES@COM.UVIGO.ES

ABSTRACT

An algorithm based on tracking stationary buried objects with advancing platform views is shown to reduce false alarms for Forward-Looking Ground Penetrating Radar (FLGPR). First, the Synthetic Aperture Radar (SAR) processed image is cleaned using a model-based clutter suppression method by applying masks to suppress the clutter signals. The mask is generated by L-band VV (vertical transmitting, vertical receiving), and VH (vertical transmitting, horizontal receiving) polarizations and X-band VV polarization SAR image results. Second, target tracking is applied to the clutter suppressed SAR image. These images are compared based on the system positions and the possible clutter signals are eliminated. The total detection performance is evaluated by a Receiver Operating Characteristic (ROC) curve with measurement data. The proposed method achieves significant reduction of the false alarm rate and improves the detection performance of the FLGPR system.

KEYWORDS: Imaging system; Synthetic Aperture Radar (SAR); Forward-Looking Ground Penetrating Radar (FLGPR).

1. INTRODUCTION

Buried explosive threats such as mines have been a problem for decades. Especially Improvised Explosive Devices (IEDs) are a significant problem and they are explosive devices assembled with conventional military weapon such as mines and projectiles and the detonating mechanism. Some types of sensors such as Ground Penetrating Radar (GPR), infrared sensor [1], acoustic sensor [2], and metal detector [3] have been studied and developed for a long time. Forward-Looking GPR (FLGPR) [4, 5] is also one of the approaches to

https://doi.org/10.26376/GPR2018012

detect these treats and with the advantages of a safe stand-off distance between the sensor vehicle platform and the buried threat, and wide area coverage. FLGPR must distinguish between target of interest and clutter, due to scattering from the rough ground surface, rocks, objects above the surface like trees, bushes, and more. Model-based clutter suppression method for FLGPR has been proposed to solve this problem.

In this work, a false alarm reduction method based on a target tracking with a model-based clutter suppression method is presented. The method is validated with a measurement data set provided by the United States (US) Army, Communications-Electronics Research, Development and Engineering Center (CERDEC), Night Vision and Electronic Sensors Directorate (NVESD). The FLGPR is a dual wideband radar system, which uses the lower frequency L-band (0.75~3.2 GHz) radar to sense subsurface objects, and the higher frequency X-band (8~12 GHz) radar to sense primarily the on-ground and above-ground scatterers. Model-based clutter suppression processing is able to clean the L-band Synthetic Aperture Radar (SAR) image using a mixture binary mask formed by L-band and X-band masks [6], with the binary mask covering just the clutter signals while excluding the buried target signals. The mask is applied to the L-band radar image and a new simulated response is generated. Primary clutter objects signals are subtracted from the original L-band signals, generating a clutter-suppressed SAR image with minimal reduction in buried target image intensity.

To reduce the false alarm rate further, a target tracking image processing method is proposed to supplement the model-based clutter suppression method. The tracking process is applied using SAR images at different Global Positioning System (GPS)-determined positions of the radar platform to track the buried target responses. This process is repeated for selected observation frames. Since grazing-incident refracted waves tend to be fairly independent of incident angle, underground objects tend to scatter similarly for most stand-off distances; and thus yield a consistent image, independent of platform position. This image consistency from the buried targets is a feature that is exploited to distinguish them from clutter objects.

https://doi.org/10.26376/GPR2018012

2. METHODOLOGY

This section explains the methodology of the false alarm reduction method. The system specification is described in Table I. The L-band radar has 8 transmitters and 8 receivers, and the X-band radar has 32 transmitters and 4 receivers. A GPS is mounted on the system so that the antenna positions are obtained at each system location. Therefore, reconstructed wideband array based images can be added together coherently with using multiple frames in the range direction to form the SAR image.

The target tracking method is applied after the model-based clutter suppression method [6]. Since the buried targets are static objects while the sensor system is moving forward, an estimated position can be derived from the position of the system at each observation frame. This position changes in the moving computational frame, corresponding to the movement of the vehicle between frames. The tracking procedure is divided into two main parts. The first part eliminates the possible false alarms by comparing the position of image peaks in different frames. In the second part, the tracking method is applied again to the positions declared in the first part to further eliminate false alarms. The procedure of the tracking method is described as:

[First part]

Step 1) Create the segments of the signals in a given image by choosing pixels above a certain threshold value in the current frame.
Step 2) Detect peaks of each segment in the image at the current frame number.
Step 3) Calculate the predicted position of each segment for the system positions from the next frames.
Step 4) Detect peaks of each segment in the next frame.
Step 5) Set the evaluation area based on the positions of Step 4 and compare to the estimated positions from Step 3.
Step 6) Decide and track using the results of Step 5.
Step 7) Repeat Steps 1 to 6, to identify additional possible targets.
Step 8) Declare the possible target positions in the first part.

https://doi.org/10.26376/GPR2018012

TABLE I – FLGPR SYSTEM.

	L-band radar	**X-band radar**
Antennas	8 transmitters, 8 receivers	32 transmitters, 4 receivers
Frequency bandwidth	0.75 GHz - 3.2 GHz	8.4GHz - 10.4 GHz

[Second part]

Step 9) Repeat Steps 1 to 8, discounting declared targets to track weaker signals and identify additional targets.

Step 10) Evaluate these results and declare the final target positions.

A series of images are used in this target tracking method to associate the positions of the peaks from frame to frame. The tracking method concept is presented in Figure 1, for $N + 1$ images. In this case, the front frame is frame #i and previous images from the past N platform positions have indexes from $i - N$ to #i. These can be used to estimate the position of the peak in the next frame image. The frame number "$i - N$" is the starting frame to obtain the result of frame #i. The SAR image is given by $I(x, y)$, and the peaks of the signals are calculated in the frame #$i - N$ as:

$$(p_{i-N}, q_{i-N}) = max[I_{i-N}(x, y)] \quad (1)$$

where (p_{i-N}, q_{i-N}) is the position within the regions at the front frame #$i - N$ of the image maximum. Since the vehicle mounted antenna platform is not necessarily moving in a straight line, it is important to re-register the images for every frame to ensure that the target responses from various frames overlap. The estimated position of the peaks can be calculated by the system position as:

$$p'_{i-N+1} = p_{i-N} - (X_{i-N+1} - X_{i-N}) \quad (2)$$

$$q'_{i-N+1} = q_{i-N} - (Y_{i-N+1} - Y_{i-N}) \quad (3)$$

where (p'_{i-N+1}, q'_{i-N+1}) is the estimated image maximum point of the region and (X_i, Y_i) is the i^{th} platform position. The next peak position in front frame #$i - N + 1$ is derived as:

https://doi.org/10.26376/GPR2018012

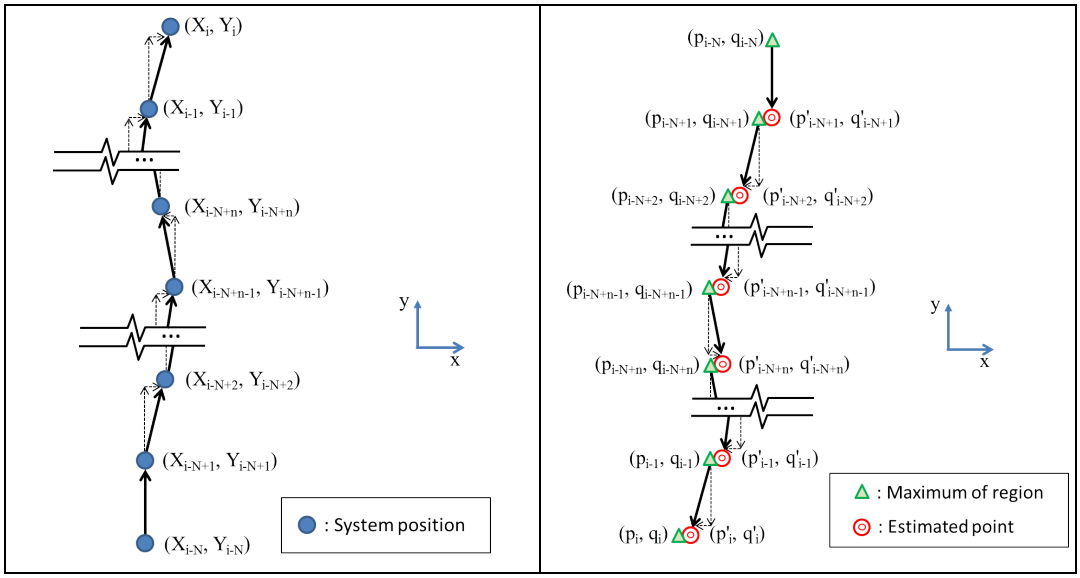

(a) **(b)**

FIG. 1 – Concept of the target tracking method: **(a)** System position in each frame. **(b)** Segment position in each frame.

$$(p_{i-N+1},\ q_{i-N+1}) = max\,[I_{i-N+1}\,(x,\ y)] \tag{4}$$

The comparison of the estimated position $(p'_{i-N+1},\ q'_{i-N+1})$ and (4) is made to decide whether the estimation position is sufficiently close; and if it is not close, that region is defined as clutter. This comparison is conducted for all discrete image maxima. The positions of the potential threats are used for calculating the next estimated position. The general estimation point in frame #n (n = 1, 2, ..., N) is presented as:

$$p'_{i-N+n} = p_{i-N+n+1} - (X_{i-N+n} - X_{i-N+n+1}) \tag{5}$$

$$q'_{i-N+n} = q_{i-N+n+1} - (Y_{i-N+n} - Y_{i-N+n+1}) \tag{6}$$

This procedure is repeated until the final comparison is made, $(p_i,\ q_i)$ and $(p'_i,\ q'_i)$. If the response persists for all frames, as shown in Figure 1(b), the region is declared a target candidate. A flowchart of this concept is given in Figure 2.

https://doi.org/10.26376/GPR2018012

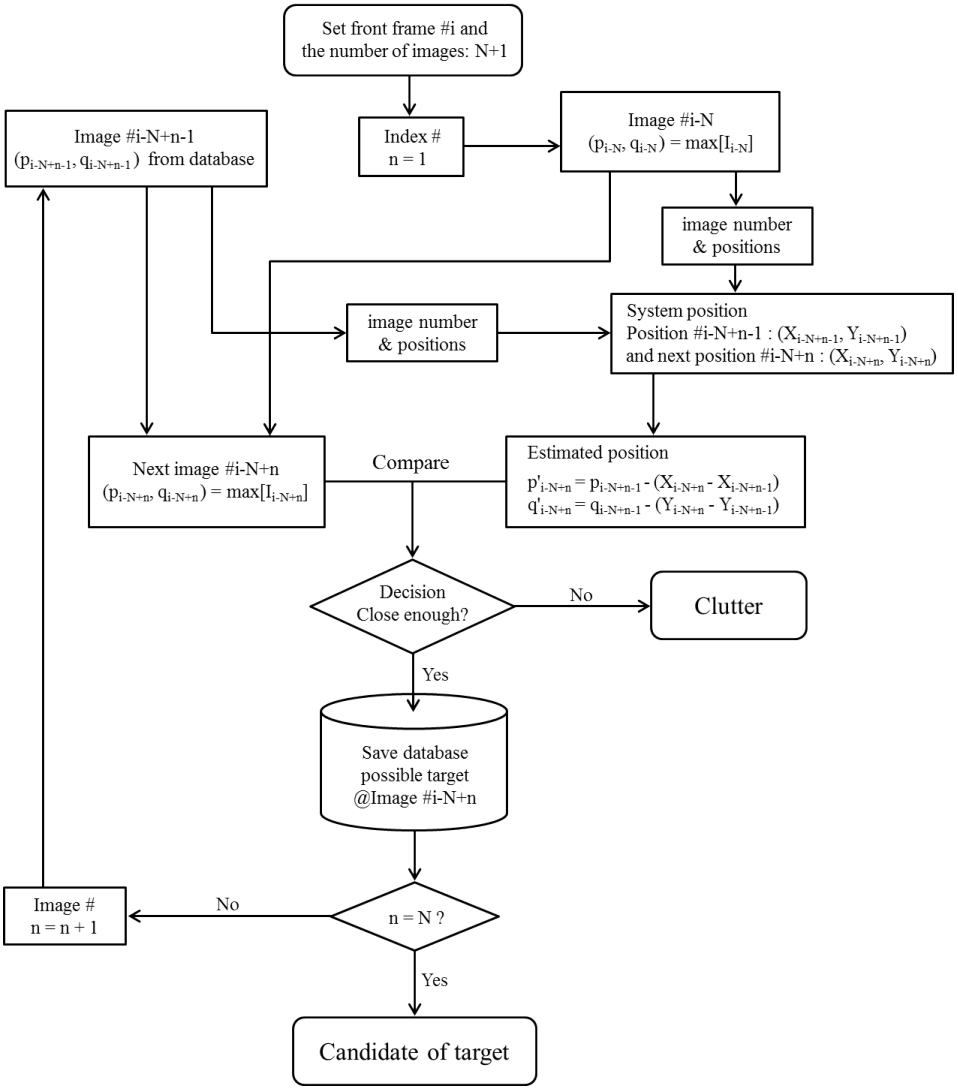

FIG. 2 – Flowchart of the target tracking method.

The second part of the method uses the same procedure as the first part, and it is applied to the output of the first part to further eliminate clutter signals. The positions of the possible target responses from the first part are compared to the positions of the vehicle, and if the responses are again declared, they have higher possibility of being target responses. Finally, the responses are declared as targets when they appear sequentially inside of the detection area. The parameters for the first and second parts are chosen from calibration runs in in the test lane.

https://doi.org/10.26376/GPR2018012

3. RESULTS

3.1 Pre-processing

An example of the original SAR image generated from field measured data is presented in Figure 3(a) [6], and the binary-mask clutter suppressed image is represented in Figure 3(b). Green triangle marker shows each true buried target (simulant explosives) position measured by GPS. In this paper, some buried targets are gathered in a group, but they are treated as one target. A noise reduction technique using a two-dimensional Gaussian smoothing filter [7] is applied to suppress small segments of the clutter signal in the image. Gaussian smoothing filters are widely used to reduce image noise and image details in digital image processing. The Gaussian filter is applied to the masking processed image scale in dB. An example of the pre-processing SAR image is shown in Figure 3(c). The Gaussian standard deviation parameter is selected as 0.8 to avoid eliminating the target signals. The number of segments in the masking processed image selected as non-target segments is 488, and the remaining number of non-target segments in the pre- processed image is 76. The potential false alarms are reduced by this pre-processing procedure.

3.2 First part of target tracking method

After applying image pre-processing, the peaks are considered as candidates for tracked responses. Examples of the pre-processed SAR image and the peak points are plotted with a black dot. As an example, for the first part of the tracking method, 28 sequential single frame step images are considered. Figure 4 represents the first comparison between images generated by the two approaches (Steps 1 - 6). The dot marks in Figure 4(a) are the peak points from the pre-processed image configuration. In Figure 4(b), the overlaid asterisk marks are the peak image points generated from the next antenna system position. The circle marks in Figure 4(c) are the peak positions of the next antenna positions. A test area is set based on the position of asterisk points, and when the pink circles are inside the test area, the positions are declared as target candidates. The evaluation area is arbitrarily set as 1.5 m wide in azimuth and 1.0 m in range. The red squares in Figure 4(d) show the declared positions. Comparing the predicted and newly-sensed images reduces some of the false alarms.

https://doi.org/10.26376/GPR2018012

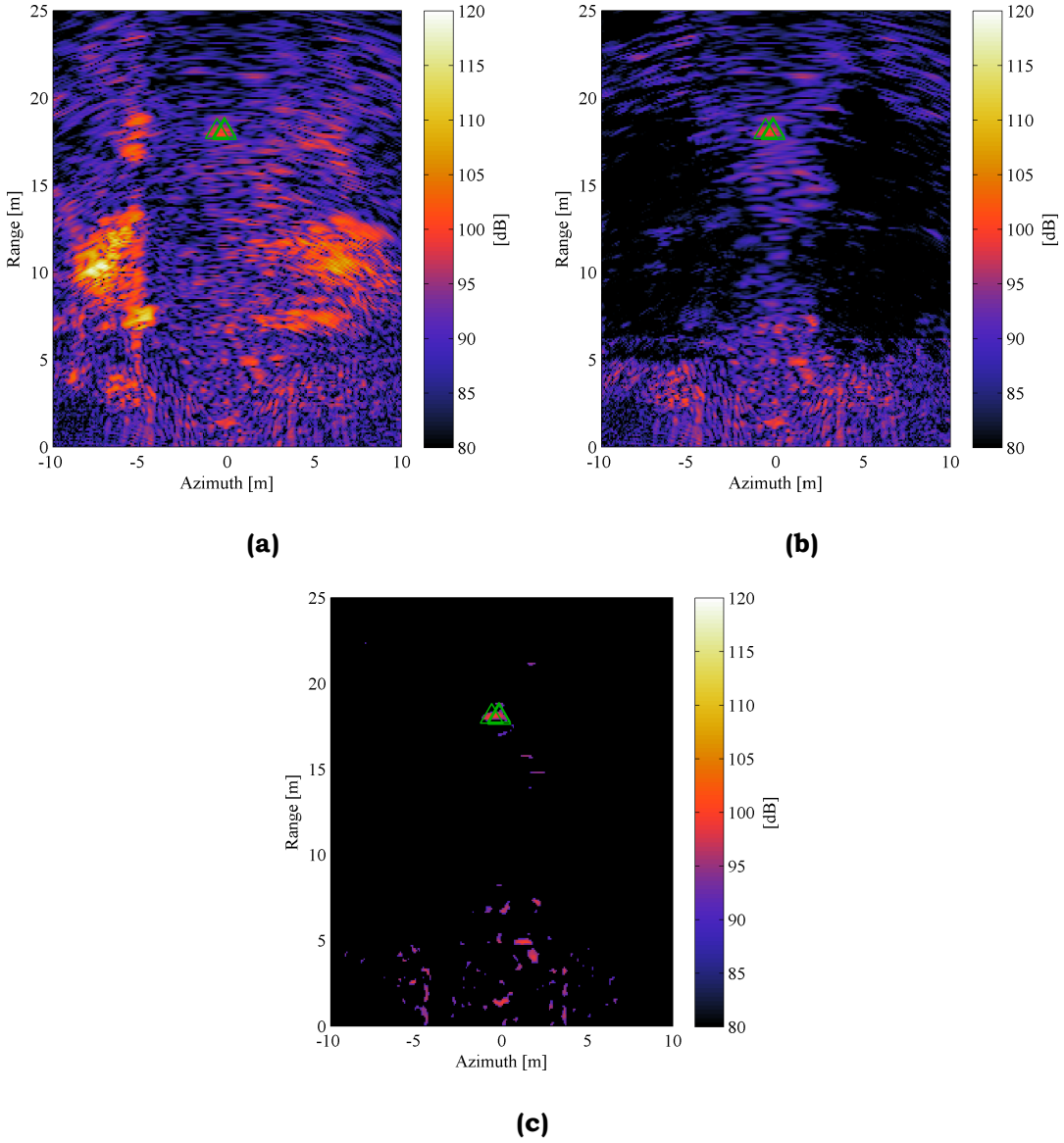

Fig. 3 – Model-based clutter suppression process image and pre-processed image. **(a)** Original SAR image. **(b)** Clutter suppression method SAR image. (c) Pre-processed SAR image. (Δ: True buried target position)

As an example, the procedure tested 28 images, with results presented in Figures 5–7. The declared points are plotted with white square boxes in the SAR image. After several iterations, the final declared potential target positions in the first step are shown in Figure 7. Figure 8 describes the relationship between the number of

https://doi.org/10.26376/GPR2018012

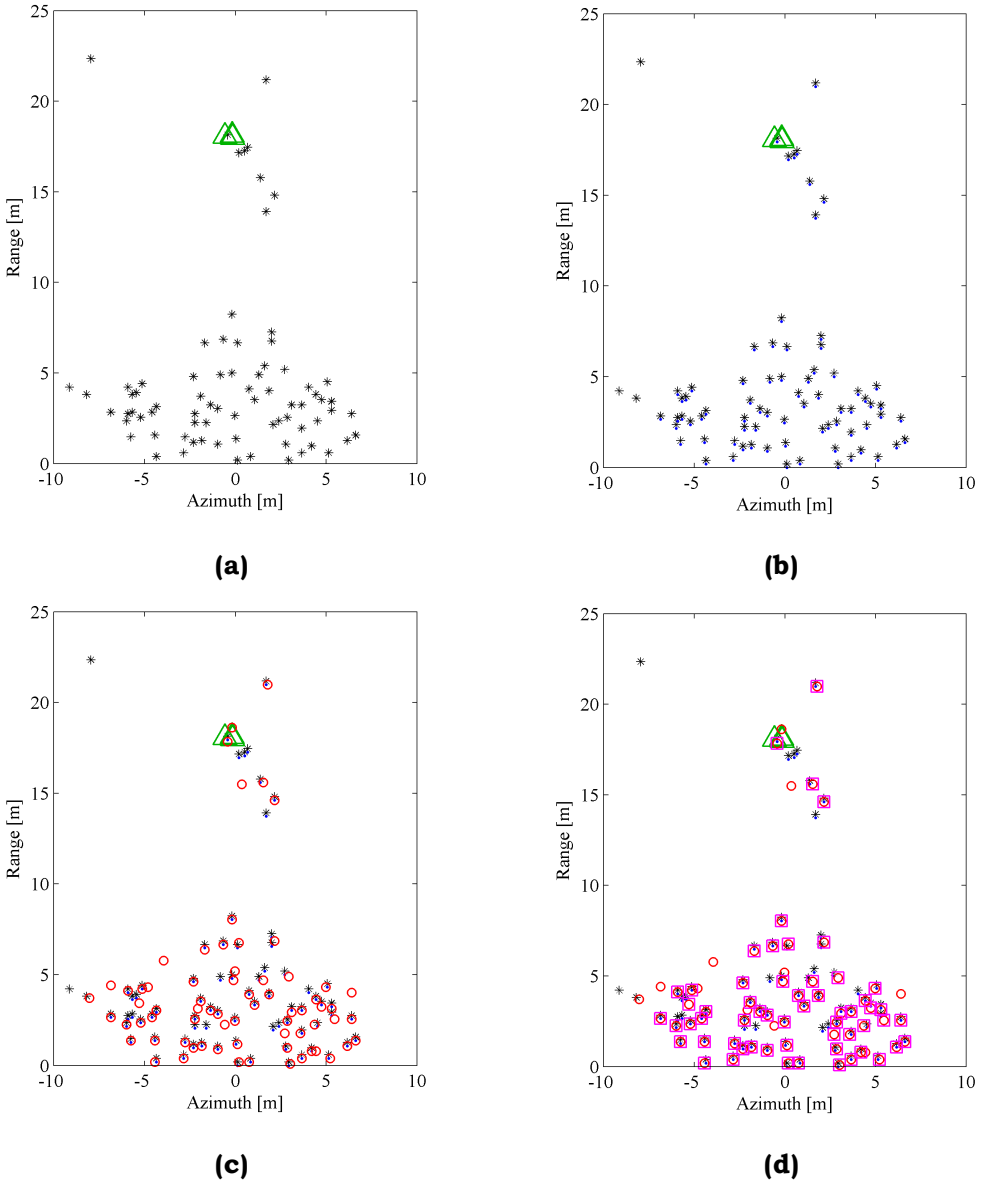

FIG. 4 – First part of the target tracking method, Steps 2-6. **(a)** Step 1. **(b)** Step 2. **(c)** Step 3. **(d)** Step 4 and 5. (· : Peak point in the current frame, ∗ : Estimated point of the next position, ◦ : Peak point in the next frame, □ : Declared point, Δ : True buried target position)

comparisons and the number of declared peaks. As presented in Figure 8, the number of declared peak points decreases by comparing the images frame by frame, from 77 at the 1st comparison to 7 at the 27th. The effectiveness of clutter reduction by the tracking method is confirmed.

https://doi.org/10.26376/GPR2018012

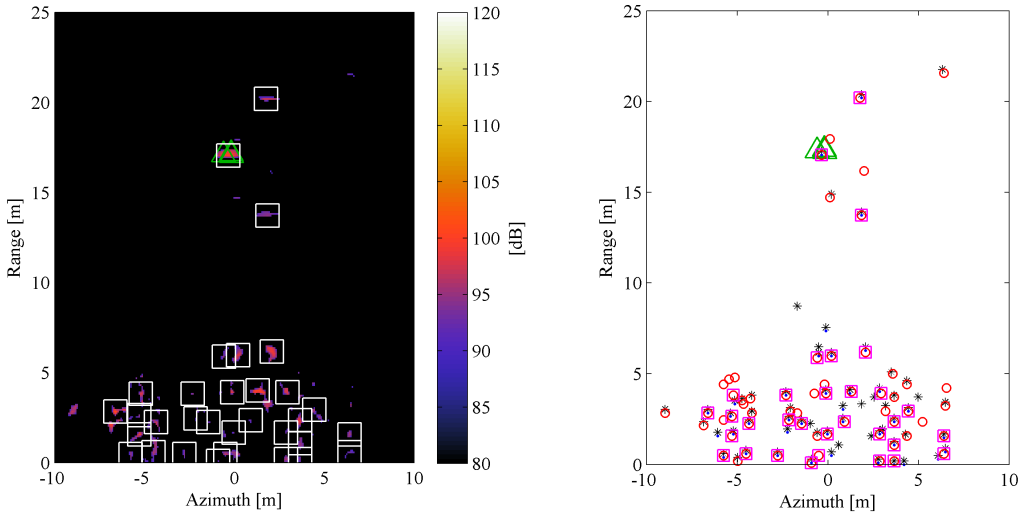

FIG. 5 – 5th comparison: **(a)** SAR image; **(b)** Peak plotted image. (∗ : Peak of current frame, · : prediction position, ◦ : Peak of next frame, □ : Declared point, Δ : True buried target position)

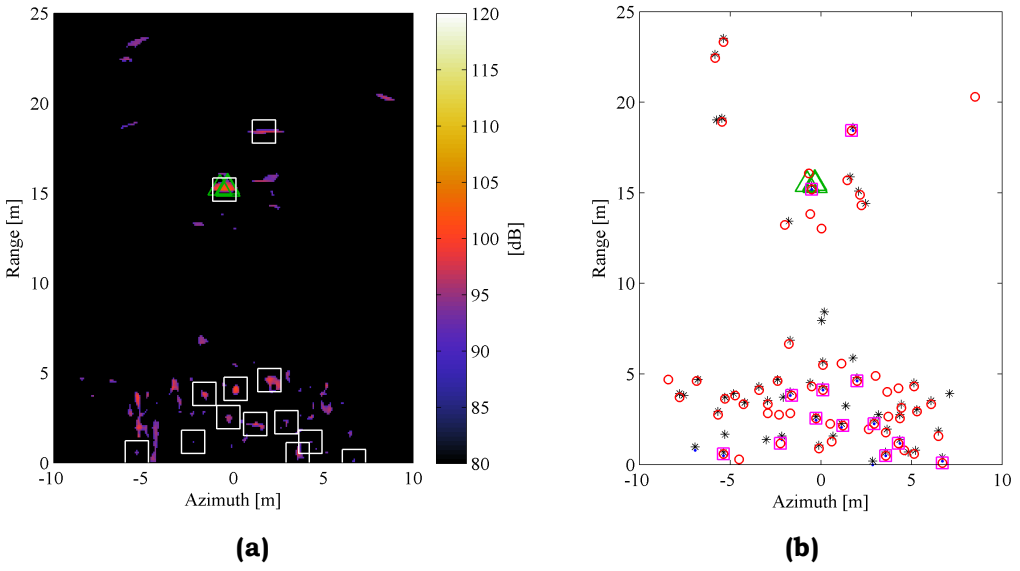

FIG. 6 – Same as in Fig. 5, 15th comparison.

https://doi.org/10.26376/GPR2018012

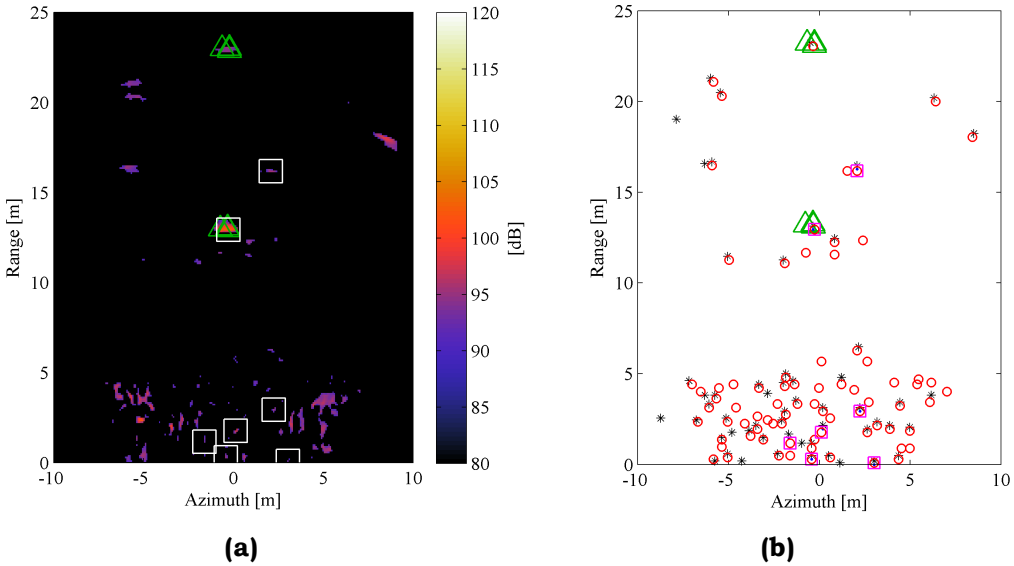

FIG. 7 – Same as in Fig. 5, 27th comparison.

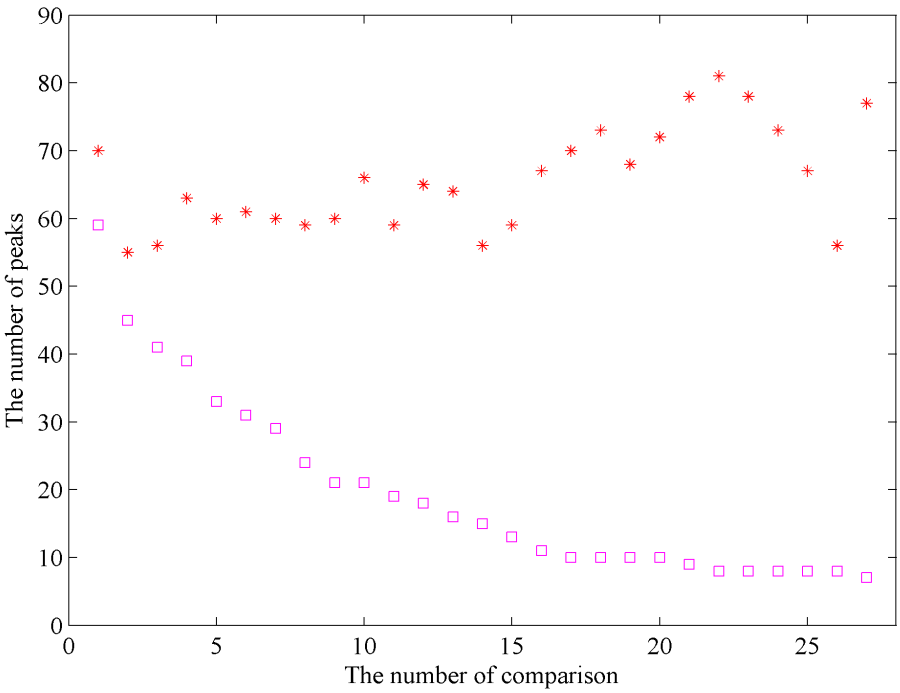

Fig. 8 – Relationship between the number of image comparison and the number of peaks (∗ : Peak point in the next frame, □ : Declared point)

https://doi.org/10.26376/GPR2018012

3.3 Second part of target tracking method

Second part of the target tracking method is based on the same concept as the first part. The positions of possible target responses from the first part are compared to the positions of the system, and if the signals are still declared, the responses have a higher probability of being target responses. Clutter responses are further eliminated, and the responses are confirmed as targets when the declared responses persist, appearing continuously within the detection area. Example results are presented in Figures 9–12. Each figure contains the results of the original SAR, the model-based clutter suppression processed image, and the target tracking processed image.

The potential target locations from the first part of the target tracking method are indicated with white markers, which are tracked during the second part of target tracking.

When a white marker appears continuously 7 times inside of the detection area, it is converted into a green marker, which indicates a higher probability of it being a target. An identification number is associated with each green square marker. When a green marker appears more than 3 times inside the detection area, it is changed into a square magenta marker and declared as a detected target. For example, the marker ID number 1 is located inside of the detection area, the green marker shown in Figure 11 is changed into the magenta marker as shown in Figure 12. This procedure is repeated continuously in every forward moving frame. The detection area for this particular sensing application is set as -7 m to 7 m in azimuth limit and 5 m to 10 m in range. The target is tracked simply and is effectively declared as detected by comparing the masking processed SAR images for various system positions.

4. Evaluations

The FLGPR target tracking method was extensively tested for multiple targets and a large variety of clutter on two lanes, lane A and lane B. In the test lanes, the buried targets were metal objects with different burial depths. Receiver Operating Characteristics (ROC) curves are used to evaluate the detection performance of the system, presenting the relationship between the probability detection (Pd) and the False Alarm Rate (FAR). FAR is calculated as the total number of false alarms per

https://doi.org/10.26376/GPR2018012

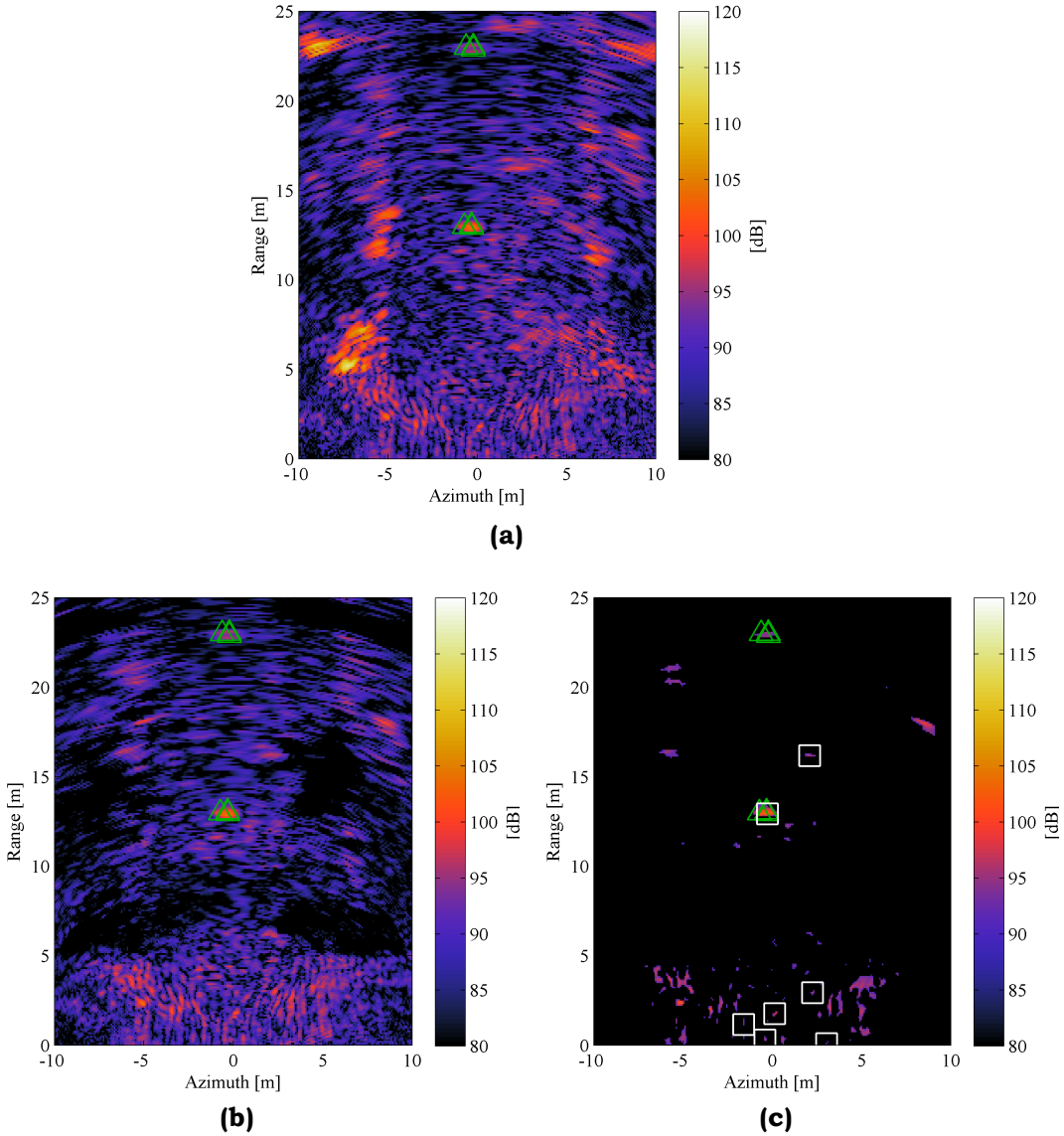

FIG. 9 – Second part of the target tracking method: Step 9 (1st output in second part): **(a)** Original SAR image; **(b)** Model-based clutter suppression SAR image; **(c)** Target tracking processed SAR image. (Δ: True buried target position, White square: First part tracked position).

the total sensing area, which is the accumulated detection area for all measured frames. The detection area is -7 m to 7 m in azimuth and 5 m to 10 m in range. The halo area for evaluation of the detected target is derived from the location of the ground truth target, with a diameter of 1 m. When a signal that rises above a specified threshold is located

https://doi.org/10.26376/GPR2018012

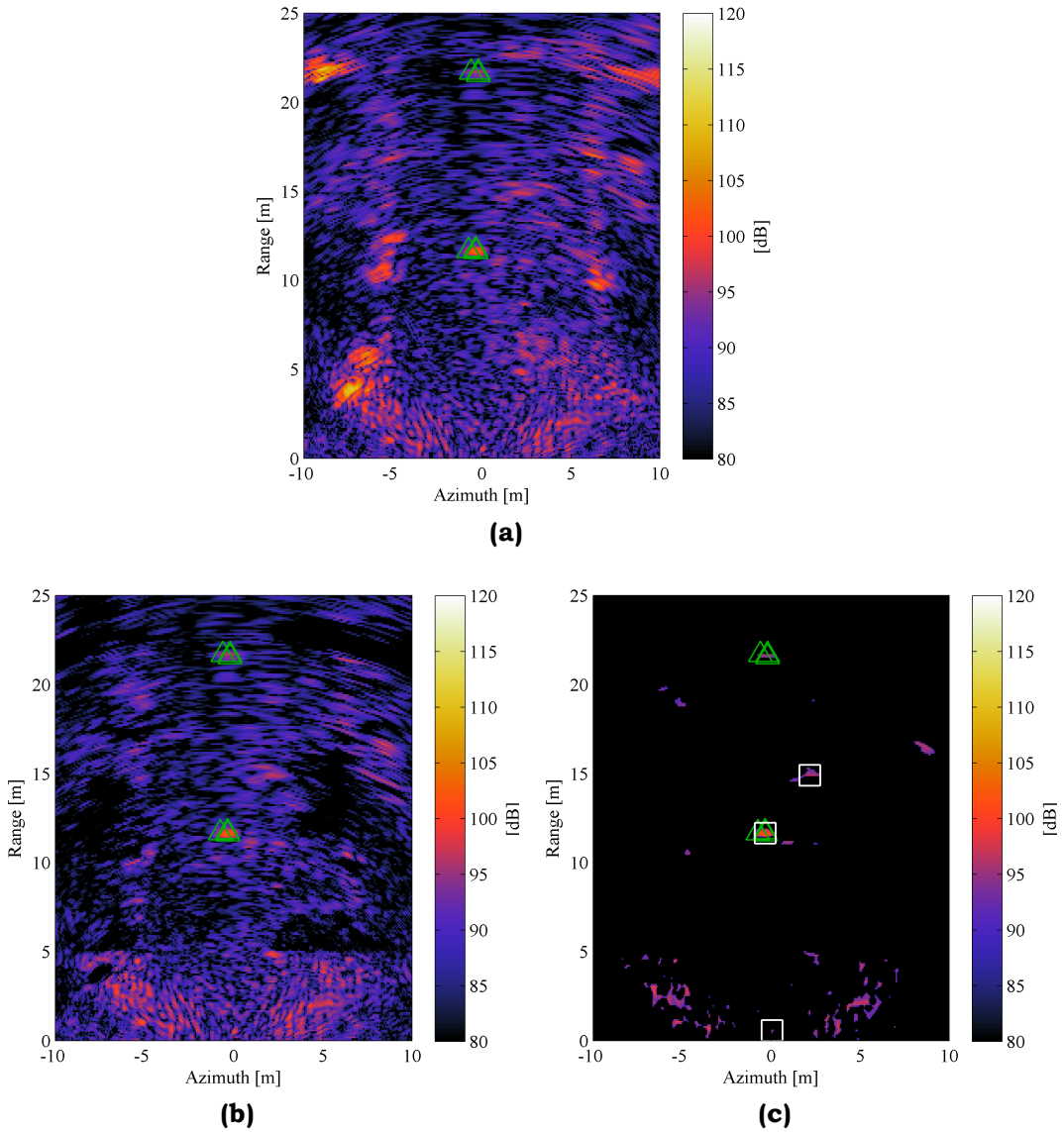

FIG. 10 – Same as in Fig. 9, for the 7th output in second part.

inside the halo, the signal is scored as a detected target. The resulting ROC in lanes A and B are presented in Figures 12 and 13. These figures present the detection results for the original SAR image, the model-based clutter suppression processed SAR image, and the target tracking processed image. Figures 12(b) and 13(b) show the performance details for target tracking. Based on these figures, the false alarm rate is reduced by almost 50 times using the proposed tracking method.

https://doi.org/10.26376/GPR2018012

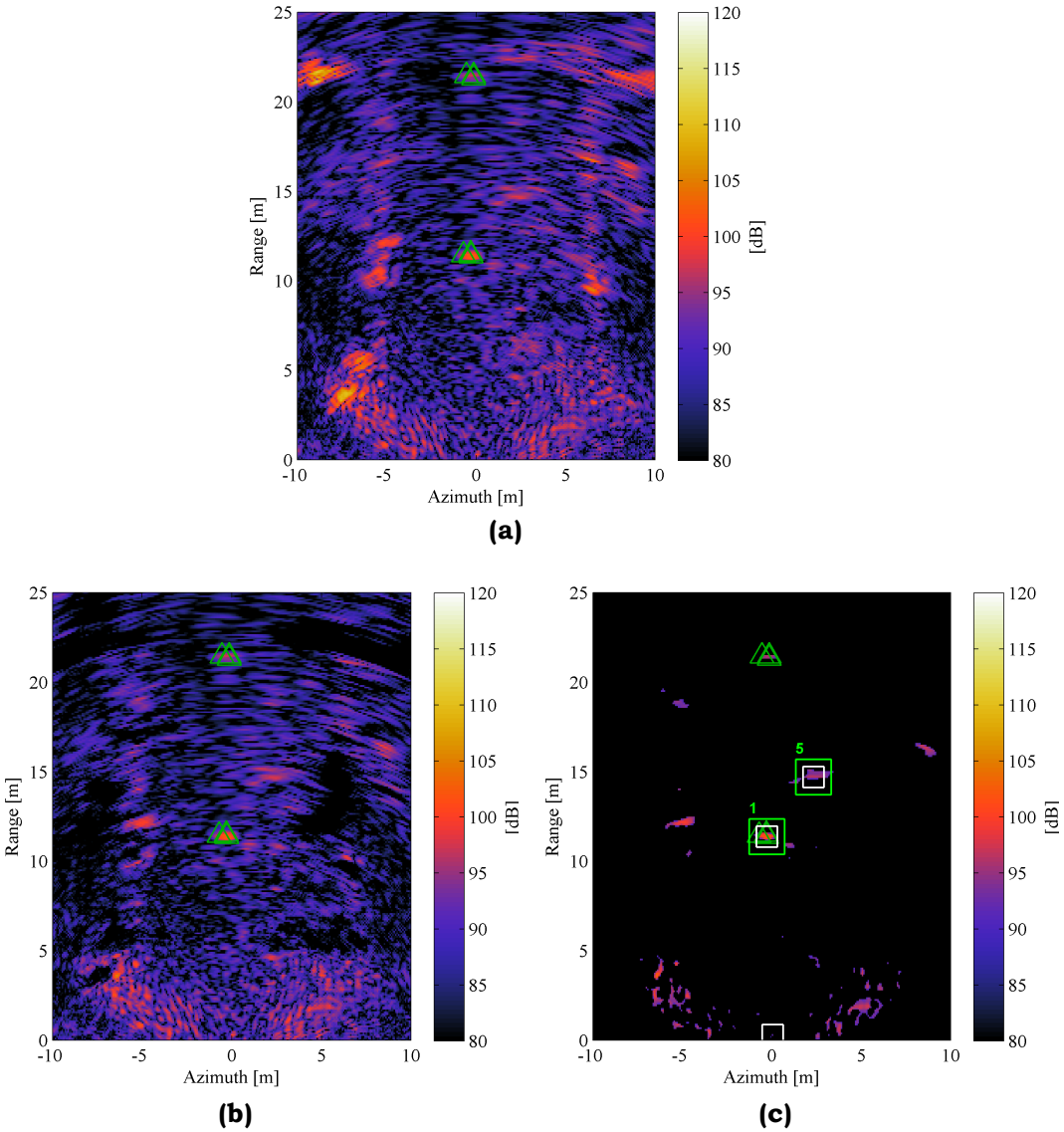

FIG. 11 – Same as in Fig. 9, for the 8th output in second part. Green squares represent the second part tracked position.

5. CONCLUSION

An advanced model-based target tracking clutter suppression process for the dual-band FLGPR was presented. The proposed method tracks and identifies buried targets by comparing the system position frame by frame and eliminating the more rapidly varying clutter images. The clutter suppression has been applied to the two lane data sets, and the

https://doi.org/10.26376/GPR2018012

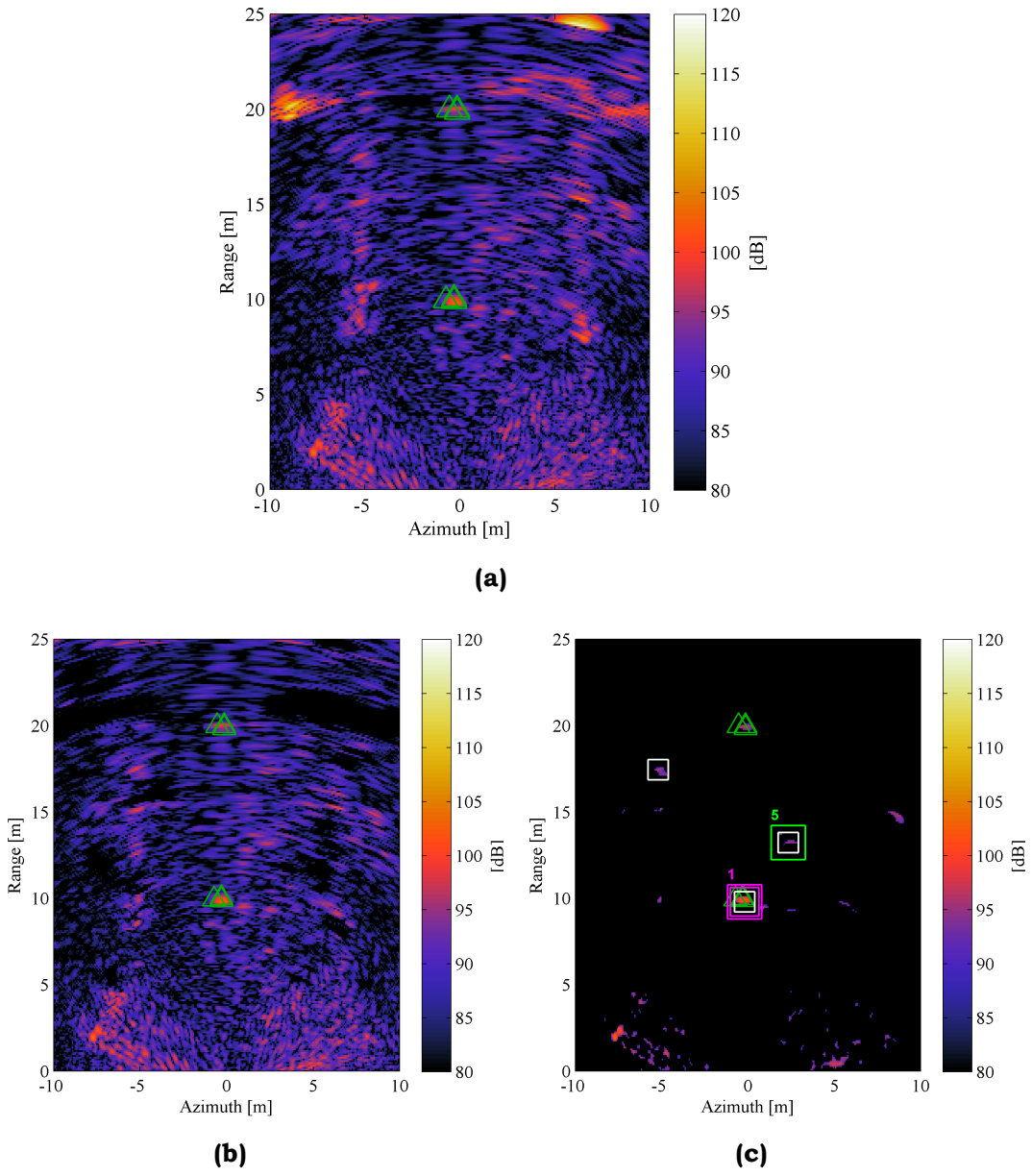

FIG. 12 – Second part of the target tracking method: Step 10 (15th output in second part): (a) Original SAR image; (b) Model-based clutter suppression SAR image; (c) Target tracking processed SAR image. (Δ: True buried target position, White square: First part tracked position, Green square: Second part tracked position, Magenta square: Detected target position).

https://doi.org/10.26376/GPR2018012

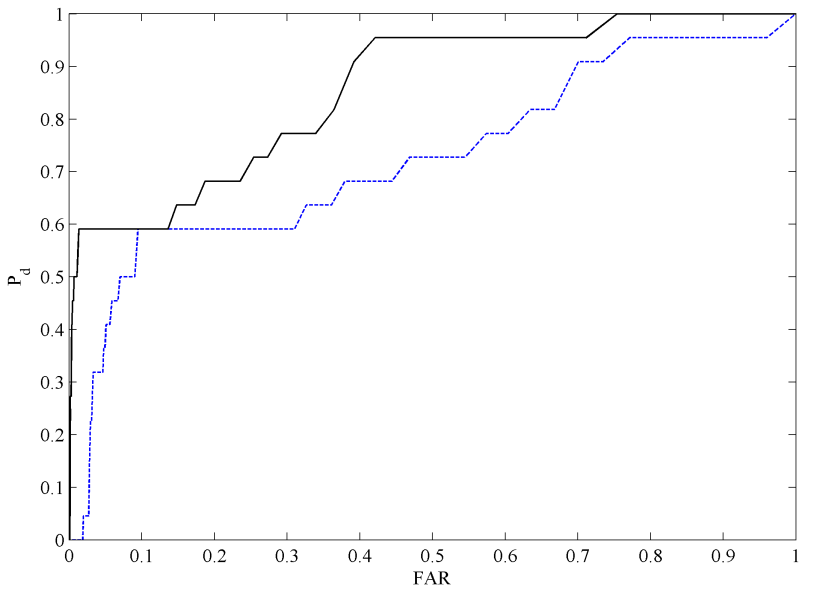

(a)

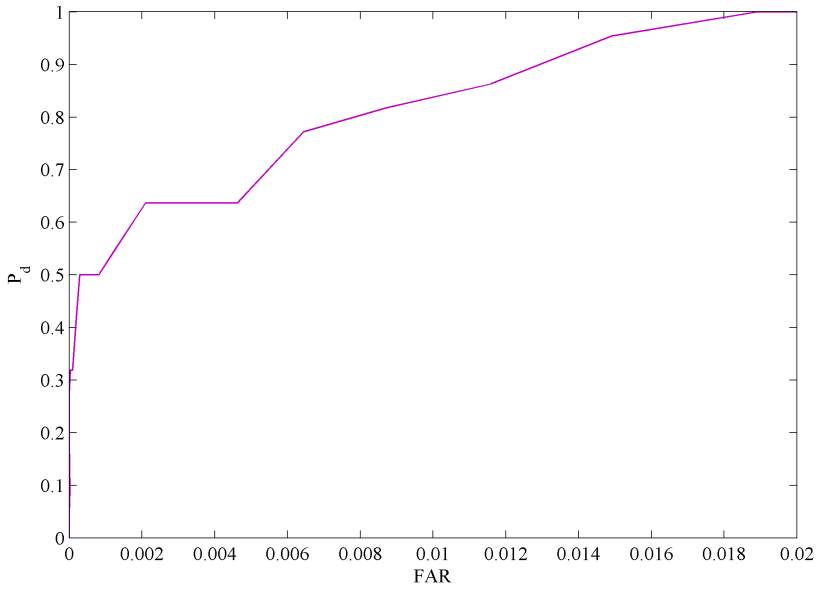

(b)

FIG. 13 – ROC curve of lane A with metal target: **(a)** No target tracking applied (--------: Original SAR image, ———: Model-based clutter suppression processed image); **(b)** With target tracking (note expanded FAR scale).

https://doi.org/10.26376/GPR2018012

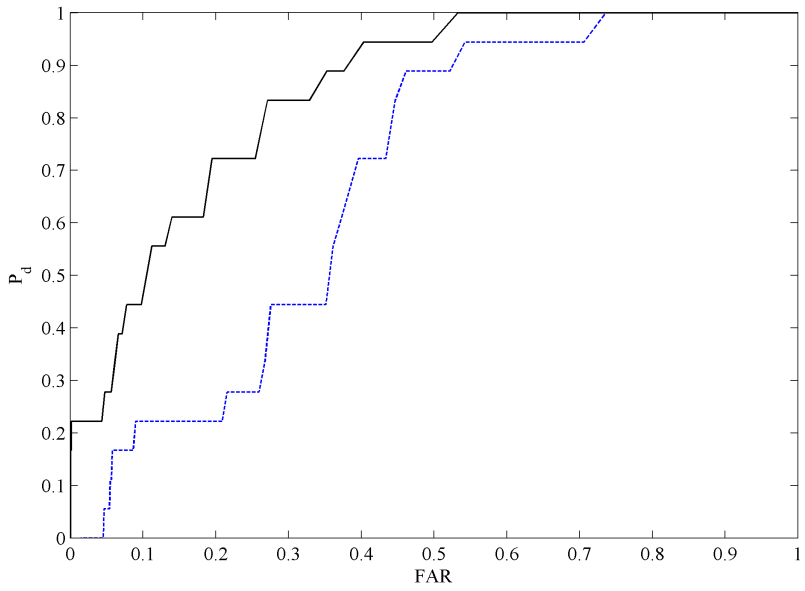

(a)

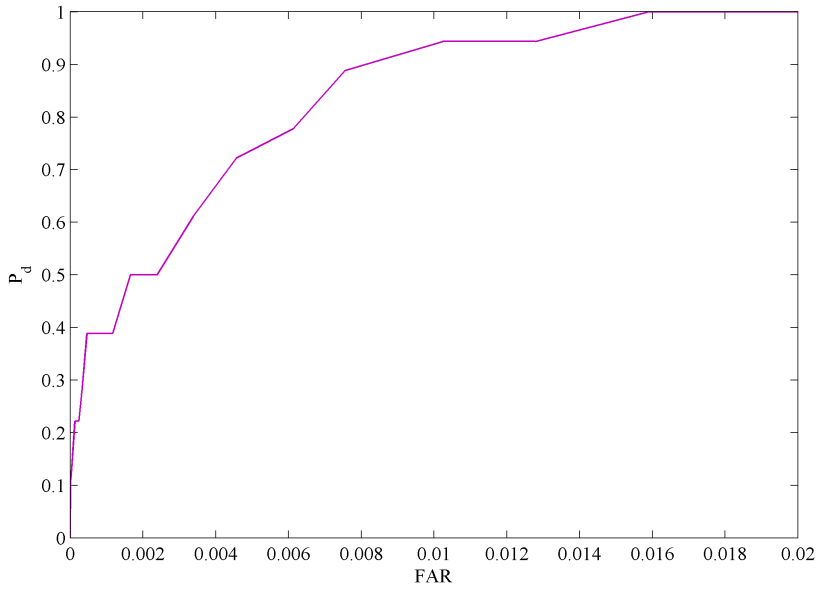

(b)

FIG. 14 – Same as in Fig. 13, for lane B.

https://doi.org/10.26376/GPR2018012

detection performance has been evaluated by using the ROC. One of the lanes is used as the test lane for optimizing the system threshold parameters and the other was used to test the algorithm. The result of test lane measurements also shows that the presented clutter reduction method is able to significantly improve the false alarm rate.

Ackwnowledgement

This work is supported by the U.S. Army CERDEC NVESD (W909MY12C0028).

References

[1] N. Playle, D. M. Port, R. Rutherford, I. A. Burch, and R. Almond, "Infrared polarization sensor for forward-looking mine detection," 2002 AeroSense conference of the International Society for Optics and Photonics, Orlando, FL, US – Proceedings of the SPIE, vol. 4742: Detection and Remediation Technologies for Mines and Minelike Targets VII, August 2002, pp. 11–18, doi: 10.1117/12.479086.

[2] B. J. Copenhaver, J. D. Gorhum, C. M. Slack, M. L. Barlett, T. G. Muir, and M. F. Hamilton, "Acoustic response of a buried landmine with a low grazing-angle source array, focused on the ground," Proceedings of Meetings on Acoustics, Acoustical Society of America, vol. 19, no. 1, 2 June 2013, Montreal, Canada, Article ID 045067, 6 pp., doi: 10.1121/1.4799604.

[3] M. Sato, J. Fujiwara, X. Feng, Z.-S. Zhou, and T. Kobayashi, "Development of a hand-held GPR MD sensor system (ALIS)," 2005 Defense and Security conference of the International Society for Optics and Photonics, Orlando, FL, US – Proceedings of the SPIE, vol. 5794: Detection and Remediation Technologies for Mines and Minelike Targets X, June 2005, pp. 1000–1007, doi: 10.1117/12.603213.

[4] L. Nguyen, "Signal and image processing algorithms for the US Army Research Laboratory: Ultra-wideband (UWB) Synchronous Impulse Reconstruction (SIRE) radar," Defence Technical Information Center (DTIC), Technical Report ARL-TR-4784, April 2009, 68 pp.

[5] K. Stone, J. Keller, K. Ho, M. Busch, and P. Gader, "On the registration of FLGPR and IR data for a forward-looking landmine detection system and its use in eliminating FLGPR false alarms," Proceedings of the Defense and Security Symposium of the International Society for Optics and Photonics – Proceedings of the SPIE, vol. 6953: Detection and Sensing of Mines, Explosive Objects, and Obscured Targets XIII, April 2008, Article ID 695314, 12 pp., doi: 10.1117/12.782238.

https://doi.org/10.26376/GPR2018012

[6] Y. Fuse, B. Gonzalez-Valdes, J. A. Martinez-Lorenzo, and C. M. Rappaport, "Advanced SAR imaging methods for forward-looking ground penetrating radar," Proceedings of the 10th European Conference on Antennas and Propagation (EuCAP 2016), Davos, Switzerland, 10–15 April 2016, pp. 1–4, doi: 10.1109/EuCAP.2016.7481192.

[7] R. Jain, R. Kasturi, and B. G. Schunck. "Machine vision," Publishing House: McGraw-Hill, Inc.; Book Series: "Computer Science;" New York, 1 May 2008; ISBN-13: 978-0070320185; ISBN-10: 0070320187; 549 pp.

https://doi.org/10.26376/GPR2018012

TABLE OF CONTENTS

NEWS & ANNOUNCEMENTS

Special Issue – Call for papers
SpliTech 2018 Workshop on the Applications of Ground Penetrating Radar

This *Ground Penetrating Radar* Special Issue will be a collection of extended papers resuming contributions presented during the scientific workshop entitled 'Applications of Ground Penetrating Radar and related Science Management aspects' successfully held in Split (Croatia), on 27-29 June 2018, in the framework of the 3rd International Conference on Smart and Sustainable Technologies (SpliTech 2018, 2018.splitech.org).

Special Issue Topics:
– Applications of GPR in civil engineering, archaeology, cultural heritage
– Science management aspects in GPR research
– Innovative GPR equipment, testing and optimization
– Electromagnetic modelling for GPR systems and environment

Special Issue Editors:
– Prof. Dragan Poljak (University of Split, Croatia) – dragan.poljak@fesb.hr
– Lara Pajewski (Sapienza University of Rome, Italy) – lara.pajewski@uniroma1.it

Deadlines and Milestones:
– Submission deadline: 31 October 2018;
– Publication of the accepted papers: 31 December 2018.

Notes:
Submissions are open to scientists and experts who participated in the workshop and their co-Authors, only. When you submit your paper, please specify in your 'Letter to the Editor' that you wish to have the paper included in this Special Issue.

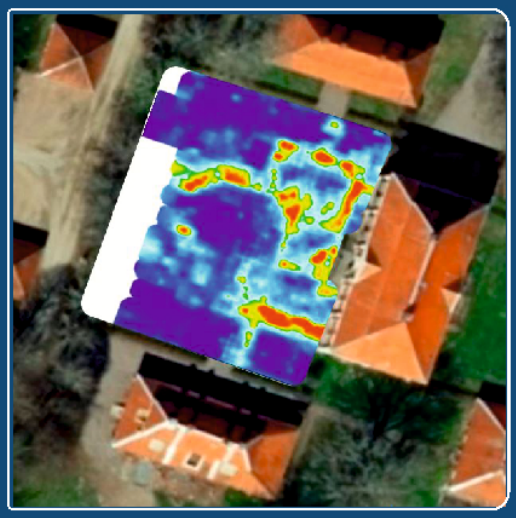

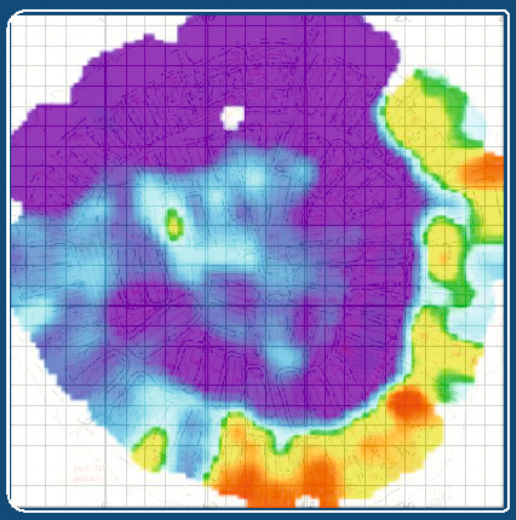

Adapis Georadar Teknik AB

Sweden
Tlf:+46 42 123 638
info@georadar.eu

Georadar.eu

AGT is Technical Partner
in GPR projects within Engineering,
Archaeology, Underground utilities,
Heritage buildings and more.

www.georadar.eu

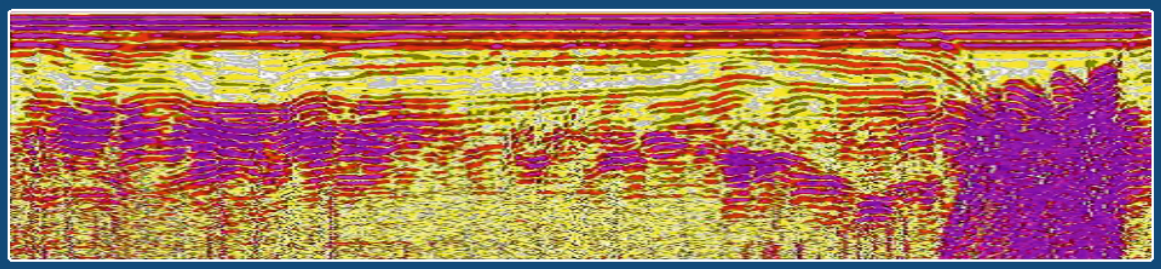

TU1208 Scientific Contest 2018-2019

This contest is open to Members of TU1208 GPR Association, only. Among all papers submitted to *Ground Penetrating Radar* from 1 September 2018 to 20 April 2019, whose Corresponding Author is a Member of TU1208 GPR Association at the time when the paper is submitted, the Editorial Board of the journal will select:

(i) the Best Paper having an early-career investigator as Corresponding Author,
(ii) the Best Paper having a female scientist as Corresponding Author,
(iii) the Best Paper having a scientist from an Inclusiveness Target Country as Corresponding Author.

The Corresponding Authors of the awarded papers will receive award certificates and TU1208 GPR Association will support their participation in the 10th International Workshop on Advanced Ground Penetrating Radar (IWAGPR 2019, Rome, Italy, 3-5 July 2019) by reimbursing their conference registration fee.

Notes:

– An early-career investigator is a scientist who received his PhD degree since no more than eight years at the time when the paper is submitted.

– Inclusiveness Target Countries are: Albania, Bosnia-Herzegovina, Bulgaria, Cyprus, Czech Republic, Estonia, Croatia, Hungary, Lithuania, Latvia, Luxembourg, Malta, Montenegro, Poland, Portugal, Romania, Slovenia, Slovakia, the former Yugoslav Republic of Macedonia, Republic of Serbia and Turkey.

– When you submit your paper, please mention in your 'Letter to the Editor' that you wish to participate in the contest. If you are an early-career investigator, please let us explicitly know (then, you will be contacted by the Editorial Board and asked to provide your PhD certificate).

IDS GeoRadar

First Class GPR Solutions

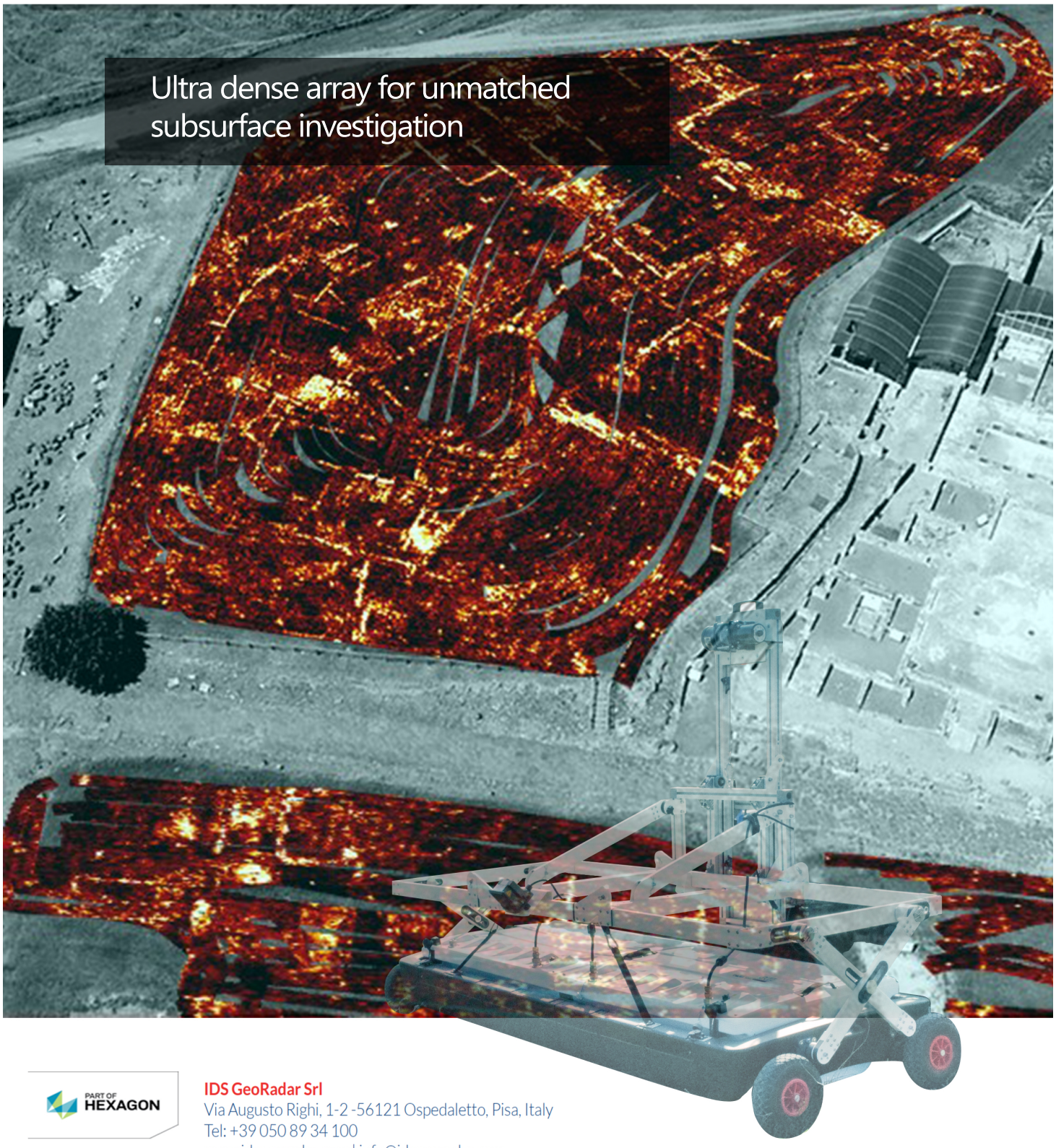

PART OF HEXAGON

IDS GeoRadar Srl
Via Augusto Righi, 1-2 -56121 Ospedaletto, Pisa, Italy
Tel: +39 050 89 34 100
www.idsgeoradar.com | info@idsgeoradar.com

Ground Penetrating Radar, Issue 2, Volume 1 | July 2018
www.GPRadar.eu/journal, journal@GPRadar.eu

Published by TU1208 GPR Association, Rome, Italy